Solar Wind Influences on Properties of the Ionosphere

A Thesis Submitted to the
College of Graduate Studies and Research
in Partial Fulfillment of the Requirements
for the degree of Master of Science
in the Department of Physics and Engineering Physics
University of Saskatchewan
Saskatoon

By

D. Huyghebaert

Permission to Use

In presenting this thesis in partial fulfilment of the requirements for a Postgraduate degree from the University of Saskatchewan, I agree that the Libraries of this University may make it freely available for inspection. I further agree that permission for copying of this thesis in any manner, in whole or in part, for scholarly purposes may be granted by the professor or professors who supervised my thesis work or, in their absence, by the Head of the Department or the Dean of the College in which my thesis work was done. It is understood that any copying or publication or use of this thesis or parts thereof for financial gain shall not be allowed without my written permission. It is also understood that due recognition shall be given to me and to the University of Saskatchewan in any scholarly use which may be made of any material in my thesis.

Requests for permission to copy or to make other use of material in this thesis in whole or part should be addressed to:

Head of the Department of Physics and Engineering Physics
University of Saskatchewan
116 Science Place, Rm 163
Saskatoon, SK S7N 5E2
Canada

Abstract

The Sun's corona expands outward, populating the solar system with plasma. This plasma is known as the solar wind. The solar wind carries with it the Sun's magnetic field, which is also known as the interplanetary magnetic field (IMF). The resulting configuration of the IMF creates a current sheet at solar equatorial latitudes, which the Earth crosses as it orbits the Sun. When the Earth is on one side of the current sheet it is in a sector where the IMF is directed largely away from or toward the Sun. On the other side of the current sheet the IMF is in opposite direction. The crossing of the current sheet is known as a sector boundary crossing (SBC). The solar wind and IMF properties change significantly near the current sheet, and this affects the Earth's ionosphere.

The Super Dual Auroral Radar Network (SuperDARN) high frequency (HF) radar data rates from 2001-2011 were examined using several techniques: a superposed epoch analysis, a fast fourier transform (FFT) analysis, and a cross–correlation analysis. Data from multiple instruments were analyzed in this study. These include the solar wind and IMF data from spacecraft, observations of charged particles precipitating into the Earth's ionosphere, echoes from ground–based SuperDARN radars, and data from gound–based neutron monitors that detect galactic cosmic rays.

Solar wind and IMF properties change significantly across a sector boundary. An increase in the IMF magnitude of about 30% occurs on the day of the SBC, and the IMF returns to pre–crossing values over the next two days. There is a decrease in the solar wind speed of about 15% the day before and the day of the SBC, and the solar wind density doubles at the time of the SBC. The polarity of the SBC does not appear to affect the solar wind and IMF. A peak in the data rate of SuperDARN echoes from both the ionosphere and ground occurs within one day of the SBC, though the variability of these data is quite large. The hemispherical power, which is an estimation of the electron energy flux precipitating into the ionosphere derived from satellite observations, increases following a SBC. Satellite particle data also revealed that the equatorward auroral oval boundary moves equatorward following a SBC. The cosmic ray counts at the Earth's surface appear to be unaffected by the SBC.

The solar wind and ionosphere data sets exhibited strong periodicities, and these were

harmonics of the synodic rotational period of the Sun (approximately 27 days). Common periodicities observed were 27 days, 13.5 days, 9 days, 6.75 days and 5.4 days. There was a dominant 9–day periodicity observed in the solar wind and ionospheric data from 2005–2008, but was not observed in the solar 10.7 cm wavelength electromagnetic flux. The 9–day periodicity in the solar wind during this period has been linked to three persistent features on the Sun that produced corotating high–speed streams, or areas of fast solar wind. The parameters whose change did not depend on the polarity of the SBC had periodicities that were half that of the SBCs.

From the cross–correlation analysis some relationships between the data sets became evident. For periods of high solar wind speed there were low SuperDARN data rates, and vice versa. The solar wind speed and hemispherical power were found to be well correlated, while the hemispherical power and the SuperDARN scatter occurrence were found to be anticorrelated.

The solar wind changes appear to be affecting the state of the ionosphere, likely through particle precipitation. The SuperDARN scatter occurrence has been shown in past studies to be most greatly affected by changes in the electron density profile of the ionosphere, which can be influenced by changes in particle precipitation. These results demonstrate a link between the solar wind and the state of the ionosphere.

Acknowledgements

First off, I would like to thank my family and friends for supporting me in every way that they did. I could not have finished my thesis without them. I would also like to sincerely thank Dr. Kathryn McWilliams for providing me with the opportunity and knowledge to complete my M.Sc. The DMSP data, the OMNI data and the cosmic ray data were provided by Dr. Barbara Emery, the NASA Goddard facility and the Bartol Research Institute, respectively. This project would not have been possible without their contributions, and I thank them. None of this would be possible without funding, and therefore I thank the Canadian Space Agency, the National Sciences and Engineering Research Council, the University of Saskatchewan and the Institute of Space and Atmospheric Studies for providing me with the means to complete my project. I would also like to thank the people in the Institute of Space and Atmospheric Studies and the Physics and Engineering Physics Department that provided help and advice along the way. Everything that has been done is very much appreciated.

The DMSP particle detectors were designed by Dave Hardy of the Air Force Research Laboratory, and the Auroral Boundary/Hemispheric Power Indices are provided with permission from the Space Vehicle Directorate, Air Force Research Laboratory, Kirtland AFB, NM 87117, via the Cedar Database at the National Center for Atmospheric Research which is supported by the National Science Foundation.

Contents

List of Figures

List of Abbreviations

ACE	Advanced Composition Explorer
ACF	Autocorrelation Function
AU	Astronomical Unit
B	Magnetic Field Vector
CIR	Corotating Interaction Region
DMSP	Defense Meteorological Satellite Program
E	Electric Field Vector
FC	Faraday Cup
FFT	Fast Fourier Transform
GCR	Galactic Cosmic Ray
GS	Ground Scatter
GSE	Geocentric Solar Ecliptic
GSM	Geocentric Solar Magnetospheric
HCS	Heliospheric Current Sheet
HF	High Frequency
HP	Hemispherical Power
HSS	High–Speed Streams
IMF	Interplanetary Magnetic Field
IMP	Interplanetary Monitoring Platform
IS	Ionospheric Scatter
ISR	Incoherent Scatter Radar
LEP	Low Energy Particle
MAG	twin triaxial flux–gate Magnetometer
MBI	Midnight Boundary Index
MLT	Magnetic Local Time
SBC	Sector Boundary Crossing
SD	SuperDARN
SuperDARN	Super Dual Auroral Radar Network
SW	Solar Wind
SWE	Solar Wind Experiment
SWEPAM	Solar Wind Electron, Proton, and Alpha Monitor
TEC	Total Electron Content
UV	Ultraviolet
V	Electric Potential
VAI	Vorticity Area Index

Chapter 1

Introduction

There are still many unknowns when it comes to understanding the Earth's atmosphere. While it is known that the Sun influences the climate of the Earth through solar electromagnetic radiation and solar wind particles, the mechanisms by which they are connected are not fully understood [e.g., *Haigh*, 2003; *Gray et al.*, 2010]. It has been shown that the orientation of the radial component of the Sun's magnetic field determines whether the northern or the southern polar regions of the Earth's ionosphere receive energetic particle precipitation originating from the Sun [*Fairfield and Scudder*, 1985]. The Sun's magnetic field is also known as the interplanetary magnetic field (IMF). The magnetic path for charged particle precipitation from interplanetary space provides a direct connection between the interplanetary medium and the atmosphere of the Earth. The plasma expelled from the Sun travels outward through the solar system and is known as the solar wind. There is a magnetic coupling between the Sun and Earth that drives plasma circulation in the Earth's magnetosphere and ionosphere [e.g., *Dungey*, 1961; *Russell and Elphic*, 1978; *Lu et al.*, 2002]. This thesis presents an investigation of how the solar wind and the IMF influence ionospheric properties. The ionosphere, which is the intermediate boundary layer between space and atmospheric weather, is key to understanding the coupling between the electromagnetic space environment and the neutral gases in the lower atmosphere.

The goal of this research is to link changes in the Earth's space environment, i.e., the solar wind, to changes in the ionosphere of the Earth. To do this, data from many different instruments were analysed. Instruments on board spacecraft measure the solar wind. The solar wind bulk velocity, proton density and the IMF were examined in this thesis. To link the solar wind measurements to the ionosphere, the state of the ionosphere must also be determined. This was accomplished by using data from satellite and ground–based instru-

ments. Satellites orbiting the Earth measure properties of charged particles precipitating into the Earth's ionosphere. The ground–based instruments include radars that measure plasma circulation in the ionosphere over large areas and neutron detectors that provide information on the galactic cosmic rays reaching the Earth's surface.

As the Earth orbits around the Sun it tends to be located in IMF sectors that are predominately directed toward or away from the Sun [*Wilcox and Ness*, 1967]. When the IMF encountered by the Earth changes from an away direction to a toward direction, or vice versa, it is called a solar sector boundary crossing (SBC). These SBCs have been shown in the past to be correlated with atmospheric changes. For example, following the passage of a solar sector boundary, there is an enhancement in the ionospheric total electron content (TEC) at high latitudes on the day of the SBC, and a depletion in the TEC following the SBC [*Mendillo and Schatten*, 1983]. The TEC is a measurement of a straight–line integrated column of electron density in the atmosphere. A relationship between the intensity of tropical weather patterns and the passage of the Earth across a solar sector boundary has been noted by *Wilcox et al.* [1974]. The vorticity area index (VAI) is a "measure of the size and prominence of all the low pressure troughs in the region of the Northern Hemisphere north of $20°N$" [*Wilcox et al.*, 1974]. As seen in Figure 1.1, the VAI drops during the passage of a solar sector boundary, with the lowest value measured on the day following a SBC during the winter months (November–March). A decrease in the VAI can correspond to a decrease in the wind speed or the size of the low pressure wind troughs. The ability of existing atmospheric models to predict the VAI around the crossing of solar sector boundaries was evaluated by *Larsen and Kelley* [1977]. In the days following a SBC there is a significant decrease in the correlation coefficient between the predicted VAI and the actual VAI (see Figure 1.2). A more recent study performed by *Prikryl et al.* [2009] has confirmed the change in the VAI during SBCs. This suggests that there is a mechanism or mechanisms by which conditions in space affect the atmosphere in ways that are not predicted by atmospheric models.

Studies have shown that processes occurring at ionospheric altitudes are able to propagate downward to lower altitudes. This includes nitric oxide production through energetic particle precipitation which can be transported downwards from the ionosphere to the stratosphere given the right meteorological conditions (strong polar vortices) [*Solomon et al.*, 1982a,b].

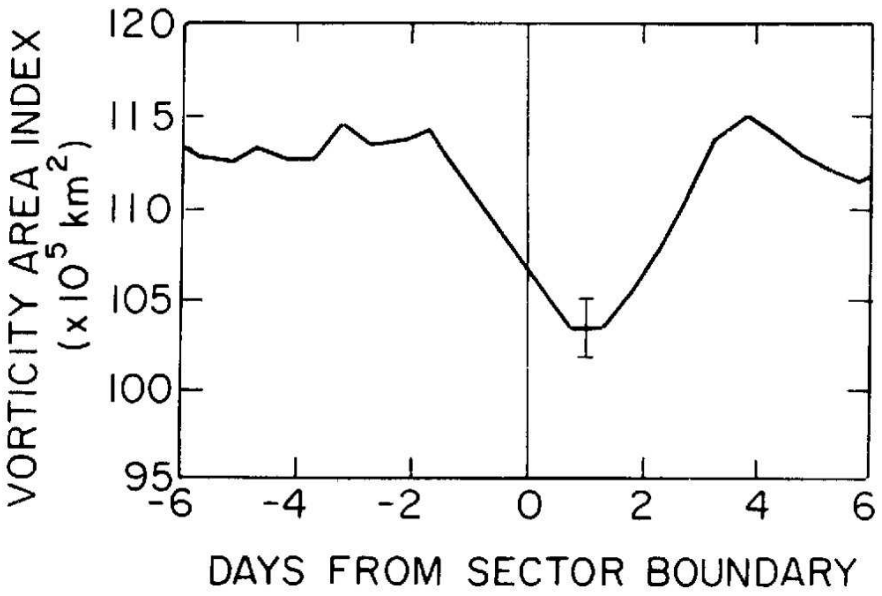

Figure 1.1: The averaged vorticity area index during the Earth's crossing of solar sector boundaries during the winter months (November–March). [From *Wilcox et al.*, 1974]

This physical mechanism has been linked to reductions in stratospheric ozone [*Randall et al.*, 2005]. The current interest in understanding weather and climate, as well as the studies demonstrating links between the atmosphere and space, highlight the potential importance of this research.

A much more extensive understanding of the coupling between the Sun and the Earth would provide a multitude of benefits. While the current study does not include the coupling along the entire path between the Sun and Earth, it does involve an important part of it– the Earth's ionosphere. Improving our understanding of this important intermediary layer has the potential to improve our understanding of meteorogical weather. Recent studies of mechanisms, such as vertical electric fields and changing ionospheric chemistry, support the idea that solar conditions have the potential to affect lower atmospheric properties.

The vertical electric field may affect cloud microphysics. Increasing the vertical currents in the atmosphere has the potential to increase ice formation in clouds [*Tinsley*, 2000]. This in turn can cause earlier dissipation of supercooled clouds, which are normally found in maritime areas rather than continental areas [*Tinsley*, 2000]. In thin clouds the increased ice formation can decrease the albedo, the incoming shortwave radiation absorption, and the

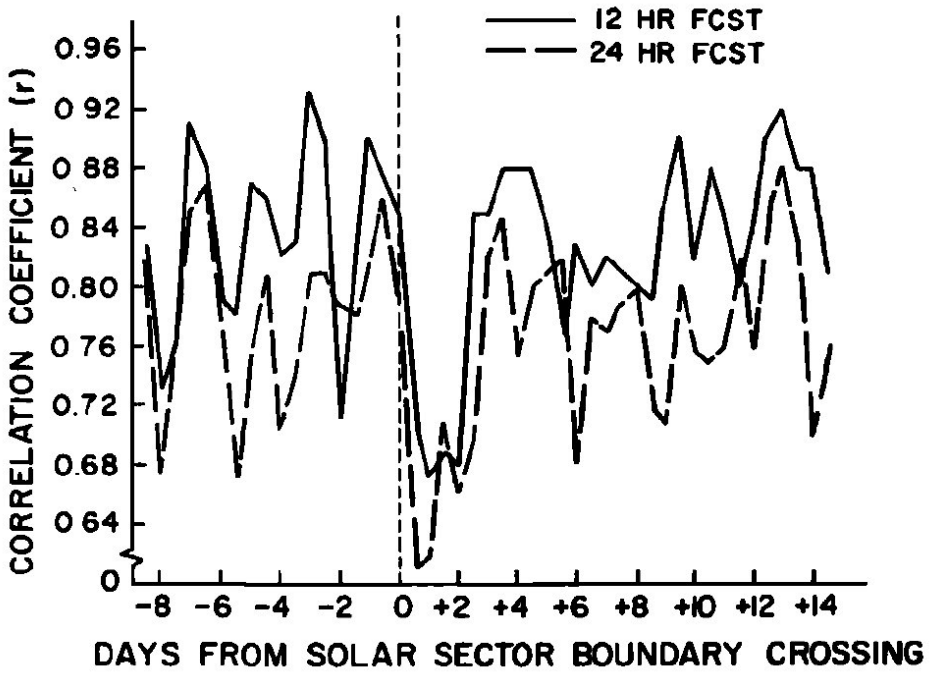

Figure 1.2: An epoch analysis performed on the correlation coefficients between the predicted and the actual vorticity area index around a solar sector boundary. [From *Larsen and Kelley*, 1977]

opacity of the clouds to outgoing longwave radiation. Increased vertical currents are also said to affect the VAI through an increase in precipitation from increased ice formation, which creates a latent heat transfer between the clouds and the Earth's surface [*Tinsley*, 2000].

Changing the ionospheric chemistry through charged particle precipitation could affect the nearby mesosphere's chemistry [*Solomon et al.*, 1982a,b], which could then propagate down through the stratosphere to the troposphere. Ozone is one of the atmospheric constituents that can be affected during energetic particle precipitation. Stratospheric ozone affects the amount of UV rays reaching the surface of the Earth [*Haigh*, 1994]. Charged particle precipitation can affect the ratios of trace species in the atmosphere and can change atmospheric circulation patterns, both of which can affect the production and destruction of ozone [*Gray et al.*, 2010].

The work presented in this thesis is also related to the reliability of radio communications. Over the horizon radio communication depends on the ionosphere to guide the radio waves over large distances in the region between the ionosphere and the ground, while satellite

communication requires radio waves to penetrate through the ionosphere. When the ionosphere has a relatively high plasma density, it is possible for radio wave absorption to occur [*Blaunstein and Plohotniuc*, 2008]. When the radio wave is absorbed it is not reflected or transmitted through the ionosphere, leading to a radio blackout. Some radio communications that would normally penetrate through the ionosphere wouldn't be received by satellites and/or spacecraft during increased ionospheric plasma density events.

Space weather not only affects communications with satellites and spacecraft, it also affects the operation of these platforms. Changes in the plasma density that the satellites or spacecraft are passing through can have catastrophic effects on their operation. There is a possibility of charge being deposited on the satellites and spacecraft, which happens more often during periods of increased plasma density. This build–up of charge can eventually discharge and damage circuitry or flip memory bits, perhaps making the satellite/spacecraft unoperational [e.g., *Baker*, 2002]. Low–altitude spacecraft and satellite orbits are also affected by the drag of the atmosphere. During periods of higher solar activity, the thermosphere expands, which results in more drag on the spacecraft and satellites due to the increased density. This causes the orbit to decay and can therefore shorten the lifetime of these devices by requiring the limited on–board fuel to be used to boost the satellite back up to its desired orbit [e.g., *Baker*, 2002]. The relationship between solar wind properties and properties of the ionosphere will be investigated in this thesis in the hope of a better understanding of ionospheric weather.

Chapter 2

Background

2.1 Solar Wind and Interplanetary Magnetic Field

2.1.1 General Solar Properties

There are multiple layers of the Sun, and from the center out these are called the core, the radiation zone, the convection zone, the photosphere, the chromosphere and the corona [e.g., *Cravens*, 1997; *Freeman*, 2001]. In the core fusion occurs, and this is the source of energy for the Sun. The energy from the Sun's core is carried outward through the radiation zone and the convection zone. The layer bordering the convection zone is the photosphere, which is the solar surface we can see, and it has a temperature of approximately 6000 K [*Cravens*, 1997]. The photosphere can have dark spots called sun spots, which are observed more frequently when the Sun is more active, i.e., near the maximum of the Sun's activity cycle, which is known as solar maximum [e.g., *Hathaway and Wilson*, 2004]. The chromosphere and corona make up what one could think of as the atmosphere of the Sun. The corona can reach temperatures of millions of kelvin, and it is the source of the solar wind particles that stream out through interplanetary space [*Cravens*, 1997]. The solar wind is a plasma that has a very high conductivity and therefore carries the solar magnetic field out through interplanetary space.

2.1.2 Solar Wind Properties

The solar wind consists of charged particles that form three main electron velocity distributions: the "core", the "halo" and the "strahl," which are illustrated in Figure 2.1. The core distribution includes about 94% of the solar wind electrons, and it is isotropic in velocity

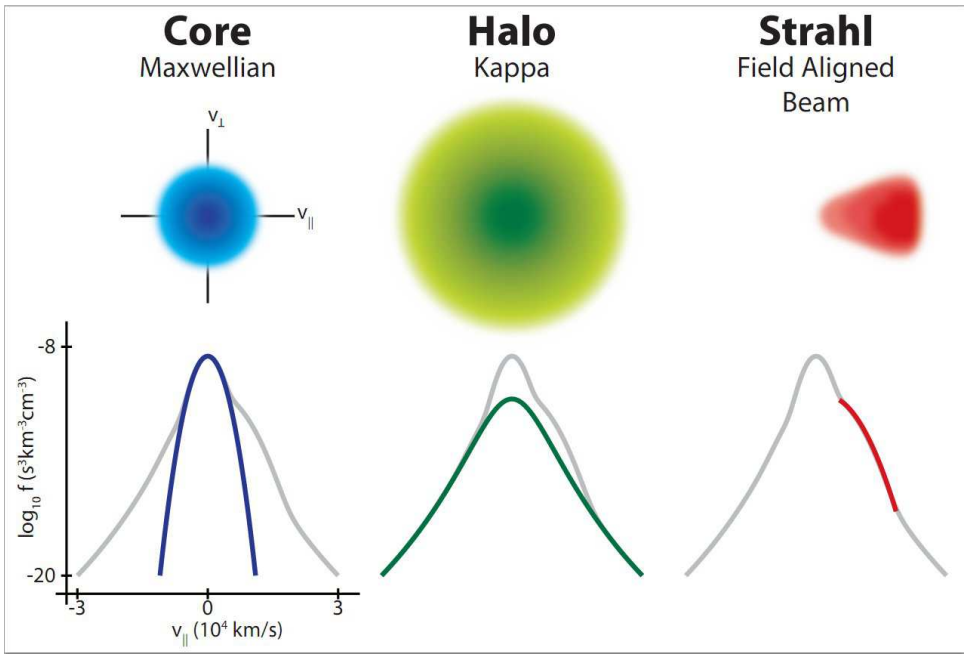

Figure 2.1: A depiction of the three electron distributions of the solar wind, with their associated velocity distributions that are parallel to the IMF. [From *Pulupa*, 2013]

[*Fairfield and Scudder*, 1985]. The core electrons in the solar wind have observed temperatures less than 10^5 K [*Fairfield and Scudder*, 1985], or energies below approximately 100 eV [*Pilipp et al.*, 1987]. The halo is the more energetic part of the solar wind distribution, having energies above 100 eV [*Pilipp et al.*, 1987]. The halo was found to be strongly anisotropic, with a subset of the distribution consisting of a large number of electrons streaming along the magnetic field lines of the Sun. These energetic field–aligned electrons were labelled the strahl [*Fairfield and Scudder*, 1985]. This strahl was found to be missing at sector boundaries, and strongest in the interior of magnetic sectors [*Fairfield and Scudder*, 1985]. Solar sectors and sector boundaries will be discussed in more detail in Section 2.1.3. It is thought that the strahl electrons have high energies because they experience very few collisions with the bulk solar wind plasma as they travel outward from the Sun [*Fairfield and Scudder*, 1985]. There is a stronger strahl when there is a relatively small ($\sim$ 1 cm^{-3}) solar wind density. The particles in the strahl are field aligned due to the conservation of the first adiabatic invariant, which describes how the magnetic field strength and the velocity of the electrons perpendicular to the magnetic field are conserved. The more energetic the strahl is, the more field–aligned the strahl electrons become [*Fairfield and Scudder*, 1985; *Pilipp et al.*,

1987]. This strahl distribution can be thought of as a focused beam of electrons guided by the magnetic field.

The strahl is dependant on a solar latitudinal variation in the solar wind's density and speed. As the solar latitude increases, the solar wind density decreases and the solar wind speed increases [*Gosling and Pizzo*, 1999]. The Sun's magnetic field can be thought of as pseudo–dipolar [*Gosling and Pizzo*, 1999]. As plasma streams out into space at equatorial latitudes it carries looped magnetic field lines with it, and the magnetic field becomes stretched. The heliospheric current forms in the region between oppositely directed stretched (non–dipolar) magnetic field lines. The streamer belt is the area around the heliospheric current sheet (HCS) where there is a relatively large solar wind proton density and a relatively low solar wind speed. Towards the poles the dipolar magnetic field is, for all intents and purposes, "open," allowing plasma to flow outward along these magnetic field lines. Since the plasma is not constrained by the magnetic field as it expands outward, the solar wind speed is larger at higher latitudes [*Gosling and Pizzo*, 1999]. The varying solar wind speed with latitude can be seen in Figure 2.2, where the measurements were taken by instruments onboard the Ulysses satellite. The Earth is most likely to be found in the streamer belt along the HCS during its orbit around the Sun, but can emerge out of it due to the tilt in the Sun's axis and the varying solar magnetic field during perturbed conditions.

2.1.3 Sun's Magnetic Field

The Sun has an eleven–year cycle of magnetic activity, during which the polarity of the Sun's magnetic field reverses. The middle of the reversal is the peak of magnetic activity, and this is known as solar maximum. When the largely dipolar field is established the Sun's magnetic activity is weak, and this is known as solar minimum. Near solar maximum the Sun is very active, with many sunspots. When the Sun is more active there are more highly energetic charged particles in the solar wind [*Hargreaves*, 1992]. During solar maximum the Sun also emits a higher flux of 10.7 cm wavelength electromagnetic waves (F10.7 index), which is correlated with the sunspot number [e.g., *Hathaway and Wilson*, 2004]. The F10.7 index refers to the flux of 10.7 cm radiation emitted by the Sun and is observed at the Penticton observatory on the Earth's surface. During solar minimum the Sun becomes quieter. The

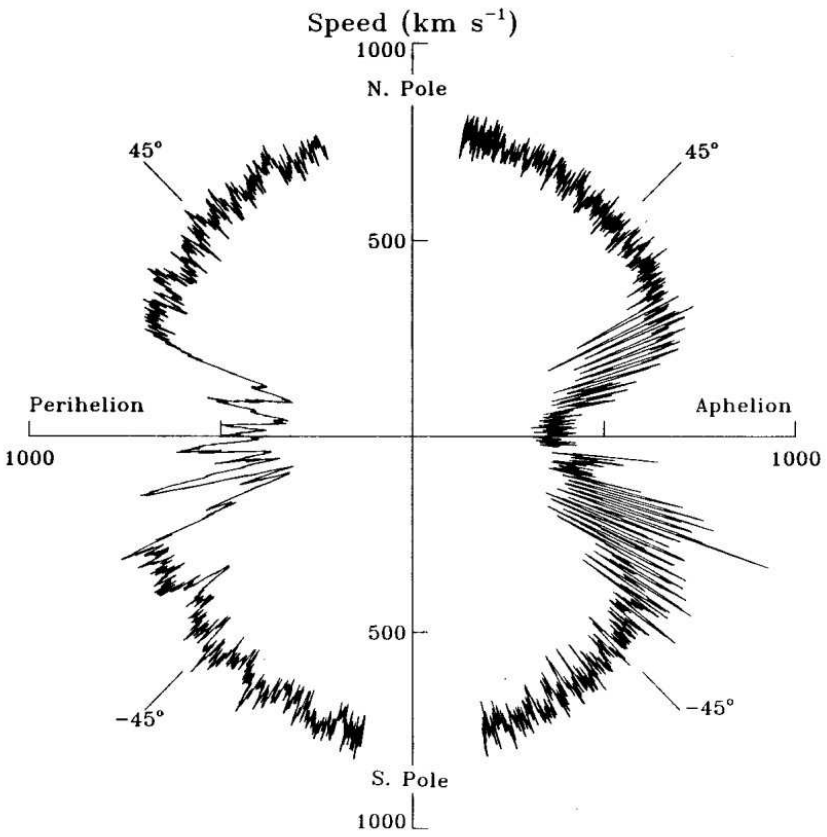

Figure 2.2: Solar wind speed as a function of solar latitude, measured between February 1992 and December 1997 by the Ulysses spacecraft. The right side of the plot are data measured at a distance of 5.4 AU and the left side are data measured at 1.4 AU. [From *Gosling and Pizzo*, 1999]

F10.7 index is lower, as are the numbers of flares and sunspots [*Cravens*, 1997].

Sun spots appear as dark "blotches" on the photosphere of the Sun. The integrated brightness of a sunspot is about 60–70% of that of the photosphere [*Solanki et al.*, 2006]. Sunspots appear more frequently near solar maximum, and less frequently near solar minimum [e.g., *Hathaway and Wilson*, 2004]. Generally sunspots appear in pairs that have opposite magnetic polarities. Magnetic field lines emerge from one spot and enter the other spot forming a magnetic loop. The leading sunspot, with regards to the Sun's rotation, drifts towards the Sun's pole, and the trailing sunspot drifts towards the Sun's equator [*Hathaway and Wilson*, 2004]. These sunspots have strong magnetic fields of about 0.3 T at their center [*Solanki et al.*, 2006]. As the sunspots accumulate near the Sun's poles (having the opposite polarity than the pole), the magnetic polarity of the Sun reverses. The Sun's magnetic field

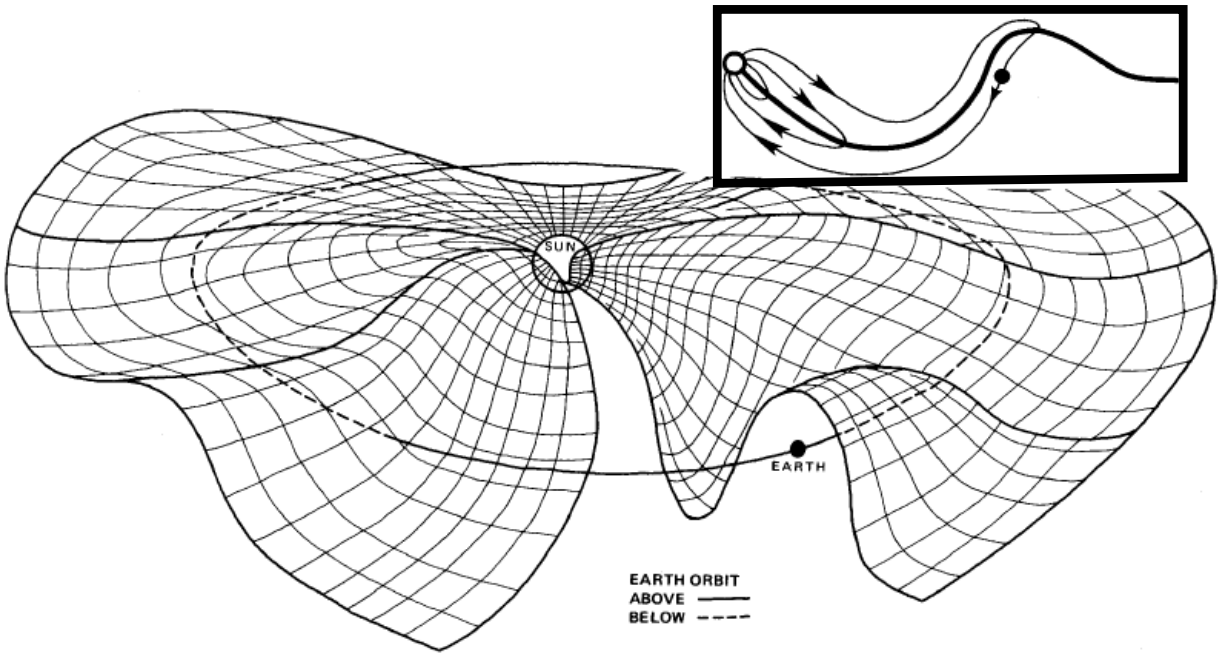

Figure 2.3: Depiction of the heliospheric current sheet, with the Earth's orbit included. The depiction in the top right is a view from the side of the Sun's magnetic field (thin black line), the Earth (solid black dot) and the heliospheric current sheet (thick black line). [Adapted from *Akasofu*, 1981]

becomes generally dipolar again, with the opposite polarity than it had at the beginning of the cycle. This reversal happens approximately every 11 years [*Cravens*, 1997; *Hathaway and Wilson*, 2004], which means a complete magnetic field cycle of the Sun takes about 22 years. The 22 year solar cycle is known as a Hale Cycle [*Sonett*, 1982].

The Sun's magnetic field is "frozen" into the solar wind plasma, which has nearly infinite conductivity. This nearly infinite conductivity enables the plasma to counteract changes to the magnetic field, which effectively freezes the IMF into the solar wind plasma as it travels outward from the Sun [*Cravens*, 1997]. This results in the highly elongated IMF lines at equatorial latitudes (top right inset of Figure 2.3). According to Ampere's law of electrodynamics, when two magnetic field lines are in opposite directions and in the vicinity of one another, a current sheet will form between them. The elongated IMF therefore creates a current sheet at equatorial latitudes of the Sun.

The heliospheric current sheet that extends outward from the Sun into the solar system

is, to first approximation, aligned with the solar ecliptic plane, but the current sheet can be distorted [*Smith*, 2001]. Figure 2.3 depicts an undulating heliospheric current sheet, where the currents flow mainly azimuthally. There are ripples that occur in this current sheet, causing it to resemble a ballerina skirt. On one side of the current sheet the IMF is directed towards the Sun, and on the other side of the current sheet the IMF is directed away from the Sun [e.g., *Smith*, 2001]. Whether the IMF is directed away from or toward the Sun above or below the current sheet depends on the polarity of the solar magnetic field, and therefore on the solar cycle, as the magnetic polarity of the Sun flips approximately every 11 years.

The basic shape of the IMF in the solar system is called the Parker Spiral. This archimedian spiral shape arises because the IMF is frozen into the radially expanding solar wind plasma, but the origin of this magnetic field is rotating with the Sun. This rotation and the outflow of solar wind plasma results in a curve in the IMF. The Sun fully rotates about every 24 days at the solar equator, but during this time the Earth is orbitting the Sun, resulting in an apparent 27–day rotation period when observed from the Earth. This is known as the solar synodic rotation period and results in an approximately 45° angle from radial in the IMF at the Earth's orbital distance. A depiction of the curved IMF can be seen in Figure 2.4, where the black lines are the sector boundaries, and the arrows give the direction of the IMF.

The solar wind plasma velocity distribution depends on the speed at which it's ejected at its solar origin. The variations in bulk solar wind velocity can result in fast solar wind catching up to slow solar wind as it expands into the solar system. When this bulk fast solar wind catches up to the slow solar wind it creates a corotating interaction region (CIR). This is a region of high solar wind pressure, high solar wind density and a sharp change from slow to high solar wind speed [*Gosling and Pizzo*, 1999]. When the Earth passes through one of these regions, the Earth's magnetosphere reacts to the changes in the solar wind plasma properties. The effects on the Earth's magnetosphere from changes in the solar wind plasma will be discussed in Section 2.2. At distances of the Earth's orbit, or 1 AU, the heliospheric current sheet is embedded in a CIR about two thirds of the time [*Gosling and Pizzo*, 1999]. This means that at solar sector boundary crossings there is likely a transition from slow to fast solar wind speeds two thirds of the time. At 3 AU the solar current sheet is embedded in a CIR almost all the time [*Gosling and Pizzo*, 1999].

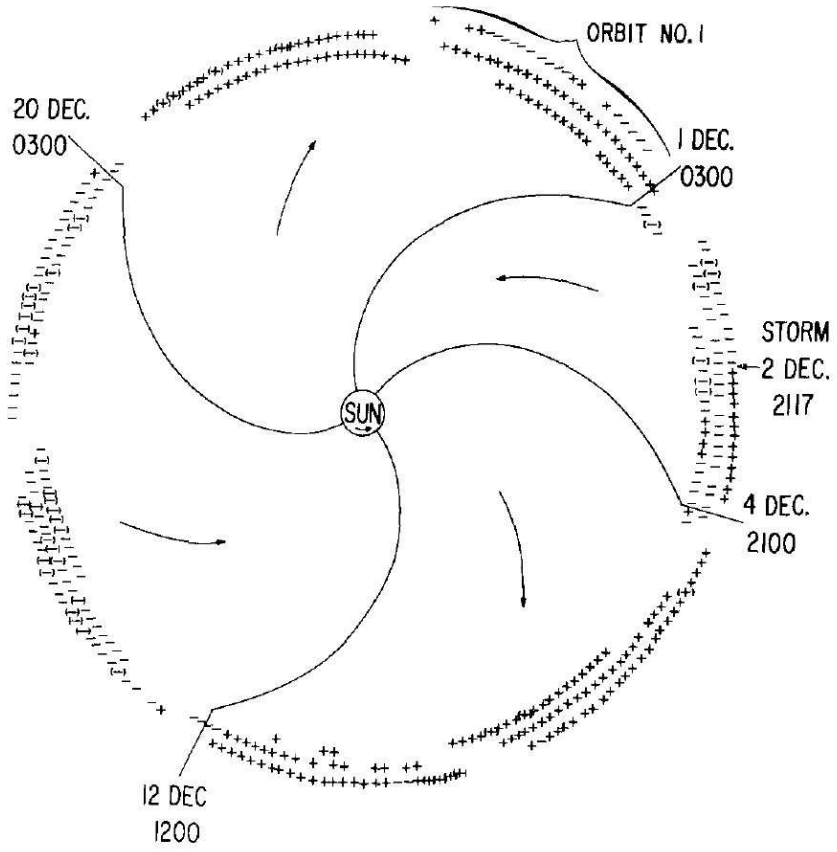

Figure 2.4: The Parker Spiral can be seen in this image from the spiral–like shape generated from the rotating Sun. The solid black lines are the sector boundary crossings and the arrows give the direction of the Sun's magnetic field. The "+" and "-" are measurements of the Sun's magnetic field direction from the IMP–1 spacecraft. [From *Wilcox and Ness*, 1967]

2.2 Earth's Magnetosphere

2.2.1 Earth's Magnetic Field

The Earth generates a mainly dipolar magnetic field. The geomagnetic field is compressed on the sunward side and elongated to very long distances (approximately 1000 R_E) downstream of the Earth [e.g., see *Sibeck et al.*, 1991]. The elongation of the magnetic field is due to its interaction with the solar wind and IMF. Magnetic reconnection results in geomagnetic field lines that are connected to the IMF and extend downstream of the Earth. This magnetic structure is known as the magnetotail. Figure 2.5 is a depiction of the magnetic field and

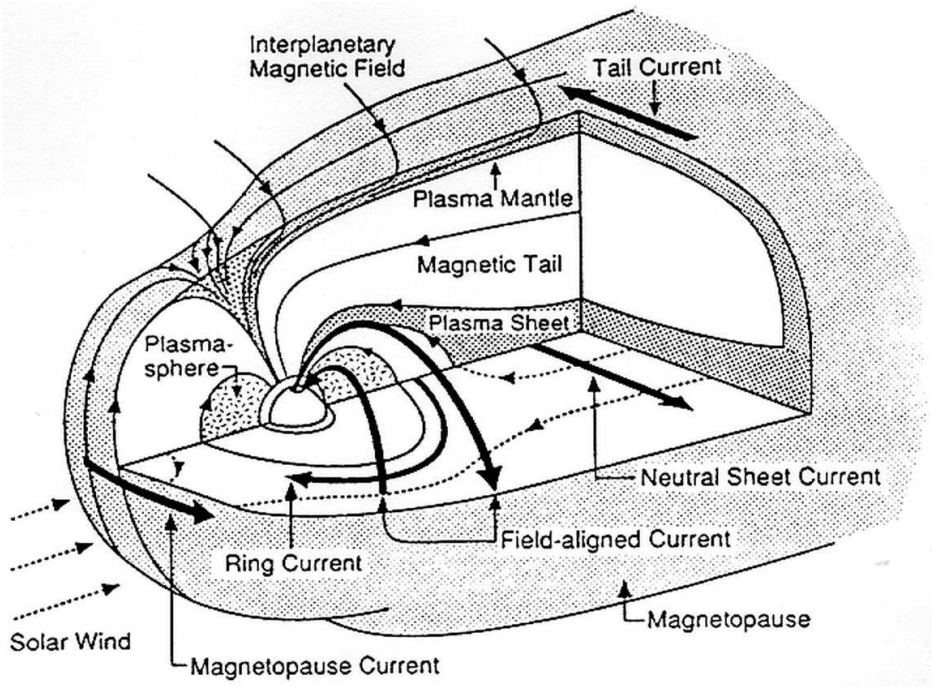

Figure 2.5: The Earth's Magnetosphere. The thin black lines represent the geomagnetic field lines, while the thick black lines represent the currents. [From *Kivelson and Russell*, 1995]

currents in the Earth's magnetosphere. The solar wind plasma exerts dynamic pressure on the Earth's magnetic field wherever the solar wind velocity has a component normal to the magnetosphere. Equilibrium is reached between the dynamic pressure of the solar wind and the magnetic pressure of the Earth's magnetosphere at the magnetopause. This is the Earth's magnetic field's boundary. The dynamic pressure exerted by the solar wind on the Earth's magnetic field varies, depending on the speed and density of the solar wind, and therefore the location of the magnetopause also changes [*Russell and Elphic*, 1978]. The sunward extent of the magnetopause is about 10 Earth radii upstream of the Earth during typical solar wind conditions (density of $5cm^{-3}$, velocity of 400km/s), but it can be located as close as about 5 Earth radii during extremely active solar wind conditions (density of $100cm^{-3}$, velocity of 1600km/s) [*Otto*, 2005].

There are two commonly used coordinate systems for the solar wind and IMF. They are the Geocentric Solar Ecliptic (GSE) coordinate system and the Geocentric Solar Magnetospheric (GSM) coordinate system. The GSE coordinate system has its x–axis pointing from

the Earth to the Sun, the z–axis pointing perpendicular to the orbital plane in the northern hemisphere, and the y–axis is perpendicular to both of these. GSM also has its x–axis along the Earth–Sun line, but it takes into account the orientation of the Earth's dipole axis. The z–axis in GSM coordinates is in the plane of the Earth's dipole axis and the x–axis, while being perpendicular to the x–axis. The y–axis is then perpendicular to both of these. The GSM coordinate system is useful when performing studies on interactions between the Earth's magnetic field and the IMF, as the GSM z–axis is in the plane of the Earth's dipole magnetic field.

2.2.2 Reconnection

When two magnetic fields that are oppositely directed converge, a process called magnetic reconnection can occur [*Dungey*, 1961; *Cravens*, 1997]. In the case of the IMF and the Earth's magnetic field, this occurs at the magnetopause. Solar wind particles can enter the Earth's magnetosphere following reconnection [*Dungey*, 1961; *Newell et al.*, 2009]. For reconnection to occur at the dayside magnetopause, a southward IMF orientation is preferred because the Earth's magnetic field is northward on the sunward side, where the IMF approaches the magnetopause. The "open" geomagnetic field lines (geomagnetic field lines that are connected to the IMF) are carried across the Earth's polar regions towards the nightside, where reconnection can occur in the magnetotail between the oppositely directed "open" geomagnetic field lines [*Dungey*, 1961]. The radial and azimuthal components of the IMF also affect the reconnection location, and this will be discussed in Section 2.3.3.

Following magnetic reconnection in the magnetotail, which produces "closed" magnetic field lines, the newly reconnected and highly distorted geomagnetic field contracts towards the Earth. By doing this the geomagnetic field returns to a lower energy state, approaching an undistorted dipole field shape [*Wolf*, 1975]. The charged particles that are frozen to the Earth's magnetic field convect with the magnetic field towards the Earth. The dipolar field is at a lower energy state, and the magnetic energy from the distorted geomagnetic field is transfered to the plasma. The plasma, which is free to flow along the geomagnetic field lines, gains kinetic energy and some of these particles are injected into the Earth's ionosphere, where they may cause aurora [e.g., *Wolf*, 1975].

2.3 Earth's Ionosphere

2.3.1 Ionospheric Plasma Regions

Plasma exists in the atmosphere in a region known as the ionosphere. The ionosphere is formed through photoionization of the neutral atmosphere by sunlight [*Bradbury*, 1938; *Nicolet and Aikin*, 1960] and through ionization by particle precipitation at higher latitudes [*Cravens*, 1997]. The neutral gas density decreases with altitude, eventually reaching densities where the collision rate is low enough for charged particles to remain ionized. At the lower altitudes (below 150 km), there is a significant reduction of ionization during the night due to a lack of photoionization and higher particle densities, where the high particle densities result in a large plasma recombination rate. The particle precipitation contribution to the plasma density in the ionosphere is therefore more evident at night, when the background plasma density is small [*Cravens*, 1997].

The Earth's ionosphere has three regions, which are known as the D, E and F regions. The plasma ionization in the D region peaks between altitudes of about 60 km and 90 km, the plasma ionization in the E region peaks between altitudes of about 105 km and 150 km and the plasma ionization in the F region peaks between 160 km and 400 km [e.g., *Hargreaves*, 1992]. The absorption of solar photons by different atmospheric constituents lead to these different plasma density peaks in the ionosphere. At F–region altitudes it is primarily atomic oxygen that absorbs the solar electromagnetic radiation, while at E–region altitudes molecular oxygen accounts for most of the absorption and subsequent ionization [e.g., *Hargreaves*, 1992]. At D–region altitudes a multitude of molecular species absorb solar electromagnetic radiation and cause ionization [e.g., *Hargreaves*, 1992]. An example of a vertical plasma density profile is shown in Figure 2.6.

The ionospheric regions have distinctive collision frequencies between atmospheric constituents, which includes neutral atoms, neutral molecules, ions and electrons. At D–region altitudes the collision rates are large allowing plasma to quickly recombine [*Hargreaves*, 1992]. Both the mean electron–to–neutral and ion–to–neutral collision frequencies are greater than their respective cyclotron frequencies at this altitude, causing the ions and electrons to drift

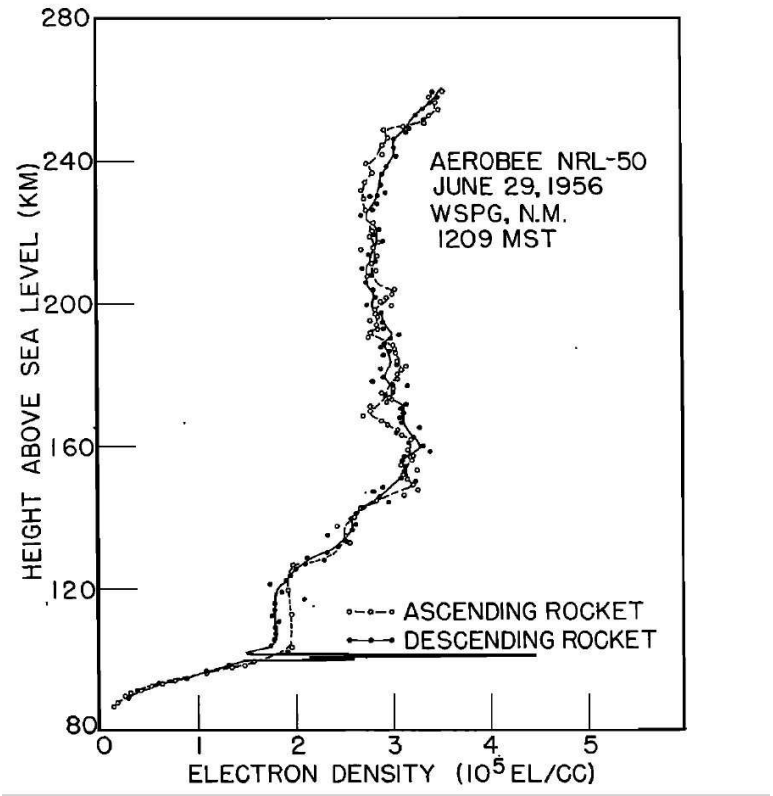

Figure 2.6: Electron density profile during the day measured with instruments onboard a rocket launched over White Sands, New Mexico. [From *Jackson and Seddon*, 1958]

primarily in the direction of the neutral particle flow. If there is sufficient plasma density, which can happen during particle precipitation events, the ionosphere can absorb radio waves. For more information on the absorption of radio waves, see Section 2.3.4.

In the E region the mean ion–to–neutral collision frequency is greater than the ion cyclotron frequency, but the mean electron–to–neutral collision frequency is less than the electron cyclotron frequency [*Hargreaves*, 1992]. This causes the ions to drift primarily in the same direction as the neutrals, while the electron motion is controlled primarily by electromagnetic forces. Due to the different relative drifts of the ions and electrons, the E region is at the altitude where currents flow [*Cravens*, 1997]. These currents are reduced in the midnight sector, since the E–region plasma is weakly ionized at this time unless there is particle precipitation. This is because there is no source of photoionization during the midnight sector and the collision frequency between electrons and molecular ions as well as ions and neutrals is relatively high in the E region, allowing the chemical processes required for recombination

to proceed quickly [*Hargreaves*, 1992]. When there is sufficient particle precipitation occuring in the ionosphere the E–region plasma may be significant as the particle precipitation gives a source of ionization (Section 2.3.3).

The F region is the highest of the three ionospheric regions, and, at these altitudes, the neutral densities are lower resulting in the mean collision frequencies between atmospheric constituents being much less than at lower altitudes. Since the mean collision frequency of the particles is low in the F region, when the source of ionization is removed the F region retains its ionization for an extended period of time [*Hargreaves*, 1992]. In the F region there are two peaks in plasma density during the day, and these are known as the F1 and F2 peaks. At night the F1 plasma density peak (located between 160 km and 180 km) is diminished, whereas the F2 plasma density peak (located between 200 km and 400 km) persists. The F1 plasma density peak is attributed to a peak in the atomic oxygen absorption of solar electromagnetic radiation, while the F2 plasma density peak is attributed to the ionization rate of oxygen from solar electromagnetic radiation being greater than the recombination rate of ions and electrons at this altitude [*Hargreaves*, 1992].

Ion– and electron–to–neutral collision rates are much less than their respective cyclotron frequencies in the F region. This results in both the electrons and ions being predominately controlled by electromagnetic forces and they do not have a significant drift in the direction of the neutral particle flow. They therefore drift in the same direction, perpendicular to the magnetic field, in the direction of the $\mathbf{E} \times \mathbf{B}$ drift [*Cravens*, 1997]. This bulk plasma drift is also known as ionospheric convection.

2.3.2 Polar Cap Convection Patterns

The magnetospheric convection cycle, as described in Section 2.2.2, is driven by magnetic reconnection and causes large scale circulation of plasma in the ionosphere. The plasma in the F region flows from noon to midnight over the very high latitude polar regions of the Earth, and then it returns at lower latitudes. The ionospheric plasma circulation is driven by the connection between the IMF and the Earth's geomagnetic field, where the orientation of the IMF is important to the circulation pattern [*Ruohoniemi and Greenwald*, 1996; *Hargreaves*, 1992]. The electric field, $\mathbf{E}$, can be defined by the electric potential, V, such that: $\mathbf{E} = -\nabla \mathrm{V}$.

Since the plasma flow follows the $\mathbf{E} \times \mathbf{B}$ drift, and since the electric field is the gradient of the electric potential, the drift of the plasma is parallel to the equipotential contours. The ionospheric circulation pattern can then be deduced from the potential patterns, such as those in Figure 2.7. The potential patterns are defined with respect to the magnetic local time (MLT), which describes the orientation of the Earth with respect to the Sun. 12 MLT refers to the direction facing the Sun (noon), while 0 MLT refers to the direction away from the Sun (midnight). 6 MLT is considered "dawn" and 18 MLT is considered "dusk." Figure 2.7 consists of statistical potential patterns created by combining all available observations of ionospheric plasma drift from the Super Dual Auroral Radar Network (SuperDARN) radars as a function of the IMF orientation at the time of the measurements [*Ruohoniemi and Greenwald*, 1996]. Typically ionospheric plasma flows from noon to midnight over the poles and returns to noon at lower latitudes. The flows, and therefore the potential patterns, vary as a function of the orientation of the IMF as it reaches the front of the magnetosphere. The central dial in Figure 2.7 represents the average IMF B_y and B_z orientation for the average potential patterns. Usually, the difference between the maximum and minimum voltage in SuperDARN convection maps is several tens of kV, with the most geomagnetic active periods reaching values of over 100 kV.

The ionospheric plasma in Figure 2.7 is travelling over the pole from the dayside to the nightside (12 to 24 MLT) parallel to the equipotential contour. The electric field is therefore approximately directed from dawn to dusk (6 to 18 MLT) over the pole. The plasma continues in the direction of the equipotential line, returning from nightside to dayside at low latitudes to complete the circuit.

It is evident from Figure 2.7 that the IMF B_z and B_y GSM components play a role in the ionospheric circulation pattern. The IMF B_z component affects the rate of reconnection at the magnetopause, which in turn affects the strength of convection in the ionosphere. A large negative IMF B_z component results in faster ionospheric convection drifts and intensified potential patterns [*Ruohoniemi and Greenwald*, 1996]. The IMF B_y component affects the dawn/dusk asymetry in the convection patterns [*Ruohoniemi and Greenwald*, 1996]. These effects are due to the IMF requiring to be antiparallel to the Earth's magnetic field for reconnection to occur [*Cravens*, 1997]. The IMF components (including IMF B_x) determine

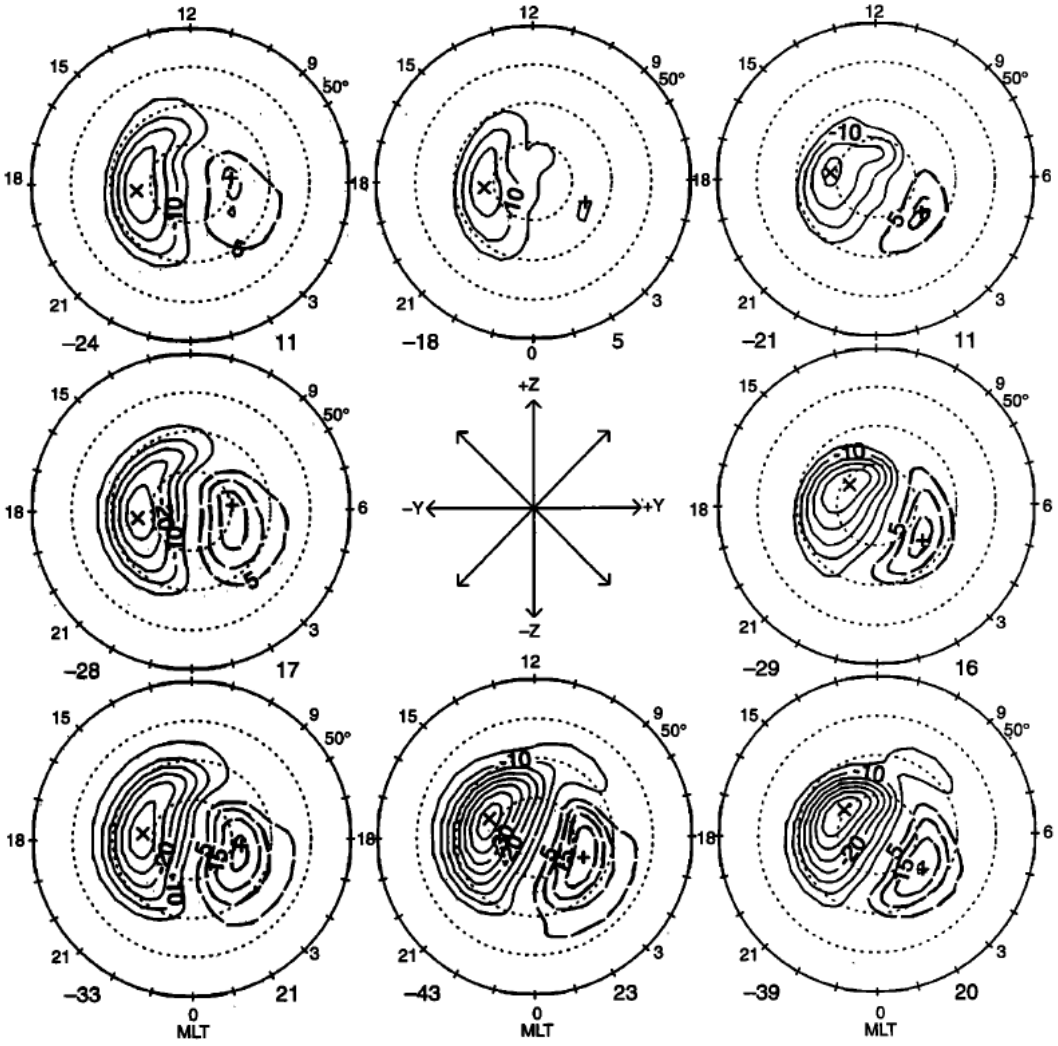

Figure 2.7: Average equipotential patterns measured by SuperDARN and sorted by IMF B_z and B_y. The "x" symbol in each plot denotes the most negative voltage and the "+" symbol denotes the most positive voltage, where the numbers to the bottom left and to the bottom right of each circular plot denote these values in kV. The dial in the middle of the plots gives the average orientation of the IMF for each panel. The plasma in the F region flows parallel to the potential contours, therefore these plots also represent the convection pattern of the F-region plasma for various orientations of the IMF. [From *Ruohoniemi and Greenwald*, 1996]

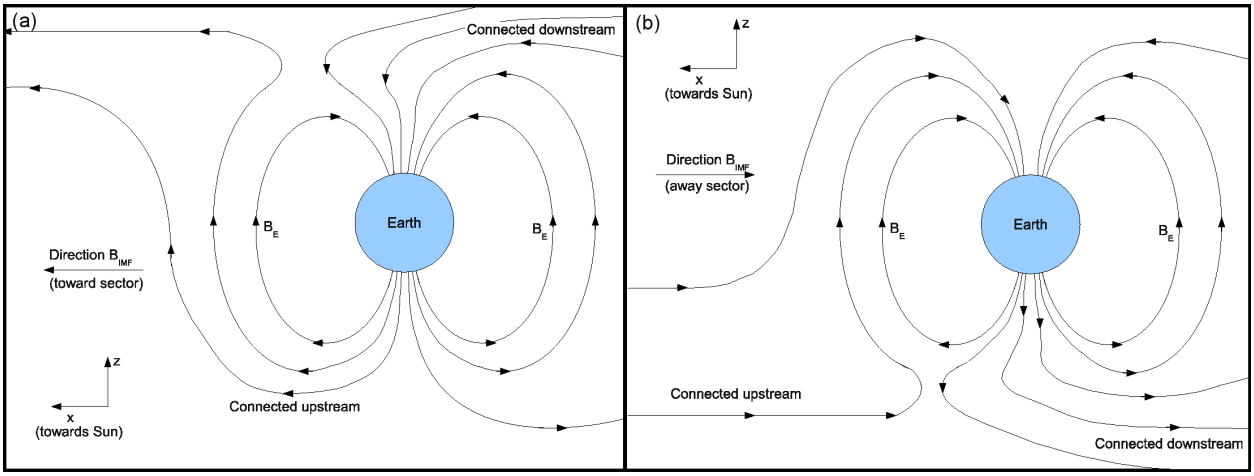

Figure 2.8: An illustration of reconnection when the IMF is purely away from or toward the Sun. Panel (a) shows the reconnected magnetic field lines in the north when the IMF is directed toward the Sun and panel (b) shows the reconnected magnetic field lines in the south when the IMF is directed away from the Sun.

which locations are connected magnetically upstream to the solar wind and which locations are connected downstream. These components also affect the location and intensity of "polar rain", or particle precipitation from the magnetosphere into the ionosphere, in the polar regions [*Newell et al.*, 2009].

2.3.3 Polar Rain

The term polar rain refers to charged particle precipitation along open field lines in the Earth's polar regions [*Newell et al.*, 2009]. While the IMF B_z component plays the largest role in controlling the magnetic reconnection rate, the IMF B_x and IMF B_y components control the location of magnetic reconnection on the magnetopause [*Newell et al.*, 2009]. The orientation of Earth's magnetic field affects the location of magnetic reconnection as well, which makes defining the coordinate system very important. For a description of the widely used coordinate systems, see Section 2.2.1.

The B_x component of the IMF determines the preferred hemisphere (north or south) where polar rain will be observed [*Newell et al.*, 2009]. Figure 2.8 shows how the IMF orientation in a solar sector can affect the morphology of the magnetic field lines. A negative IMF B_x (i.e., away from the Sun) is antiparallel to the dipolar geomagnetic field at high latitudes in the southern hemisphere (see panel (b) in Figure 2.8). When reconnection occurs here the

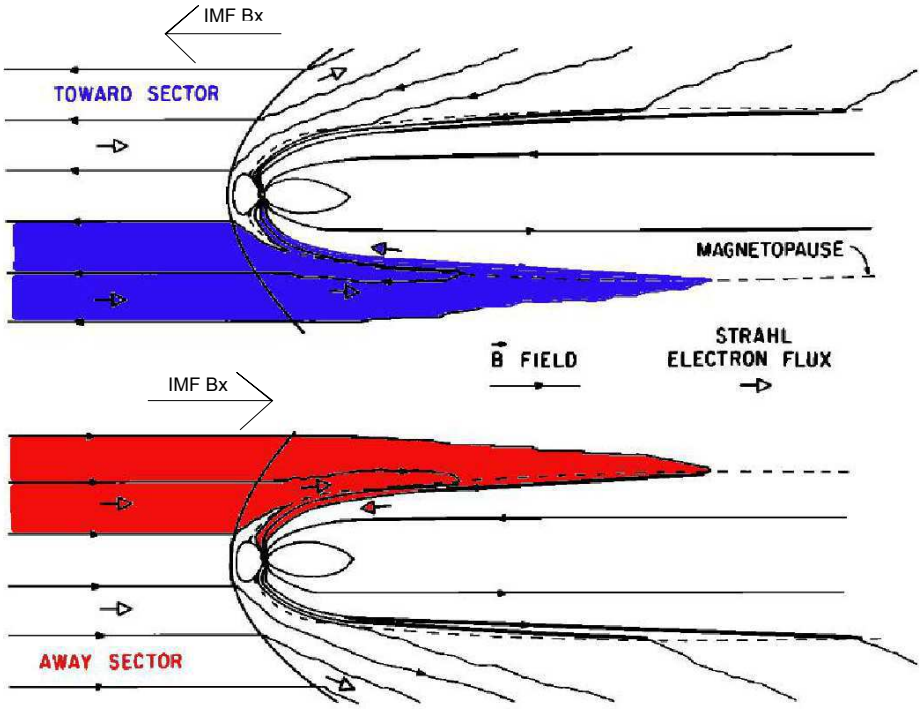

Figure 2.9: In a "toward" solar sector (top panel) the solar wind plasma has a path to precipitate into the southern polar ionosphere. In an "away" orientation (bottom panel) the solar wind plasma has a path to precipitate into the northern hemisphere. The hollow arrows represent the direction of the solar wind velocity, while the smaller solid arrows represent the direction of the IMF. Adapted from *Fairfield and Scudder* [1985].

newly "open" magnetic field lines in the northern hemisphere are connected upstream to the solar wind, while those in the southern hemisphere are connected downstream. This causes direct particle precipitation from the upstream solar wind to occur mostly in the northern hemisphere. A positive IMF B_x component (i.e., toward the Sun) causes the opposite to happen (see panel (a) in Figure 2.8), such that the particle precipitation occurs mostly in the southern hemisphere [*Fairfield and Scudder*, 1985]. This is also illustrated in Figure 2.9, which is an adaptation of a figure by *Fairfield and Scudder* [1985]. When the IMF is pointed toward the Sun (a "toward" solar sector with IMF $B_x > 0$) energetic charged particles precipitate into the southern hemisphere of the Earth, and when the IMF is pointed away from the Sun (an "away" solar sector with IMF $B_x < 0$) energetic charged particles precipitate into the northern hemisphere (as shown by the blue and red shaded regions in Figure 2.9, respectively).

The B_y component of the IMF, which determines the east–west location of the reconnection site on the magnetopause, determines the dawn–dusk energy flux gradient of the polar rain [*Newell et al.*, 2009]. This gradient is not necessarily smooth. A positive IMF B_y results in higher fluxes on the dawn side of the northern hemisphere [*Newell et al.*, 2009].

The energy flux of polar rain is less than 0.05 erg cm^{-2} s^{-1} 99% of the time, with typical values of 10^{-4} to 10^{-2} erg cm^{-2} s^{-1} in the favored hemisphere [*Newell et al.*, 2009]. When the polar rain energy flux increases to greater than 0.05 erg cm^{-2} s^{-1}, it is generally associated with an increase in solar wind plasma density rather than an increase in the solar wind particle energies [*Newell et al.*, 2009]. There have been recorded occurrences of single electron keV polar rain, with energy fluxes of over 1 erg cm^{-2} s^{-1}, which can occur several times a year [*Newell et al.*, 2009] and which are anticorrelated with the density of the solar wind, as predicted by *Fairfield and Scudder* [1985]. This is consistent with the properties of the solar wind strahl electrons, which was described in Section 2.1.3.

There is also a measured seasonal asymmetry in the intensity of the polar rain, where the summer hemisphere polar rain fluxes are more intense than the winter hemisphere polar rain fluxes [*Newell et al.*, 2009]. One reason given for this is that the dipole tilt of the geomangetic field leads to the summer magnetic field lines pointing more directly upstream towards the Sun, and therefore the precipitation is expected to be more intense in the summer hemisphere [*Newell et al.*, 2009].

Boudouridis et al. [2003] showed that solar wind pressure pulses have the ability to expand the auroral oval and cause increased particle precipitation. This effect is more pronounced when extended periods (longer than 30 minutes) of negative IMF B_z precede the pressure pulse. The increase in particle precipitation can lead to an increased plasma density in the lower ionosphere through ionization of the neutral species [*Kelley*, 1989; *Randall et al.*, 2005]. The increased ionization of the lower layers of the ionosphere can affect the way radio waves propagate in these regions.

2.3.4 Ionospheric Radio Wave Propagation

The ionosphere greatly affects radio communications through its variable index of refraction and its attenuation of electromagnetic waves. It is possible to model the ionosphere and

predict the propagation path of radio signals. These models tend to be steady state and smoothily varying, so they are best suited to model the ionosphere during quiet geomagnetic periods. This can be done using a model of ionospheric density, the Appleton–Hartree equation (Equation 2.1) and Snell's Law (Equation 2.6) [*Budden*, 1961]. The Appleton–Hartree equation describes the index of refraction of a plasma under the influence of a constant magnetic field, while Snell's Law describes the path of a radio signal through a plasma with a variable index of refraction. Equations 2.2–2.5 define the variables used in the Appleton-Hartree equation (Equation 2.1). Equation 2.2 gives the squared plasma frequency divided by the radio signal frequency, Equation 2.3 gives the electron collision frequency divided by the radio signal frequency, and Equations 2.4 and 2.5 give the electron cyclotron frequency divided by the radio signal frequency. The index of refraction, n, is dependant on the plasma density (N_e), the collision frequency of the electrons (ν_e), the frequency of the radio wave (ω), the background magnetic field (B_0) and the angle between the radio wave propagation path and the background magnetic field (θ). There are also some constants involved in the calculation, namely the electron charge (e), the permittivity of free space (ϵ_0) and the mass of an electron (m_e).

$$n^2 = 1 - \frac{X}{1 - iZ - \frac{Y_T^2}{2(1-X-iZ)} \pm [\frac{Y_T^4}{4(1-X-iZ)^2} + Y_L^2]^{1/2}} \tag{2.1}$$

$$X = \frac{N_e e^2}{\epsilon_0 m_e \omega^2} \tag{2.2}$$

$$Z = \frac{\nu_e}{\omega} \tag{2.3}$$

$$Y_L = \frac{B_0 e}{m_e \omega} cos\theta \tag{2.4}$$

$$Y_T = \frac{B_0 e}{m_e \omega} sin\theta \tag{2.5}$$

Snell's Law (Equation 2.6) describes the propagation of a radio wave across the boundary between two media with different indices of refraction. The variable n_1 is the index of refraction of the initial medium, n_2 is the index of refraction in the medium that the radio wave is entering, θ_I is the angle between the incident radio wave and the boundary normal

direction, and θ_T is the angle between the radio wave and the boundary normal direction in the second medium.

$$n_1 \sin\theta_I = n_2 \sin\theta_T \tag{2.6}$$

From Figure 2.6, in Section 2.3.1, it can be seen that the electron density increases from the E region to the F region. This means that, generally, the index of refraction is increasing. From Equation 2.6 it follows that the radio wave then bends towards the Earth if it is transmitted from Earth. Depending on the angle and frequency at which the radio signal is transmitted, it is possible to "bounce" the radio signal off the Earth's ionosphere and have it return to the Earth's surface. This is the key to over–the–horizon capabilities of high–frequency (HF) radars, for example. HF radars operate at frequencies between 3 and 30 MHz. The curving of the radio wave allows transmitted SuperDARN signals to be perpendicular to the geomagnetic field lines. The radio signal, at the proper frequency, can then be scattered from magnetic field–aligned irregularities and be measured at a receiver. This method of receiving radio signals from the ionosphere is described in more detail in Section 3.1.

In addition to being refracted, a radio wave is also attenuated as it travels through the ionosphere. This is due to electron collisions with the ions and neutrals in the ionosphere. The equation that describes the amount of attenuation experienced by the radio wave due to absorption is given by Equation 2.7 [*Blaunstein and Plohotniuc*, 2008]. A_κ is the absorption experienced by the radio wave in decibels (dB), where the integration is done over the path of the radio wave. I_0 is the initial intensity of the radio wave, and $I(\kappa)$ is the intensity of the radio wave as a function of the wavenumber, κ, after passing through the region of absorption. The constant c is the speed of light, ω_{pe} is the electron plasma frequency (given by Equation 2.8), ν_{en} is the collision frequency between the electrons and neutrals, ν_{ei} is the collision frequency between the electrons and the ions, and ω is the frequency of the radio wave. The equation is integrated over the path of absorption to determine the attenuation of the signal due to absorption, in decibels. Equation 2.7 holds for $\omega \gg \omega_H$ and $\omega > \omega_{pe}$, where ω_{pe} is the electron plasma frequency given by Equation 2.8 and ω_H is the electron gyrofrequency given by Equation 2.9 [*Blaunstein and Plohotniuc*, 2008].

$$A_\kappa = 10 \log_{10} \frac{I_0}{I(k)} = \frac{4.3}{c} \int \frac{\omega_{pe}^2(\nu_{en} + \nu_{ei})}{\omega^2 + (\nu_{en} + \nu_{ei})^2} ds \tag{2.7}$$

$$\omega_{pe}^2 = \frac{N_e e^2}{\epsilon_0 m_e} \tag{2.8}$$

$$\omega_H = \frac{B_0 e}{m_e} \tag{2.9}$$

From Equation 2.7 we can see that absorption is heavily dependant on the product of the plasma frequency and the electron collision frequency. If there is greatly enhanced electron density at low altitudes there will be a significant amount of radio wave absorption. Enhanced electron density corresponds to a higher plasma frequency, and there is also high particle densities at lower altitudes which result in a large electron collision frequency. This is why during significant particle precipitation events, when the ionospheric D–region plasma density is enhanced, there is often a drop–out of received radio signal from the ionosphere. Equation 2.7 also illustrates that the frequency of the radio signal has a significant role in the absorption of the radio wave. At higher frequencies, there will be less absorption in the ionosphere due to the squared radio frequency factor in the denominator.

Chapter 3

Instruments

Using data from instruments that measure ionospheric plasma flows, solar wind velocity and density, the IMF, and precipitating energetic particles, it is possible to investigate how the orientation of the solar sector angle affects the Earth's ionosphere. The following sections include basic information on the instruments used in this study.

3.1 Super Dual Auroral Radar Network

The super dual auroral radar network (SuperDARN) radars operate at frequencies between 8 and 20 MHz [*Greenwald et al.*, 1995]. The coverage of the SuperDARN network for both the north and south hemispheres is shown in Figure 3.1. The three letter acronyms refer to the locations of the SuperDARN radar sites. The radio waves transmitted by SuperDARN propagate up to the E and F regions of the ionosphere, where the radio waves are able to coherently scatter from plasma wave structures oriented along the magnetic field lines. The plasma structures that scatter SuperDARN waves have wavelengths that are between 18.75 and 7.50 meters, depending on the radar frequency being used. SuperDARN receivers and transmitters are co–located, using the same antenna array. Therefore, for the radar to receive a signal (an echo) from the plasma structure, the radio wave must scatter back towards the radar from an ionospheric irregularity that has a wavelength half that of the radio wave [*Greenwald et al.*, 1995]. The ionospheric plasma density affects the propagation path of the radio waves by refraction (Section 2.3.4). This in turn affects the location where the radio wave can scatter from plasma wave structures. If the signal is not perpendicular to the magnetic field, and therefore not perpendicular to the field–aligned irregularities, scatter cannot occur. This is why having a variable frequency capability was a requirement

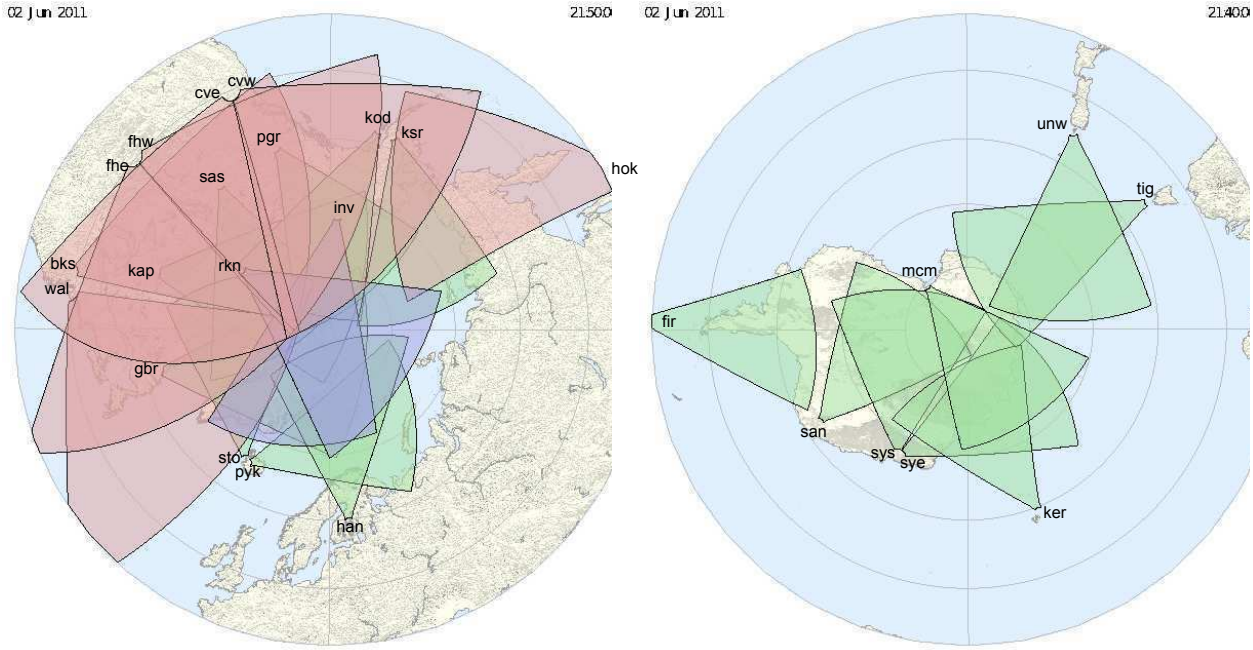

Figure 3.1: The SuperDARN fields of view with the three letter acronyms of the radar sites. The northern hemisphere SuperDARN coverage is shown on the left, and the southern hemisphere SuperDARN coverage is shown on the right.

for the SuperDARN radars [*Greenwald et al.*, 1995], as different radio frequencies refract differently through the same plasma density gradient. An ionized D region can also affect echo occurrence, as the radio wave can be absorbed by the D–region plasma [*Hargreaves*, 1992, and Section 2.3.4]. In addition to propagation effects, if there are insufficient irregularities of an appropriate wavelength to scatter SuperDARN radio waves, there will also be no ionospheric scatter back towards the radar. All of these processes can affect the amount of scatter arriving at a SuperDARN receiver during a SuperDARN scan. A typical SuperDARN scan therefore does not have echoes in every possible measurement location, but these radars are useful in understanding the conditions in the ionosphere that affect radio wave propagation and irregularity production. After receiving the scattered radio signal at the radar array, it is possible to determine the component of the plasma drift velocity along the beam from the doppler shift of the radio wave. When two radars record data from the same area it is possible to construct from the two measured drift components a full plasma drift vector in the plane perpendicular to the magnetic field direction [*Greenwald et al.*, 1995].

The SuperDARN radar transmits a sequence of radio wave pulses, and the backscattered

signal from these pulses is then measured at the same radar. The pulse sequence has different lags between the pulses, allowing for an autocorrelation function (ACF) to be created from the received signals. The rate of change in the phase between the lags in the ACF gives the velocity of the plasma along the beam, while the decay of the ACF determines how well correlated the plasma waves are in the measurement volume. Ionospheric scatter echoes generally have a fast decay in the ACF, while the ACF of ground scatter echoes generally does not decay. The ground scatter echoes also should have zero doppler shift associated with them, as the ground should not be moving.

SuperDARN radars make it possible to measure the $\mathbf{E} \times \mathbf{B}$ drift of the ionospheric plasma on a global scale as often as every minute. The potential patterns in Figure 2.7 in Section 2.3.2 are averaged ionospheric convection patterns obtained from 6 years of SuperDARN data. With SuperDARN radars it is possible to monitor, minute by minute, how the ionospheric convection pattern changes as space weather conditions change.

3.2 OMNI Spacecraft

The OMNI data set [*King and Papitashvili*, 2012] consists of measurements taken by four different unmanned spacecraft. The data are provided by the Goddard Space Physics Data Facility, found at `http://omniweb.gsfc.nasa.gov/`. In this thesis, the OMNI data used had a cadence of one minute. The observations are propagated to a common position immediately upstream of the Earth's bow shock [*King and Papitashvili*, 2012]. The bow shock changes position depending on the solar wind dynamic pressure being exerted on the Earth's magnetosphere. The position that the OMNI data is mapped to is therefore not constant. On average, the apex of the parabolic bow shock is at 14.6 R_E in the sunward direction [*Fairfield*, 1971]. To confirm that this shifting method was providing accurate results, OMNI compares shifted data from several spacecraft.

The IMF, solar wind plasma velocity and solar wind plasma density measurements were used in the analysis for this thesis. The minute time–stamp used for the data refers to the start of the interval over which the data were averaged. The four spacecraft contributing to the OMNI data set were the Advanced Composition Explorer (ACE) [*Stone et al.*, 1998], the

Wind spacecraft [*Ogilvie et al.*, 1995; *Lepping et al.*, 1995], the Interplanetary Monitoring Platform 8 (IMP–8) [*Paularena and King*, 1999] and the Geotail spacecraft [*Kokubun et al.*, 1994; *Mukai et al.*, 1994]. Geotail measurements were included in the OMNI data set from March 15, 1995 to December 31, 2006, IMP–8 measurements were included in the OMNI data set from January 1, 1995 to June 9, 2000, ACE measurements were included in the OMNI data set from February 5, 1998 to the present and WIND measurements were included in the OMNI data set from January 1, 1995 to the present. Each of these spacecraft are briefly described below. [*King and Papitashvili*, 2012]

3.2.1 Advanced Composition Explorer (ACE)

The ACE spacecraft [*Stone et al.*, 1998] is situated at the L1 Lagrangian point between the Earth and the Sun, well outside the Earth's magnetosphere at about 240 R_E upstream of the Earth. Instruments on board measure parameters of the solar wind and the IMF. The particle detectors on the spacecraft can measure ions from the solar wind and galactic cosmic rays with energies in the range from 100 eV to several hundred MeV. The instruments monitoring the solar wind and IMF are the Solar Wind Electron, Proton, and Alpha Monitor (SWEPAM) [*McComas et al.*, 1998] and a twin triaxial fluxgate Magnetometer (MAG) [*Smith et al.*, 1998]. SWEPAM measures characteristics of the solar wind in three dimensions, with electron energies ranging from approximately 1 to 900 eV and ion energies ranging from 0.26 to 36 keV [*Stone et al.*, 1998]. With MAG and SWEPAM the magnetic field vector can be determined, along with the solar wind density, velocity and temperature with a time resolution of at least one minute. ACE provides advance knowledge of incoming solar wind conditions at the Earth.

3.2.2 WIND

The WIND spacecraft is normally located approximately 210 R_E between the Sun and the Earth. One of the purposes of this satellite is to measure the solar wind "strahl" (Section 2.1.2). This is one goal of a set of sensors on board the spacecraft called the Solar Wind Experiment (SWE) [*Ogilvie et al.*, 1995]. For measuring general parameters of the solar

wind, such as ion velocity, density and temperature a Faraday cup (FC) instrument is used, which is also part of the SWE. Using the SWE sensors, the solar wind proton velocity (3 components) can be measured in the range of 200–1250 km/s with an error of 3%, the solar wind proton density can be measured in the range of 0.1–200 cm^{-3} with an error of 10% and the solar wind thermal speed can be measured in the range of 0–200 km/s with an error of 10% [*Ogilvie et al.*, 1995]. The time resolution of this solar wind data can be on the order of a couple of seconds, depending on the operational mode [*Ogilvie et al.*, 1995]. There is also a magnetometer on board the spacecraft that is capable of making three dimensional measurements of the magnetic field. As with the Advanced Composition Explorer, the magnetometer is a dual triaxial fluxgate magnetometer [*Lepping et al.*, 1995]. This instrument takes 10.9 magnetic field vector measurements per second when in standard operation [*Lepping et al.*, 1995]. The time resolution is degraded to 1–minute for the OMNI data set, but this is more suitable for comparison with SuperDARN data, which has a typical time resolution of 1–2 minutes.

3.2.3 IMP–8

The average radius of the IMP–8 spacecraft's orbit is 35 R_E, with the apogee distance being 45 R_E and the perigee distance being 22 R_E in the extreme cases [*Paularena and King*, 1999]. The satellite did not continuously measure the solar wind as it only spent about 7 to 8 days of its orbital period of approximately 12.5 days in the solar wind [*Paularena and King*, 1999]. The IMP–8 spacecraft had both a Faraday cup and a triaxial fluxgate magnetometer among its instruments [*Paularena and King*, 1999]. With these instruments it was possible to take measurements of the solar wind plasma velocity, density and temperature as well as the IMF vector. The satellite is not always outside the Earth's magnetosphere, and therefore the measurements have multi–day gaps. While this is not ideal, IMP–8 does provide measurements closer to the bow shock of the Earth than ACE and Wind. This allows the time shifting technique to be tested when shifting the ACE and Wind spacecrafts' measurements to the bow shock.

3.2.4 Geotail

For the first couple years of the Geotail spacecraft's operational lifetime, it was located mainly in the Earth's magnetotail, and therefore was not measuring the solar wind. After this initial phase, the spacecraft was maneuvered into an orbit with an apogee of 30 R_E and a perigee of 8 R_E [*Kokubun et al.*, 1994]. The magnetic field is measured using the spacecraft's dual three–axis fluxgate magnetometers [*Kokubun et al.*, 1994]. The plasma density and velocity vectors are measured using a low energy particle (LEP) instrument [*Mukai et al.*, 1994]. This LEP instrument is capable of measuring ion energies of 140 eV/Q to 8 keV/Q where Q is the charge of the particle being measured [*Mukai et al.*, 1994]. Though this spacecraft is not consistently measuring the solar wind, it does give complementary measurement data to that of the other spacecraft listed above.

3.3 Defense Meteorological Satellites Program (DMSP)

The Defense Meteorological Satellites Program (DMSP) was first devised for the American military. They decided to create their own branch of weather forecasting for troops in the field to give them a tactical edge in military missions [*Curtis and Adams*, 1987]. The satellites orbit the Earth with a period of approximately 101 minutes. The current DMSP satellites have onboard an instrument that determines the energy and density of precipitating charged particles [*Hardy et al.*, 1984]. These data are not included directly in this report, but parameters derived from these data will be examined to determine if solar sector orientation correlates with characteristics of the polar rain precipitating into the north and south polar regions. If a correlation exists, it may be possible to determine if these precipitating particles have enough energy to alter the ionization at E– and D–region altitudes. Figure 3.2 shows DMSP data during a pass of a keV polar rain event. The top two panels are the total energy flux and the average energy of the electrons (black dots) and ions (red dots) and the bottom two panels are the energy flux of precipitating electrons and ions, respectively, where the energy flux is represented by the color bar. The polar rain electrons have a spread of energies between 10^2 eV and 10^4 eV, and are detected poleward of approximately -70° magnetic

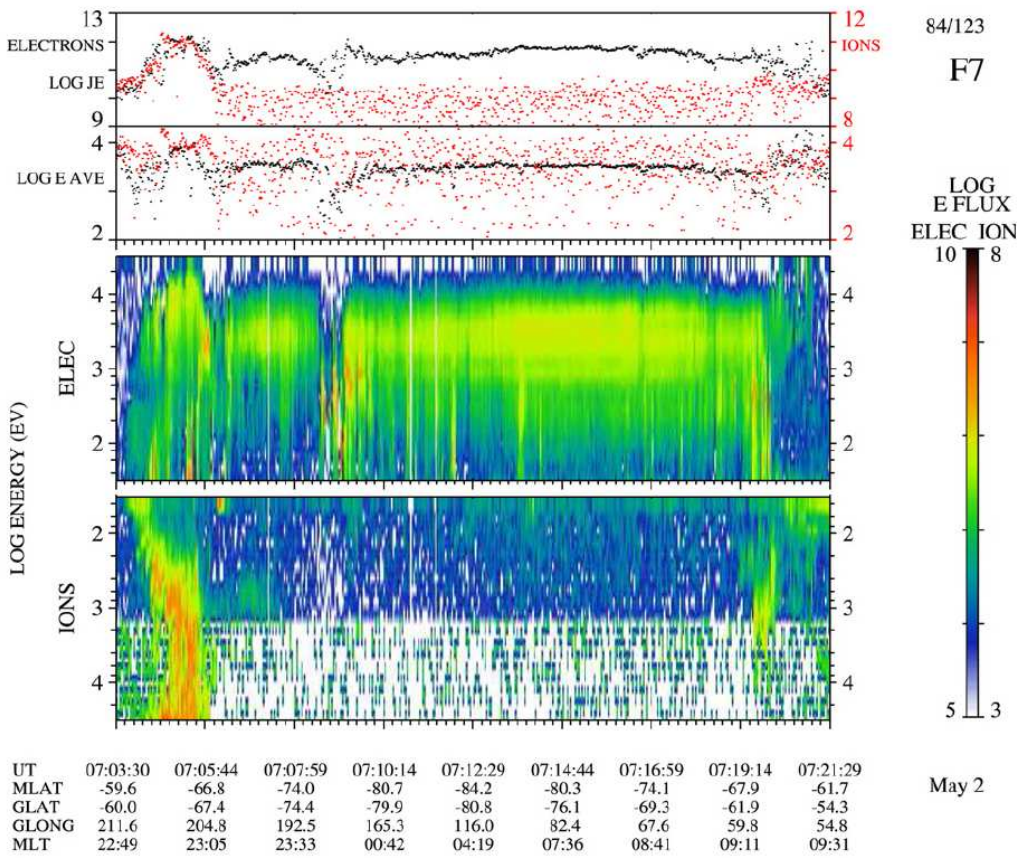

Figure 3.2: Energy spectrograms of data retrieved from a DMSP satellite passing over the auroral zone and polar cap of the Earth. These plots show the flux and energy of ions and electrons entering the Earth's ionosphere. The top panel shows the total energy flux and the second panel shows the average energy of the particles. The red dots give the value for the ions and the black dots give the value for the electrons. The bottom two panels show the flux of electrons and ions precipitating at different energies. [From *Newell et al.*, 2009]

latitude for this pass.

3.3.1 DMSP Indices

The DMSP hemispherical power (HP) and midnight boundary index (MBI) data were provided by the CEDAR Database and the Air Force Research Laboratory (`http://cedarweb.hao.ucar.edu/wiki/index.php`) [B. Emery, personal communication]. The MBI consists of times and latitudes when DMSP satellites crossed the equatorward edge of the auroral zone in the north and the south. Sharp changes in precipitating electron characteristics define the

location of the equatorward auroral boundary [*Gussenhoven et al.*, 1981]. The hemispherical power is an estimate of the total energy being deposited into a hemisphere's auroral zone and polar cap by electron precipitation. A previously created statistical ionospheric particle precipitation map is fitted to the electron fluxes measured by the DMSP satellite along the satellite track. The hemispherical power is calculated through the following equation:

$$HP = \langle PHI \rangle \times A(I) \times f(MLT)[Evans,\ 1987] \tag{3.1}$$

The parameters of the statistical ionospheric climate map are used to calculate a hemispherical power for a satellite pass, where $\langle PHI \rangle$ is the measured electron energy flux along the spacecraft trajectory, A(I) is the area of the auroral oval with a geomagnetic activity level of I, as determined from $\langle PHI \rangle$, and f(MLT) is a factor that accounts for the different satellite trajectories through the polar cap and auroral oval. It essentially extrapolates electron energy fluxes measured at different magnetic local times to the entire polar cap and auroral oval [*Evans*, 1987].

One hemispherical power (HP) and one midnight boundary index (MBI) value is obtained for each satellite pass poleward of the equatorward auroral boundary. There are several DMSP satellites and their passes occur at irregular intervals throughout the day. Both the HP and the MBI data sets were averaged to match the time resolution of the other data sets (one–day resolution).

3.4 Galactic Cosmic Ray Detector

The galactic cosmic ray (GCR) detector used in this study detects near–thermal neutrons that are created when high energy GCRs, or particles produced from collisions with GCRs, interact with the Earth's atmosphere. This detection is accomplished by measuring the charged particles that are often produced when a neutron is absorbed by $^{10}BF_3$ (boron trifluoride, where the boron has an atomic weight of 10) or ^3He [*Clem and Dorman*, 2000]. A neutron monitor consists of neutron proportional tubes filled with $^{10}BF_3$ or ^3He, surrounded by a moderator material and a lead target. The neutron proportional tubes count the charged particles produced by the neutron–nucleus interaction [*Clem and Dorman*, 2000]. Around

each of these counters is a moderator. This moderator is used to reflect low energy neutrons and slow down other neutrons to increase the probability of detection [*Clem and Dorman*, 2000]. Surrounding all of this is a lead target, which absorbs secondary neutrons produced in the collisions. Then, around this lead shielding, is another moderator that disallows low energy neutrons produced in the immediate surroundings from entering the detector. This moderator also absorbs any low energy neutrons produced by particle interactions with the lead shielding [*Clem and Dorman*, 2000]. There have been previous studies showing that the magnitude of the IMF [*Cane et al.*, 1999] and the Earth's atmosphere [*Clem and Dorman*, 2000] can affect the amount of GCRs reaching the Earth's surface.

GCRs have been shown to be correlated with the Earth's low altitude cloud cover [*Marsh and Svensmark*, 2000], though it is a controversial topic. A different study by *Sloan and Wolfendale* [2008] argues that the amount of cloud cover affected by GCRs is actually quite small. However, it is still worth investigating if GCRs are affected during solar sector boundary crossings, since it is possible that GCRs are related to tropospheric weather.

3.4.1 Galactic Cosmic Rays Data Set

The cosmic ray data used in this study are from the neutron monitors located at McMurdo, Antarctica and Thule, Greenland, and they are provided by the Bartol Research Institute (`http://neutronm.bartol.udel.edu/`). These sites, along with 9 other neutron monitoring sites, are operated by the University of Delaware Bartol Research Institute Neutron Monitor Program. The cosmic ray data consist of hourly counts of the number of GCR–induced neutrons. From the available parameters, both the raw, uncorrected counts and the corrected counts of neutrons were used in this study. The corrected counts have the atmospheric pressure taken into account as this affects the neutron production. For comparison with the other data sets, an average neutron count was calculated for each day.

Chapter 4

Data Analysis

4.1 Summary of Solar Wind and IMF Properties

Long term fluctuations in the solar wind and IMF were analyzed using the OMNI data set (Section 3.2). Figure 4.1 shows an average taken every 27 days of the solar wind speed (top panel) and solar wind proton density (bottom panel), with the vertical black lines representing the standard deviation of the one–day averages of the data. A 27–day average was chosen as it is approximately the solar synodic rotation period. This removes the 27–day solar rotation periodicity from the data, revealing long term trends in the data. The average solar wind speed in 2003 is consistently greater than at any other time during the solar cycle. The year 2003 was early in the declining phase of solar cycle 23, following the solar maximum in 2000. The solar wind was also relatively fast in 2008 (approximately 550 km/s on average), but decreased in 2009 to just above 300 km/s, on average. In 2008 there were many corotating interaction regions (CIRs) which produce high speed solar wind streams [*Mason et al.*, 2009], and these could account for the relatively high solar wind speeds during 2008. The year 2009 was a deep solar minimum and the beginning of solar cycle 24.

In 2003 and in 2008 there is, on average, a lower solar wind proton density than during the surrounding years, which is opposite of the trend seen in the solar wind speed. Previous studies have noted this anticorrelation between the solar wind speed and solar wind density [*Neugebauer and Snyder*, 1966; *Hundhausen et al.*, 1970].

Figure 4.2 displays an average taken every 27 days of the IMF strength and the three GSM components. The GSM coordinate system is described in Section 2.2.1. The vertical lines on the plots represent the standard deviation of the one–day averaged data over 27 days. The three components of the IMF affect the location of magnetic reconnection between the

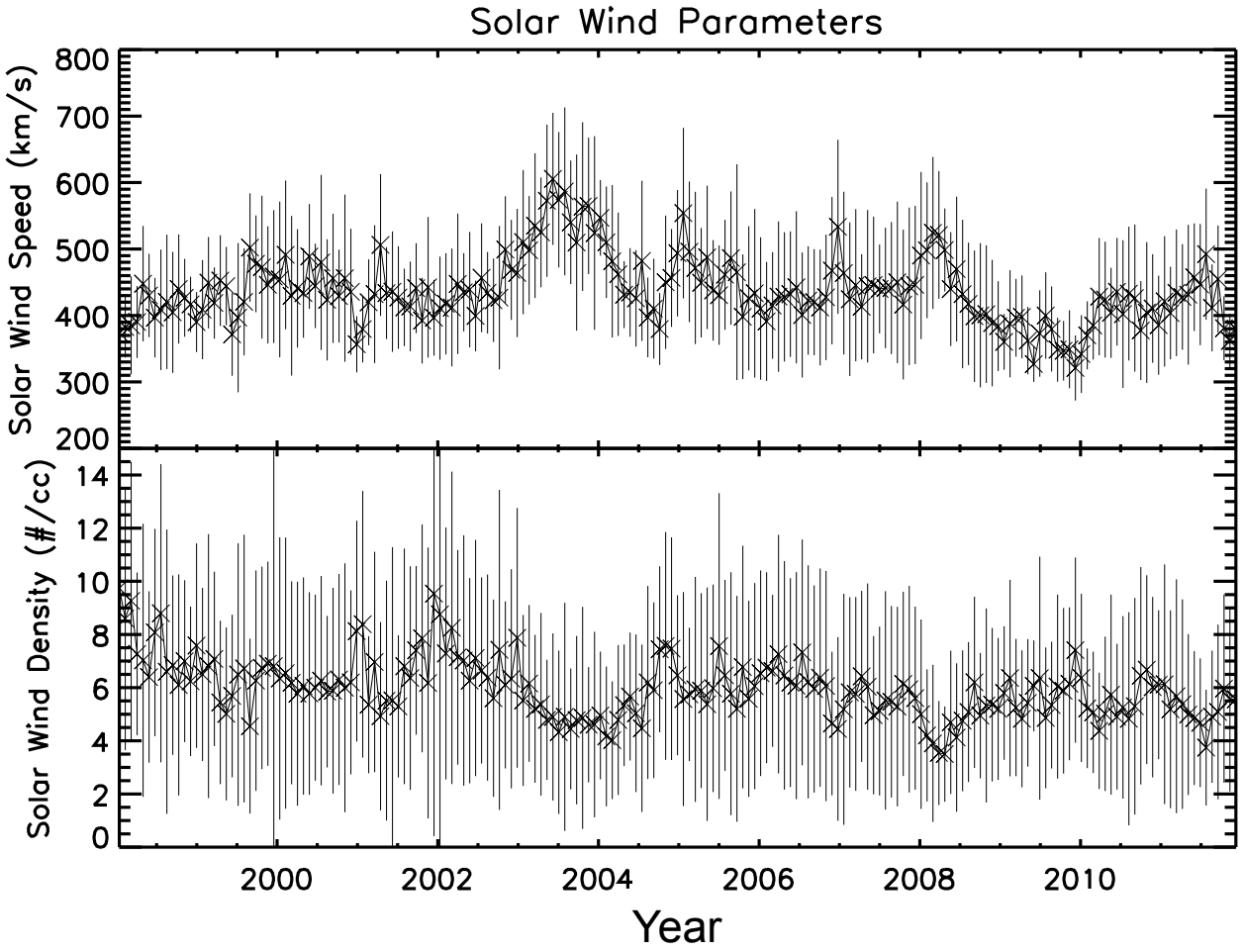

Figure 4.1: 27–day averages of solar wind plasma speed (top panel) and plasma density (bottom panel) from 1998–2011 inclusive. The vertical lines represent the standard deviation of the daily averages for each 27–day interval.

IMF and the Earth's magnetosphere, which in turn affects the shape of the magnetosphere and the flux and location of energetic particle precipitation at high latitudes. The B_y and B_x components of the IMF are generally anticorrelated. This is due to the fact that the Parker spiral is typically at an angle of 45° at the Earth (Figure 2.3). In "toward" solar sectors, the B_x component of the IMF is generally positive, and the B_y component of the IMF is generally negative. The opposite occurs for "away" sectors, where the B_x component is generally negative and the B_y component is generally positive.

During the years 1998–2004 all components of the IMF had large standard deviations compared to the standard deviation values during 2006–2012. The small standard deviation after 2005 coincides with the beginning of the relatively quiet solar minimum. The large

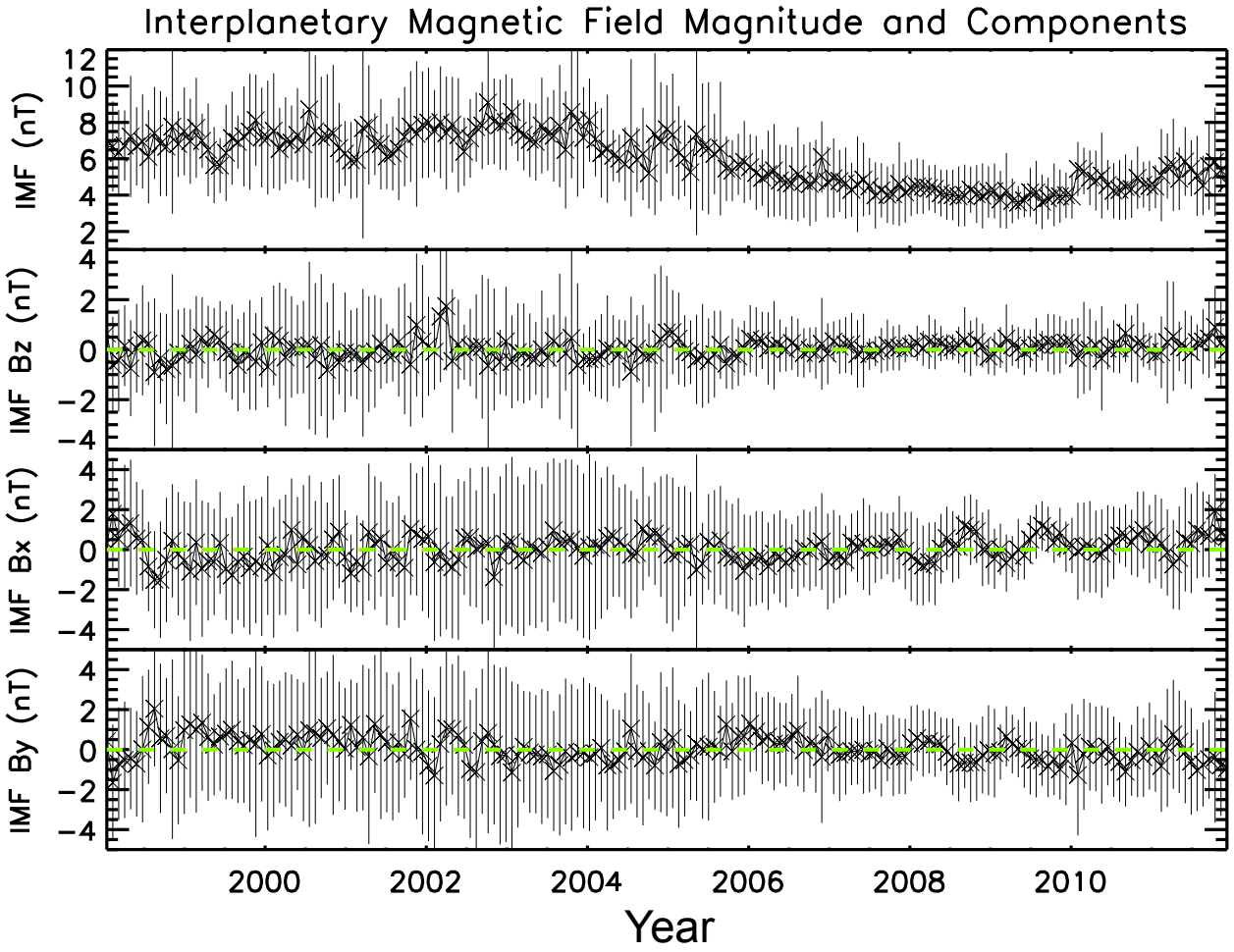

Figure 4.2: 27–day averages of OMNI IMF magnitude and GSM components. The vertical lines represent one standard deviation calculated from the one–day averages of the IMF, and the green dashed line is at 0 nT magnetic field (a reference).

standard deviation during 1998–2004 indicates that there was large variability of the IMF during solar cycle 23.

The magnitude of the IMF averaged every 27 days is presented in the top panel of Figure 4.2. In the years 1998–2004 the IMF was approximately 7 nT on average, and then decreased to an average of 4 nT in the years 2004–2008. In 2010 and 2011 the IMF increased slightly to an average value of 5 nT. The weak IMF after 2004 is consistent with the unusually weak solar activity during solar cycle 24.

The solar sector boundary crossings and their polarities ("away–to–toward" or "toward–to–away") were identified using the OMNI magnetic field data. The sector boundary crossings occur as the Earth passes through the heliospheric current sheet (HCS). The data obtained

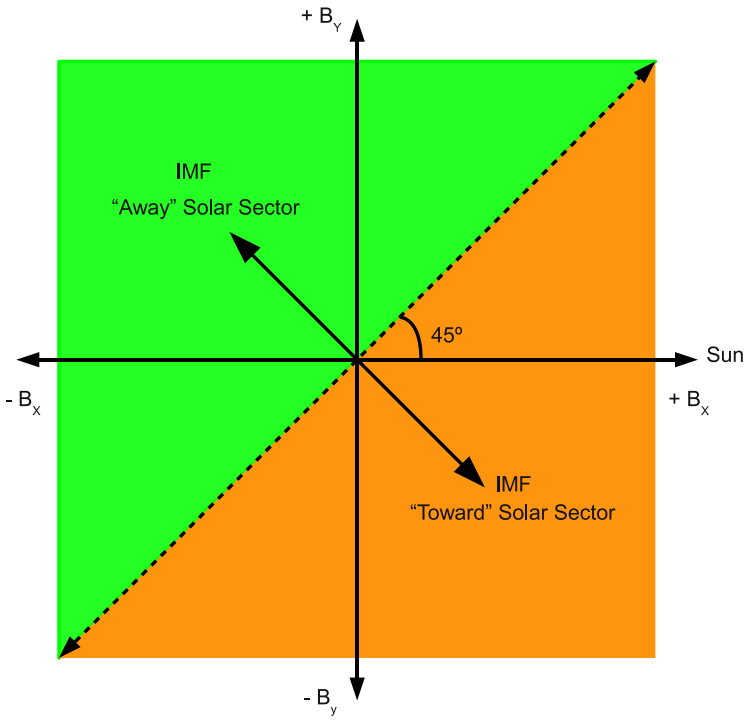

Figure 4.3: Depiction of the definition of angles used to determine solar sector orientation in this study.

from the OMNI database have a time resolution of 1 minute, and therefore the sector boundary crossings have 1–minute time resolution. The IMF B_x and B_y values in GSM coordinates were used to calculate the solar sector angle by taking the inverse tangent of B_y/B_x, which results in 0° pointing radially towards the Sun.

At Earth the IMF Parker Spiral is approximately 45° from radial, so an "away" sector includes the angles in the ranges 45° to 180° and −135° to −180°. The "toward" sector includes the angles in the range −135° to 45°. This is displayed graphically in Figure 4.3.

For every point in the IMF time series, the algorithm evaluates sector angles before and after that point. The number of away and toward IMF sector angle values before and after a specific time are used to quantify the likelihood that the central time is a sector boundary crossing. A percentage is assigned to the central time, based on how likely it was that a sector crossing occurred at this time. This percentage is calculated using the following equations:

$$P_1 = \frac{N_A^- + N_T^+}{N} \times 100\% \tag{4.1}$$

$$P_2 = \frac{N_T^- + N_A^+}{N} \times 100\% \tag{4.2}$$

Where N is the total number of data points before or after the current time, the subscript T refers to points in a toward sector orientation, the subscript A refers to points in an away sector orientation, the superscript '+' refers to points after the current time, and the superscript '-' refers to points before the current time. P_1 is the likelihood that the central time is an "away–to–toward" transition, and P_2 is the likelihood of a "toward–to–away" transition. Either P_1 or P_2 will reach a maximum at the time most likely to be a boundary sector crossing. The higher percentage of the two equations is recorded, as well as the polarity of the potential crossing for every point in the IMF time series. The algorithm worked very successfully to identify sector boundaries with a user defined time of N=1500 minutes before and after the central time and a minimum P_1 or P_2 of 68%.

The crossings were confirmed by visual inspection of the sector angle time series, with the most likely boundary crossing times indicated on time series plots of the solar sector angle. Examples of these are presented in Figures 4.4 and 4.5. Figure 4.4 is an example of a typical two–sector structure, when the Earth is above the HCS for half a solar rotation and below the HCS for the other half of the solar rotation. This periodicity persisted for approximately two and a half years (2002–2004.5). Figure 4.5 is an example of a much less regular series of solar sector crossings. This is more common in the OMNI data set. For just under nine years of IMF data the program identified 957 sector boundary crossings. There were 18 events that would have been selected by eye but were not identified by the automated method. These missing crossings were due either to gaps in the IMF data or due to the sector angle not having a rapid change from one sector to the other. The missing sector crossings were added manually to the sector boundary crossing list with a reduced level of confidence (60%).

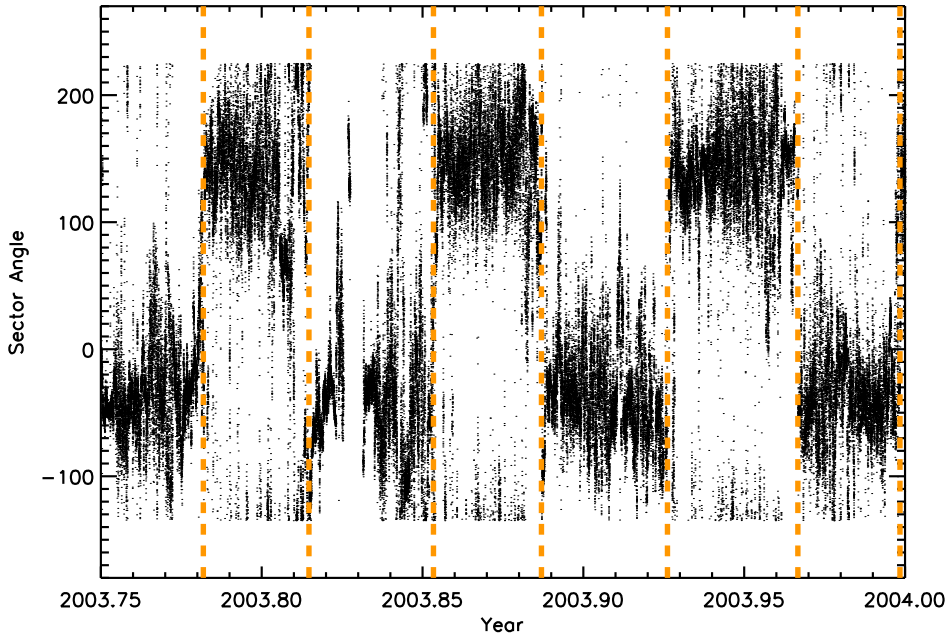

Figure 4.4: Solar sector angle during the last 3 months of 2003, with the boundary crossings overlaid (orange dashed lines)

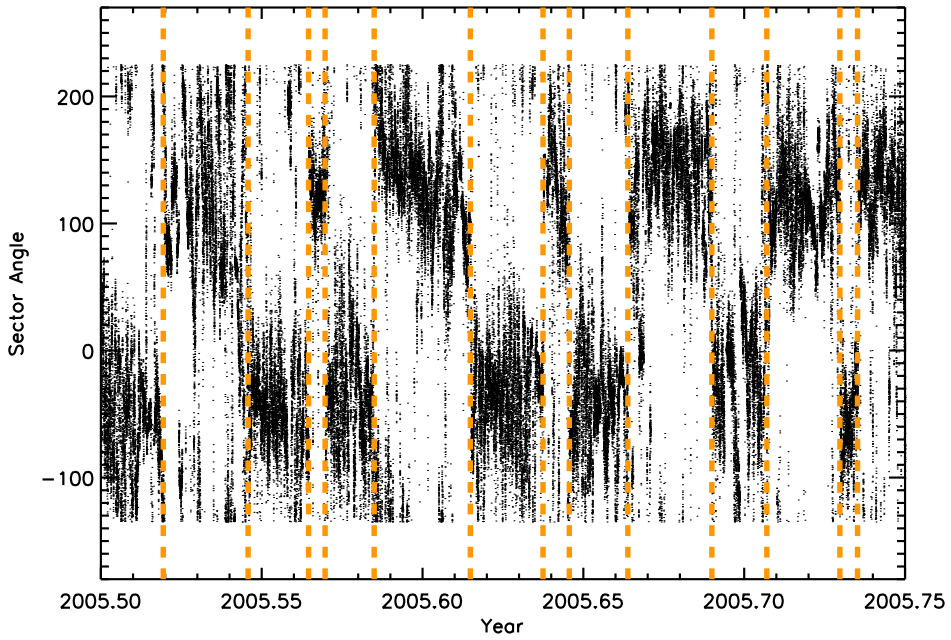

Figure 4.5: Solar sector angle during the 3rd quarter of 2005, with the boundary crossings overlaid (orange dashed lines)

A superposed epoch analysis of solar sector boundary crossings was performed with the automatically detected solar sector boundaries as the zero epoch reference time. A superposed epoch analysis consists of averaging time series centered on a particular phenomenon of interest, such as the sector boundary crossing in this case. Only isolated boundary crossings were used in the superposed epoch analysis, and these were defined as having no other boundary crossings within 5 days, with a minimum percentage of 68%. The superposed epoch analysis was also repeated using all boundaries, including those detected visually, and the results were very similar.

The superposed epoch plots of the IMF magnitude are shown in Figure 4.6. The top panel includes transitions from a toward to an away solar sector, and the bottom panel includes transitions from an away to a toward solar sector. There were 153 events with a transition from toward to away, and 138 events with a transition from away to toward. In both cases, the magnitude of the IMF increases by 30% across the sector boundary. This is consistent with past studies [*Liu et al.*, 2012]. The IMF returns to pre–boundary values in approximately 2 days. Galactic cosmic rays are known to be affected by changes in the IMF magnitude over time scales of a solar cycle (11 years) [*Cane et al.*, 1999], though the IMF changes presented here are over shorter time scales (days).

When the Earth crosses the heliospheric current sheet (a solar sector boundary crossing), it is expected that the speed of the solar wind plasma will decrease and the density of the solar wind plasma will increase, as seen in past studies [*Gosling and Pizzo*, 1999; *Liu et al.*, 2012]. A superposed epoch analysis was performed on both the one–day averages of solar wind speed and density. Figures 4.7 and 4.8 summarize the results of this analysis. The values are presented as a percentage difference from the 10–day mean.

As seen in Figure 4.7, the average solar wind speed decreases during the day before the sector boundary crossing by approximately 15% from the 10–day mean for both polarities of crossings. The top panel includes 153 toward–to–away events, while the bottom panel includes 138 away–to–toward events. Following the sector boundary crossing the solar wind speed begins to increase, and two days after the crossing the speed has returned to pre–crossing values.

The superposed epoch plots of solar wind density are presented in Figure 4.8. Again, the

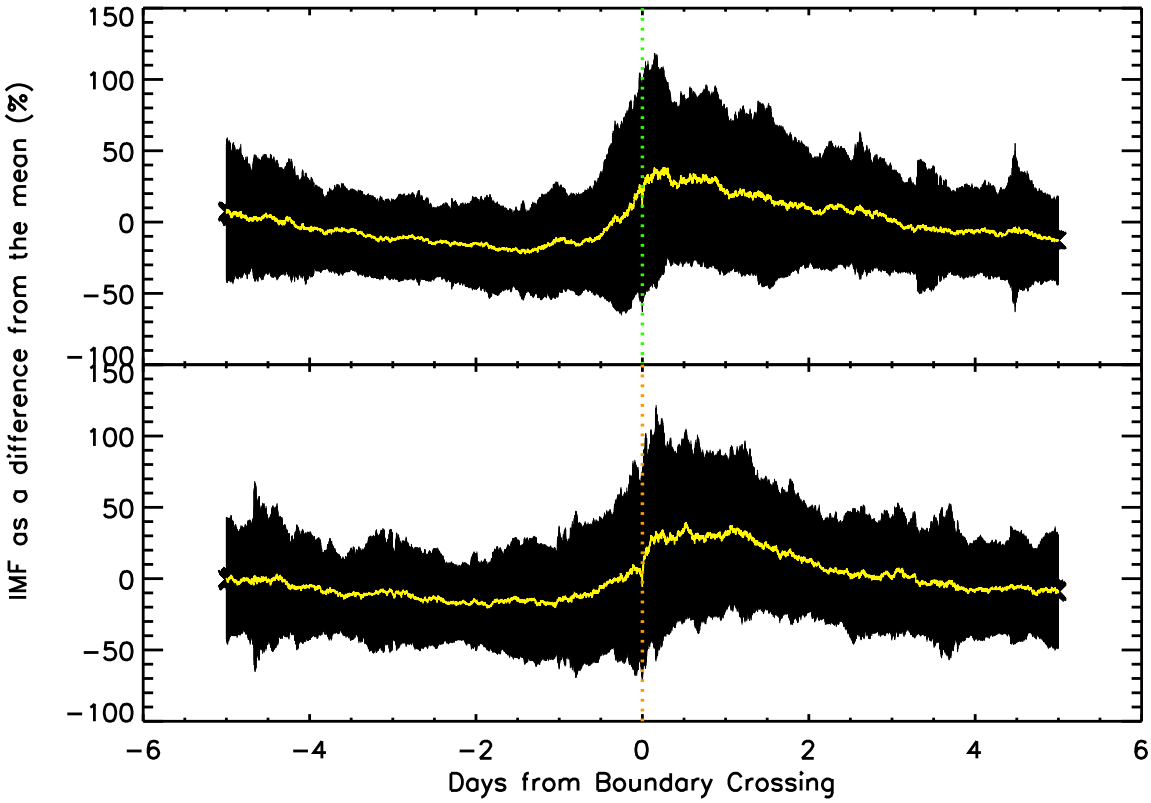

Figure 4.6: Superposed epoch plots of the IMF magnitude in terms of the percentage difference from the 10–day mean value. The top panel includes 153 toward–to–away events, and the bottom panel includes 138 away–to–toward events. The yellow line gives the mean of the data, while the black vertical lines give the standard deviation.

top panel includes 153 toward–to–away events, and the bottom panel includes 138 away–to–toward events. The one–day averaged solar wind density increases to approximately 200% above the 10–day mean for both polarities of sector boundary crossings. The day before the sector boundary crossing, the solar wind density increases until the sector boundary crossing when it reaches its peak value. The solar wind density decreases to its pre–sector boundary crossing levels about two days after the crossing.

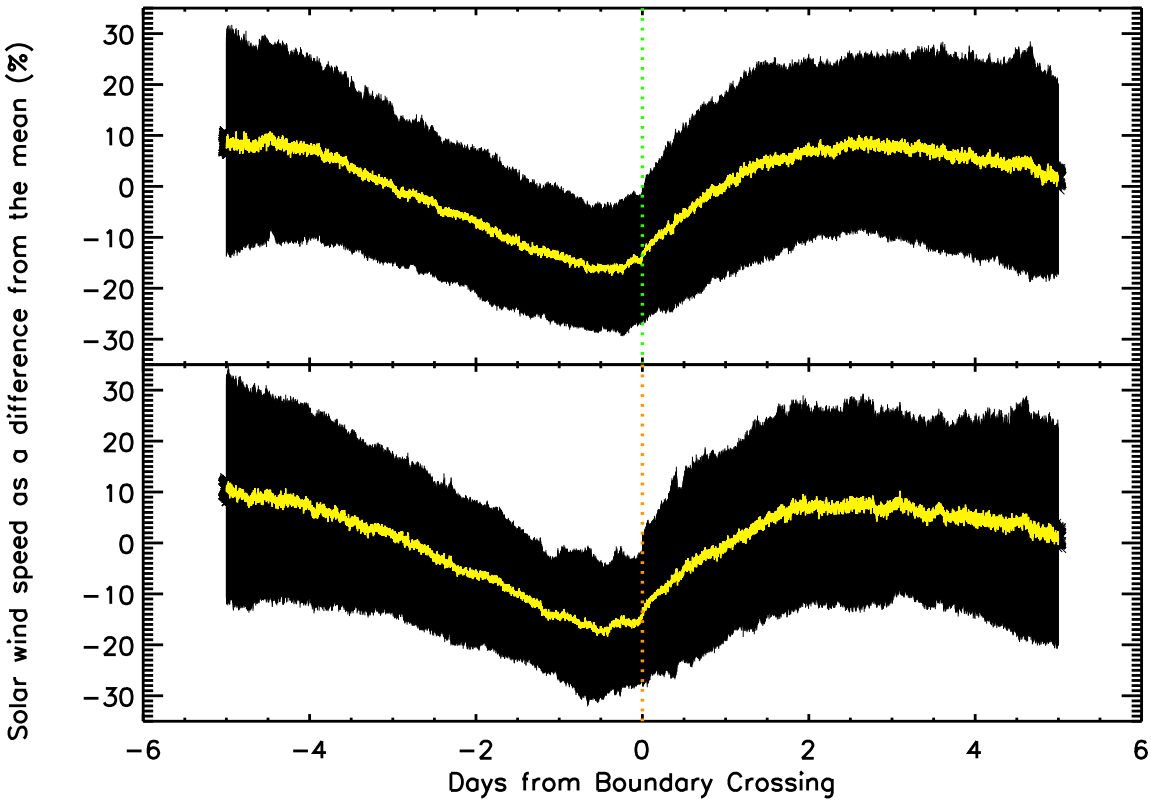

Figure 4.7: Superposed epoch plots of the solar wind speed in terms of the percentage difference from the 10–day mean value. The top panel includes 153 toward–to–away events, and the bottom panel includes 138 away–to–toward events. The yellow line gives the mean of the data, while the black vertical lines give the standard deviation.

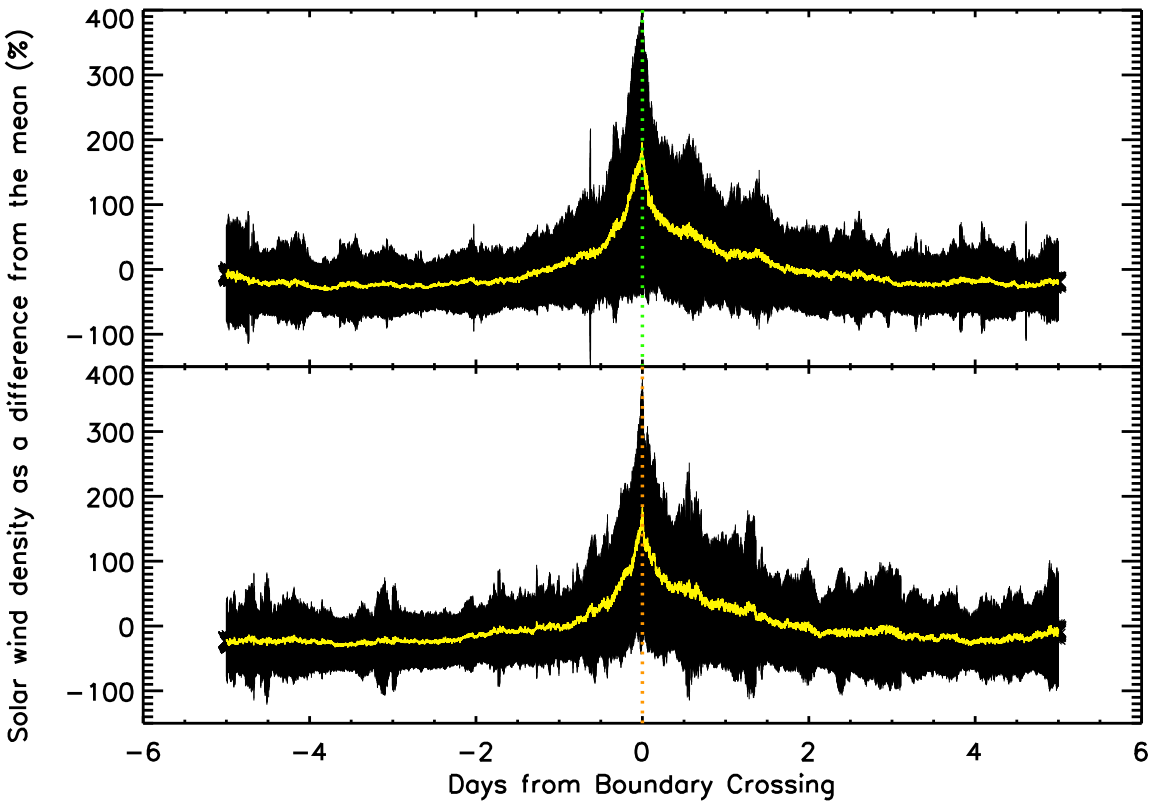

Figure 4.8: Superposed epoch plots of the solar wind density in terms of the percentage difference from the 10–day mean value. The top panel includes 153 toward–to–away events, and the bottom panel includes 138 away–to–toward events. The yellow line gives the mean of the data, while the black vertical lines give the standard deviation.

4.2 Ionospheric Response to Sector Boundary Crossings

4.2.1 SuperDARN Data Processing

The SuperDARN echoes from the northern and southern radars were classified according to whether they were ionospheric or ground echoes. Sums of total ground and ionospheric echoes recorded by all radars were calculated with a time resolution of one day. Only F–region echoes were included by rejecting echoes that occured in the first 15 range gates. Data from years 2001 to 2011 are included in the study, which is nearly one full solar cycle. The SuperDARN data selection resulted in four time series: a northern hemisphere ground scatter count, a northern hemisphere ionospheric scatter count, a southern hemisphere ground scatter count and a southern hemisphere ionospheric scatter count.

4.2.2 Sector Boundary Crossing Analysis

As seen in Section 4.1, the solar wind speed, the solar wind density and the IMF magnitude changes significantly during a solar sector boundary crossing, as well as over the course of a solar cycle. These solar wind and IMF variations will influence reconnection with the geomagnetic field, and therefore influence convection in the Earth's magnetosphere and ionosphere. Ionospheric measurements from multiple instruments were analyzed to determine if these changes in the solar wind and the IMF have a detectable effect on the Earth's ionosphere. The instruments used were SuperDARN radars, GCR neutron monitors and instruments onboard DMSP satellites. The SuperDARN radars measure ionospheric convection velocity (Section 3.1), the neutron monitors measure GCRs incoming to the Earth from outer space (Section 3.4), and the DMSP satellites measure charged particles that precipitate into the Earth's atmosphere from the magnetosphere (Section 3.3). Since these instruments measure very different aspects of the near–Earth space environment, together they can give a better understanding of the physical mechanisms at work during solar sector boundary crossings.

Epoch analyses were performed on SuperDARN radar measurements, separating the

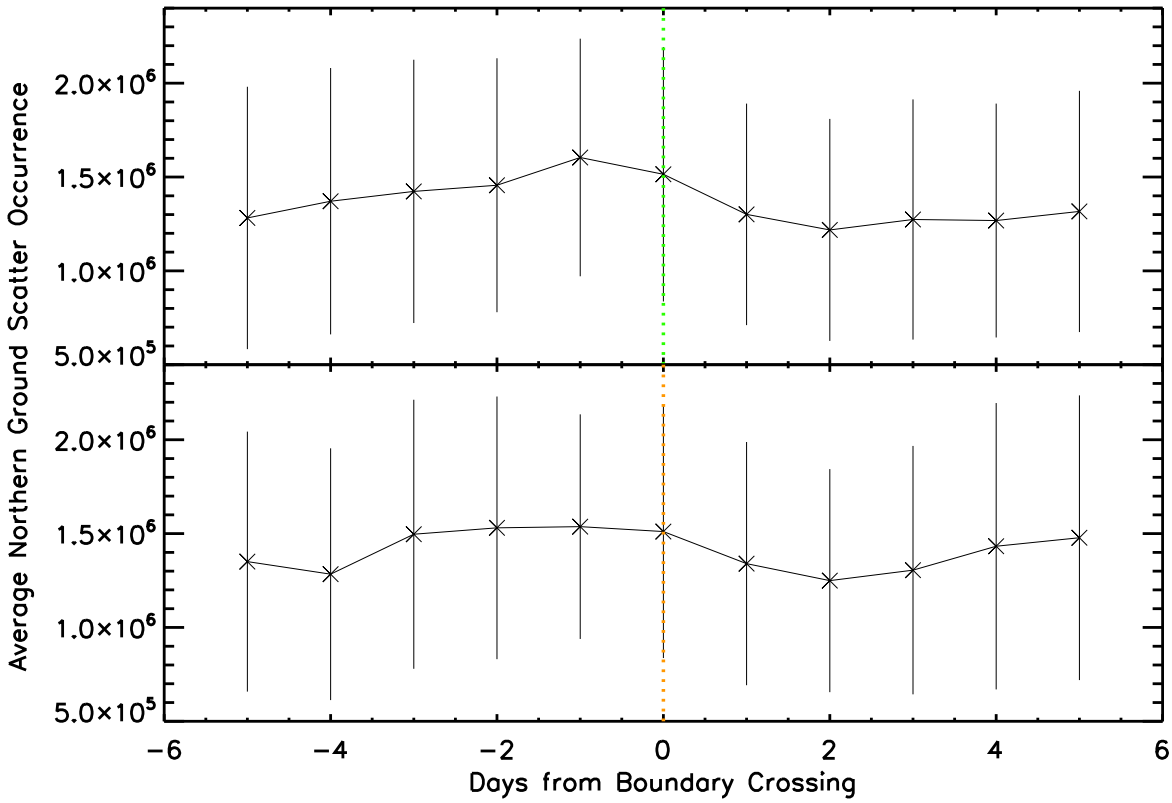

Figure 4.9: Superposed epoch plots of northern hemisphere SuperDARN ground scatter occurrence. The top panel includes 153 toward–to–away events, and the bottom panel includes 138 away–to–toward events. The black vertical lines give the standard deviation.

northern and southern hemispheres, as well as the ionospheric scatter and ground scatter. The superposed epoch plots are presented in Figures 4.9, 4.10, 4.11, and 4.12. The vertical lines on the plots show the standard deviation of the data for that epoch day. The top panel of the figures includes 153 toward–to–away sector boundary crossing events, and the bottom panel in the figures includes 138 away–to–toward sector boundary crossing events.

Figure 4.9 is the superposed epoch plot of the total number of ground scatter measurements made in one day by all of the northern hemisphere SuperDARN radars. Within a day of the solar sector boundary crossing there is a notable peak in the northern hemisphere SuperDARN ground scatter counts. This corresponds to lower solar wind speed and higher solar wind density conditions, as discussed for Figures 4.7 and 4.8. To obtain SuperDARN ground

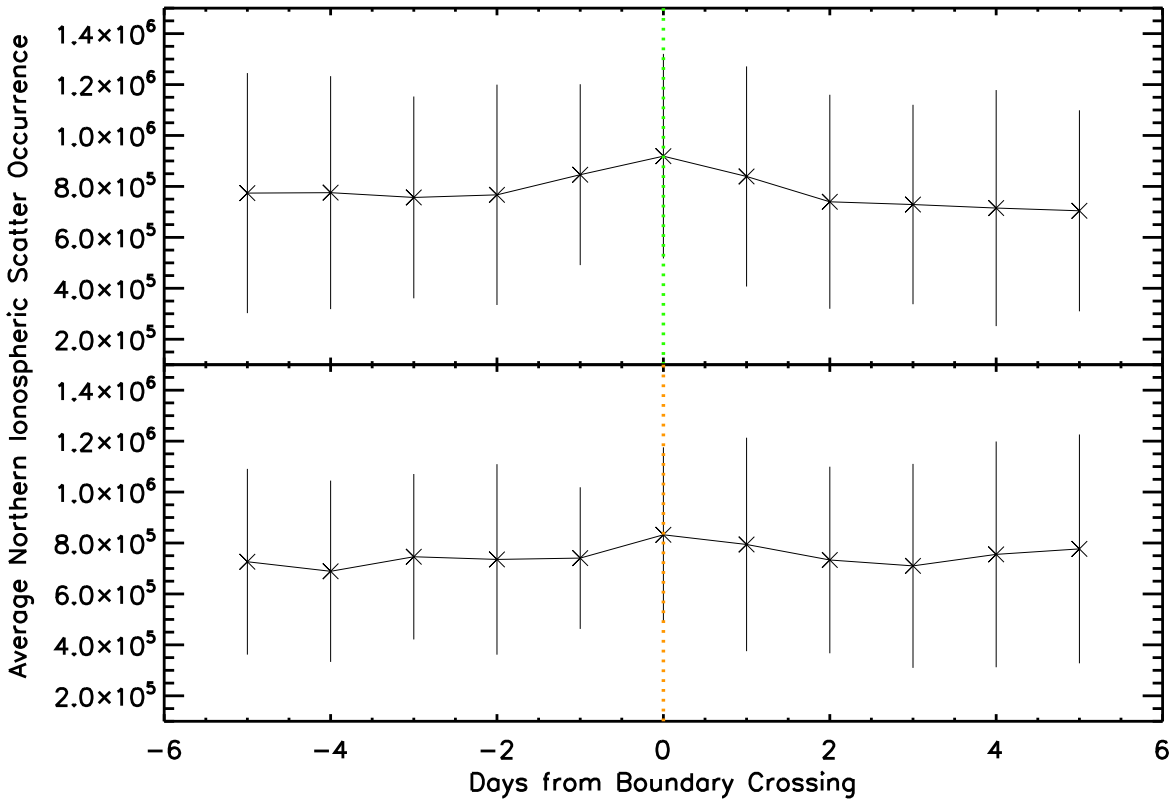

Figure 4.10: Superposed epoch plots of northern hemisphere SuperDARN ionospheric scatter occurrence. The top panel includes 153 toward–to–away events, and the bottom panel includes 138 away–to–toward events. The black vertical lines give the standard deviation.

scatter measurements there must be sufficient plasma density in the ionosphere to refract the radio wave forward to the ground and the scattered wave back to the radar [*Greenwald et al.*, 1995]. The radio waves must also not be absorbed by the ionosphere, which can occur during greatly enhanced electron density events [*Hargreaves*, 1969]. SuperDARN ground scatter measurements are not significantly affected by the existence of plasma irregularities.

Figure 4.10 displays the superposed epoch plot of the daily count of ionospheric echoes from SuperDARN in the northern hemisphere. There is a noticable peak in the SuperDARN counts on the day of a sector boundary crossing. A peak in both the ground scatter and the ionospheric scatter within a day of the sector boundary crossing suggests that changes in radio wave propagation affected the SuperDARN scatter occurrence. Radio wave propagation to

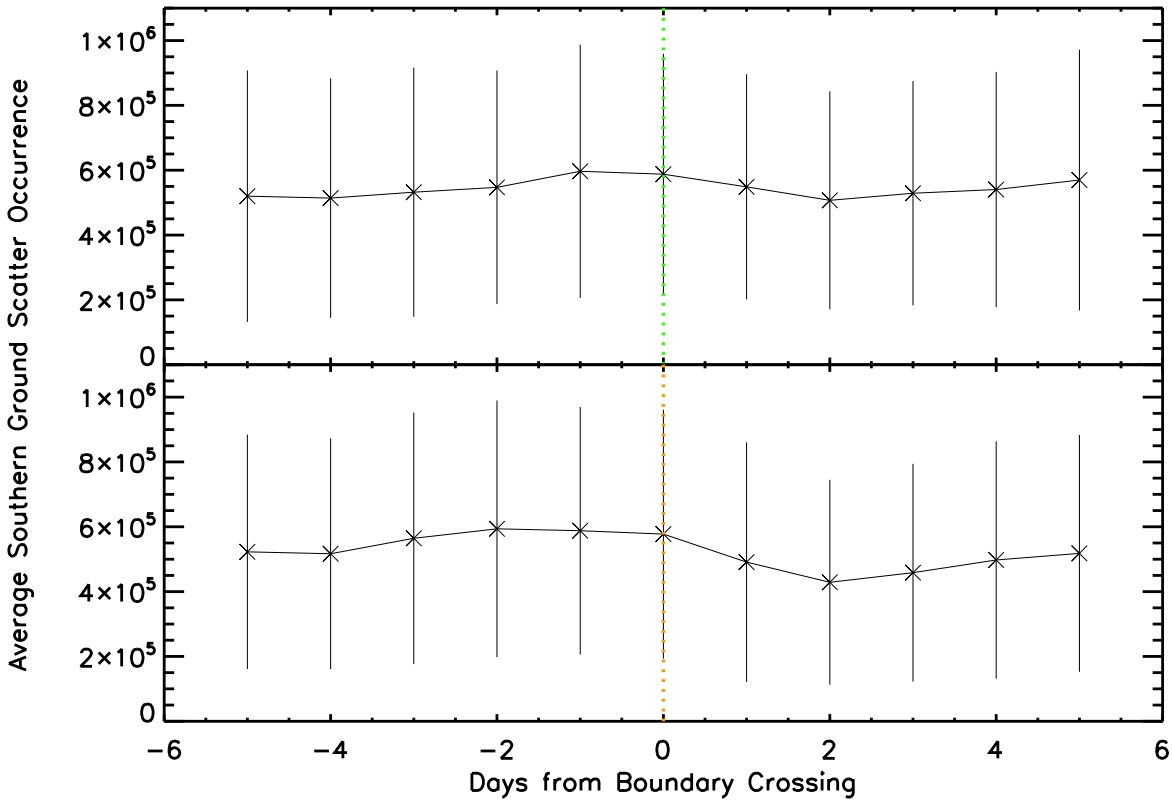

Figure 4.11: Superposed epoch plots of southern hemisphere SuperDARN ground scatter occurrence. The top panel includes 153 toward–to–away events, and the bottom panel includes 138 away–to–toward events. The black vertical lines give the standard deviation.

the ionosphere and the ground is affected by the structure of the ionospheric plasma density. This does not preclude ionospheric irregularities from being affected by conditions in the solar wind, but the irregularities are expected to only affect the ionospheric scatter occurrence.

The southern hemisphere SuperDARN echoes were also examined using a superposed epoch analysis, the results from which are presented in Figures 4.11 and 4.12. While the coverage of SuperDARN in the southern hemisphere is not as extensive as in the northern hemisphere (coverages shown in Figure 3.1), and therefore there are less possible measurements, it is sufficient coverage to investigate if the changes in SuperDARN scatter occurrence are hemisphere dependant. This could give insight into the physical mechanism(s) causing the changes in the SuperDARN scatter occurrence.

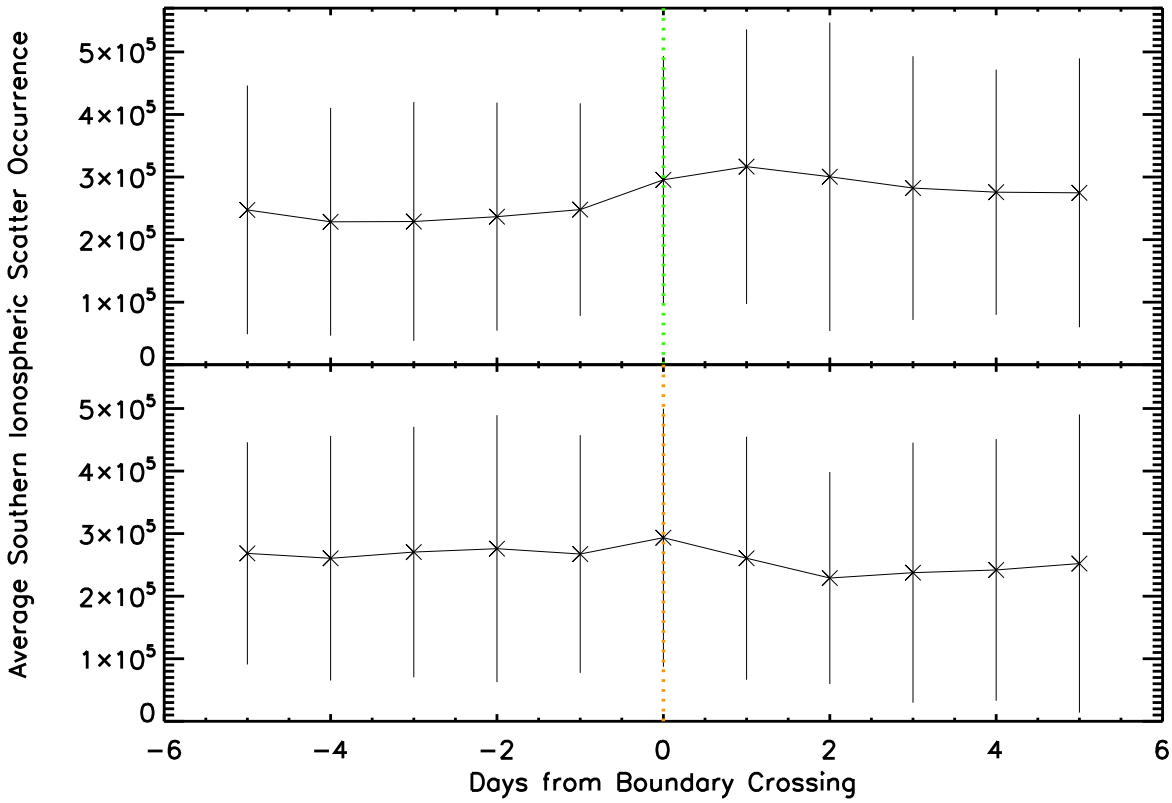

Figure 4.12: Superposed epoch plots of southern hemisphere SuperDARN ionospheric scatter occurrence. The top panel includes 153 toward–to–away events, and the bottom panel includes 138 away–to–toward events. The black vertical lines give the standard deviation.

Figure 4.11 is a superposed epoch plot of the daily counts of ground scatter echoes from SuperDARN radars in the southern hemisphere. There is a decrease in the southern hemisphere ground scatter echoes in the two days following a sector boundary crossing. This trend is similar in the northern hemisphere, albeit smaller. There appears to be no hemispherical dependence on SuperDARN ground scatter occurrence during solar sector boundary crossings.

A superposed epoch analysis was done on the SuperDARN ionospheric scatter occurrence in the southern hemisphere, and results are presented in Figure 4.12. In the toward–to–away solar sector transition plot (top panel), it can be seen there is a peak in the number of ionospheric echoes recorded in the day following the sector boundary crossing. The opposite

was seen in the northern hemisphere SuperDARN echoes for both ionospheric and ground scatter (Figures 4.9 and 4.10), as well as opposite of that seen in the southern hemisphere ground scatter counts. The scatter occurrence does decrease following an away–to–toward sector boundary crossing with a peak on the day of the crossing (bottom panel of Figure 4.12).

Data from the DMSP satellites were used to investigate particles precipitating into the Earth's ionosphere. A superposed epoch analysis was performed on the hemispherical power, which is a quantity derived from the DMSP satellite measurements, and is described in Section 3.3.1.. The hemispherical power is an estimation of the energy deposited through electron precipitation into the area poleward of the equatorward auroral boundary. The superposed epoch analysis of the hemispherical power resulted in the plots shown in Figures 4.13 and 4.14. The top panels in the figures include the toward–to–away sector boundary transition events, and the bottom panels in the figures include the away–to–toward events. The red line is the mean value with one–hour resolution, and the vertical lines are the standard deviation of the superposed data for one epoch hour.

Figure 4.13 is a superposed epoch plot of the northern hemispherical power, with the zero epoch time being the solar sector boundary crossing. The standard deviations are large in the plots, but there is a trend that can be seen. There is, on average, a decrease in the hemispherical power leading up to the sector boundary crossing and an increase in the hemispherical power at or following a sector boundary crossing. This does not appear to be dependent on the polarity of the sector boundary crossing (away–to–toward, or toward–to–away). The hemispherical power is an estimate of the energy being deposited into the auroral zone and poleward of it and is therefore affected by both the number and energy flux of the electrons precipitating. An increase in the hemispherical power corresponds to an increase in the energy flux of the precipitating electrons. This hemispherical power value includes both the auroral zone electron precipitation, originating from the magnetosphere, and the polar cap electron precipitation, originating from "open" field lines connected to interplanetary space.

The superposed epoch plot of the southern hemispherical power in Figure 4.14 reveals a similar trend to that found in the northern hemisphere (Figure 4.13). There is a decrease in the hemispherical power leading up to the sector boundary crossing and an increase in

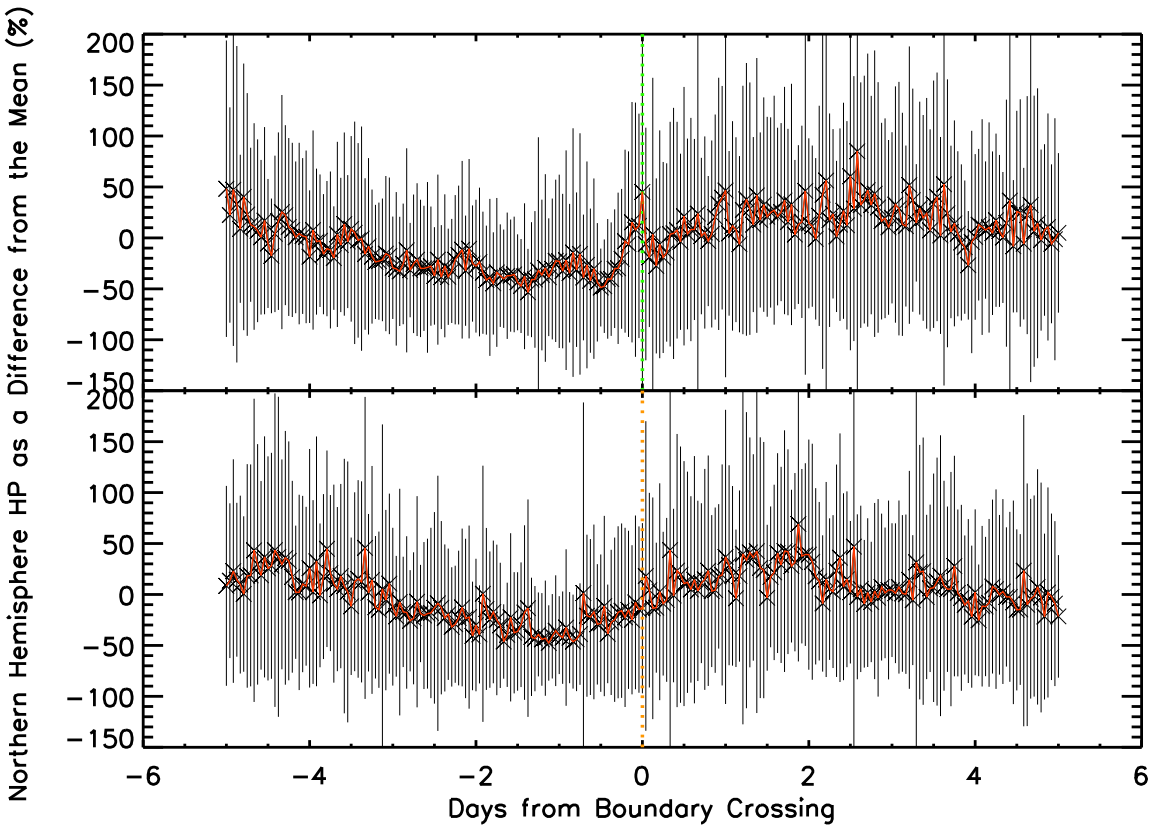

Figure 4.13: Superposed epoch plots of northern hemisphere DMSP hemispherical power. The top panel includes 153 toward–to–away events, and the bottom panel includes 138 away–to–toward events. The red line gives the mean of the data, while the black vertical lines give the standard deviation.

the hemispherical power at or after the sector boundary crossing. The magnitudes of change are similar to those of the northern hemispherical power (Figure 4.13). The variation of hemispherical power appears to be independent of the polarity of sector boundary crossing and of the hemisphere. Therefore it is the crossing of the heliospheric current sheet itself that is related to this change in precipitating electrons, rather than the polarity of the crossing.

From the DMSP satellite measurements, it is also possible to derive the approximate location of the auroral oval in the midnight sector. The "midnight boundary index" (MBI) value is the approximate latitude of the equatorward boundary of the auroral oval at midnight local time, as described in Section 3.3.1. Figures 4.15 and 4.16 are hourly superposed epoch plots of the midnight boundary index (MBI). The vertical lines in the plots are the standard

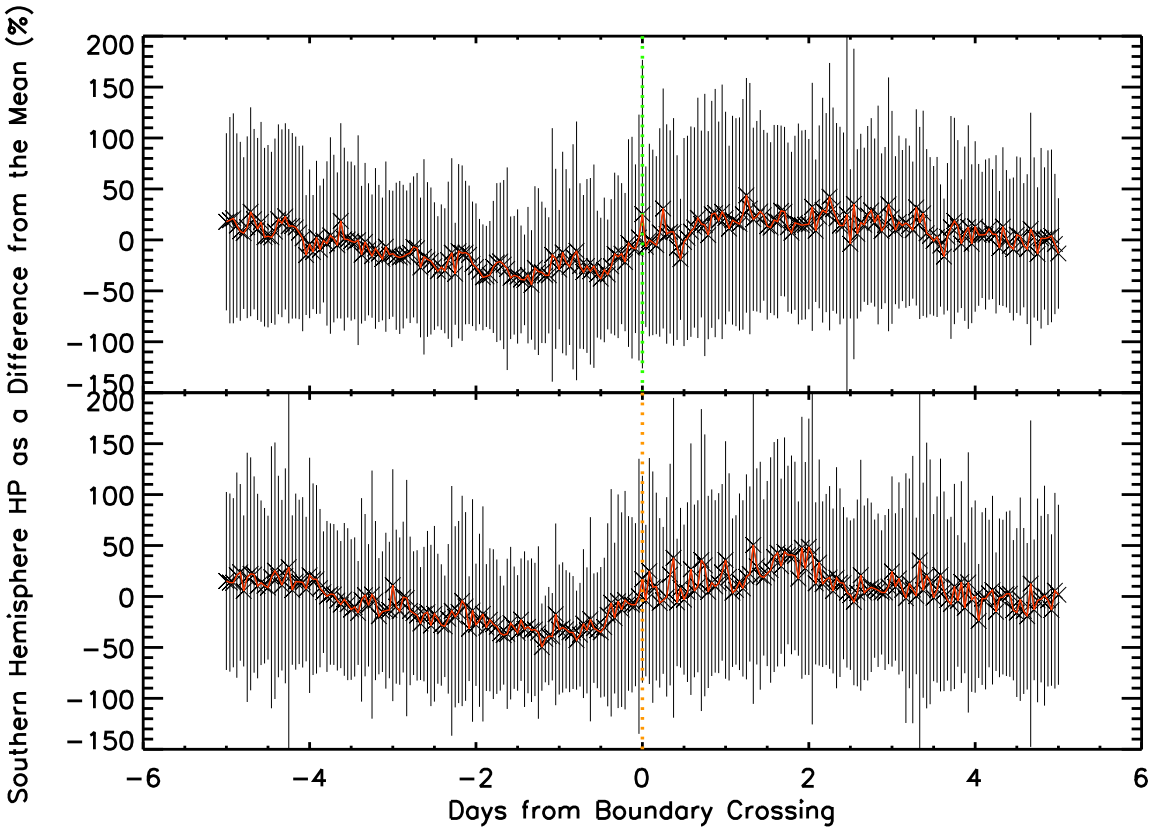

Figure 4.14: Superposed epoch plots of southern hemisphere DMSP hemispherical power. The top panel includes 153 toward–to–away events, and the bottom panel includes 138 away–to–toward events. The red line gives the mean of the data, while the black vertical lines give the standard deviation.

deviation for that epoch hour while the red line is the mean MBI for that epoch hour. The zero epoch hour is when the Earth crosses the solar sector boundary. The top panel includes the sector boundary transition events with toward–to–away polarity, and the bottom panel includes the sector boundary transition events with away–to toward polarity. Both panels in Figure 4.15 show a decrease in the MBI latitude in the days after a sector boundary crossing. This means that the equatorward auroral boundary expands towards the equator after a sector boundary crossing, but does not give us information on what is happening with regards to the poleward auroral boundary. The MBI does not reveal if the whole oval is expanding and maintaining its shape, or if just the midnight auroral oval is broadening in latitude. Case studies could shed light as to whether there are changes to the poleward

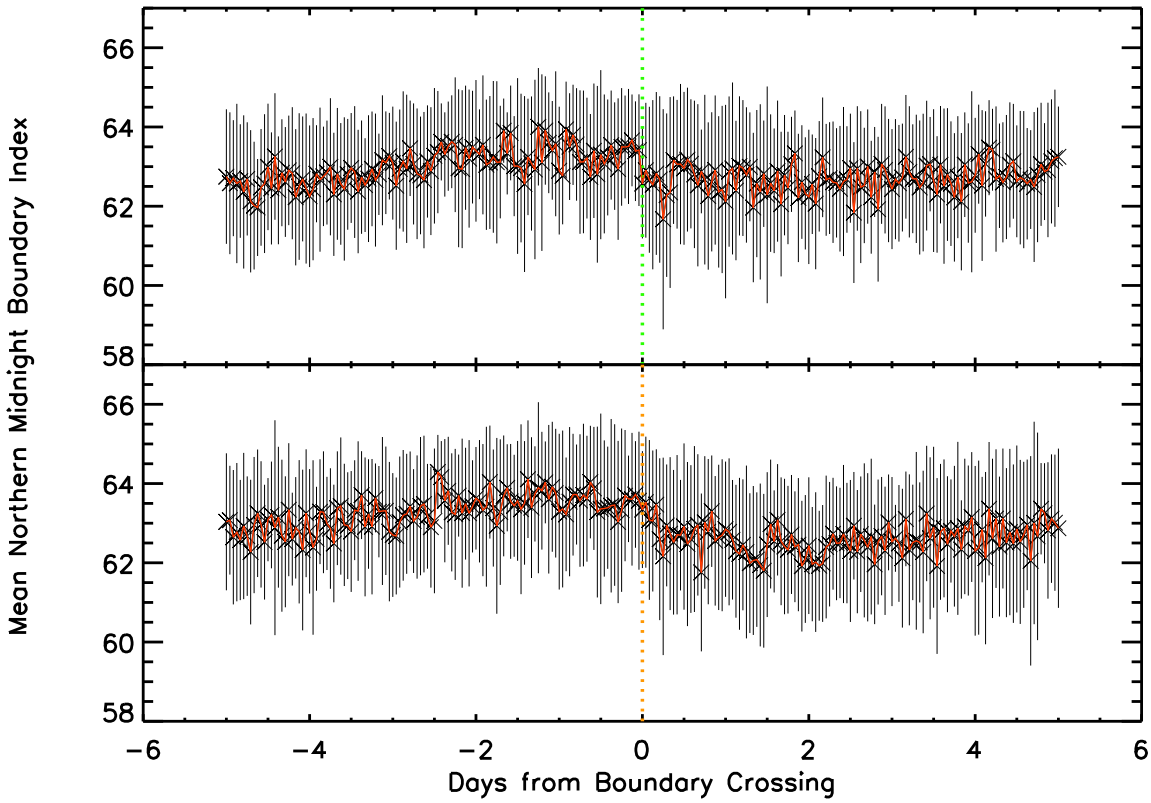

Figure 4.15: Superposed epoch plots of northern hemisphere DMSP midnight boundary index. The top panel includes 153 toward–to–away events, and the bottom panel includes 138 away–to–toward events. The red line gives the mean of the data, while the black vertical lines give the standard deviation.

auroral boundary, but this will be left for future work. As both panels display a decrease in MBI latitude following a solar sector boundary crossing, there does not appear to be any dependence of the MBI latitude on the polarity of the sector boundary crossing. From the hemispherical power results we know there is more energy being deposited in the hemispheres after a sector boundary crossing, which has been shown to be correlated with an expansion of the auroral oval [*Boudouridis et al.*, 2003].

Figure 4.16 are the hourly superposed epoch plots of the DMSP MBI in the southern hemisphere. The MBI latitude decreases after the sector boundary crossing for both the transition polarities. This is the same trend that was seen in the northern MBI, so the change in the auroral oval latitude does not appear to be dependant on either the polarity

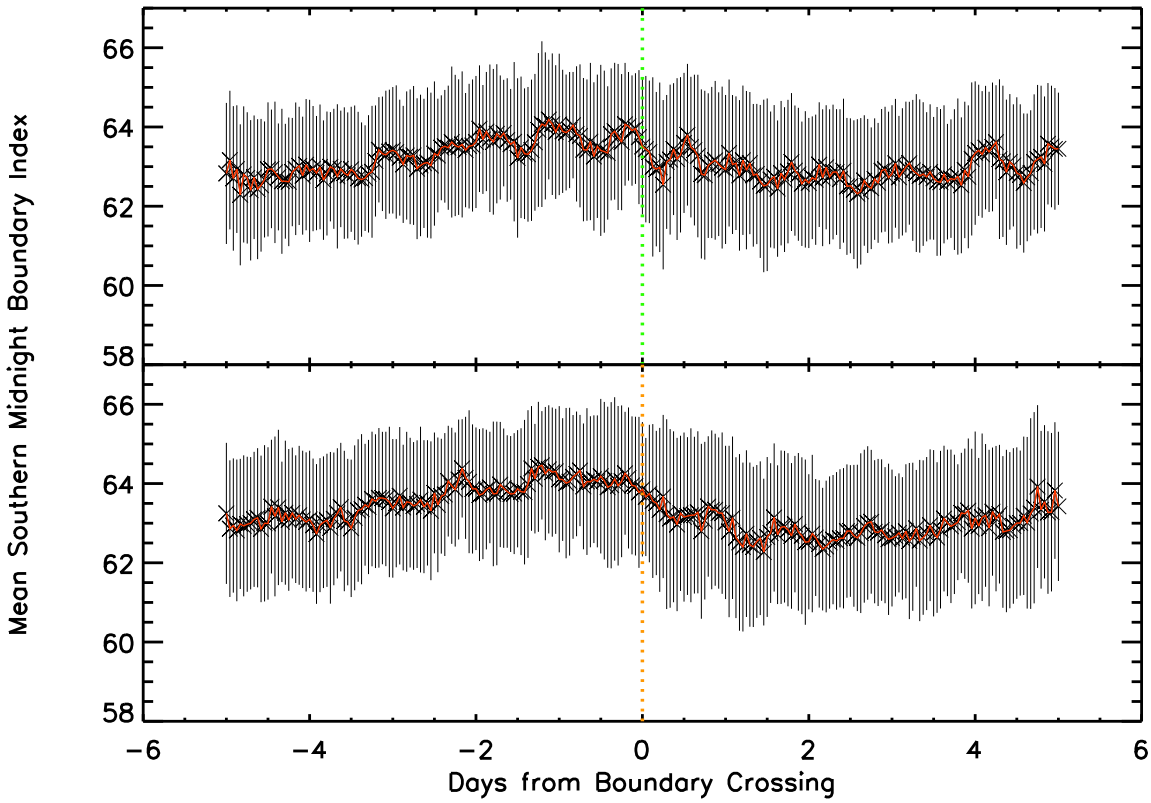

Figure 4.16: Superposed epoch plots of southern hemisphere DMSP midnight boundary index. The top panel includes 153 toward–to–away events, and the bottom panel includes 138 away–to–toward events. The red line gives the mean of the data, while the black vertical lines give the standard deviation.

of the sector boundary crossing or on the hemisphere during sector boundary crossings.

Since there is a change in the magnitude of the IMF during sector boundary crossings (Section 4.1), there may be an effect on the galactic cosmic rays (GCRs) measurements at Earth's surface [*Cane et al.*, 1999]. The Bartol Research Institute has a multitude of GCR monitors located around the globe, and their operation was described in Section 3.4. A superposed epoch analysis was performed on the GCR monitor measurements, and is shown in Figures 4.17 and 4.18. The time resolution of the superposed GCR data is one hour, and 120 hours of data on either side of the sector boundary crossing are shown. The vertical lines are the standard deviation of the hourly superposed data, and the red line is the mean. Plotted are the uncorrected neutron counts from the detectors, which means no

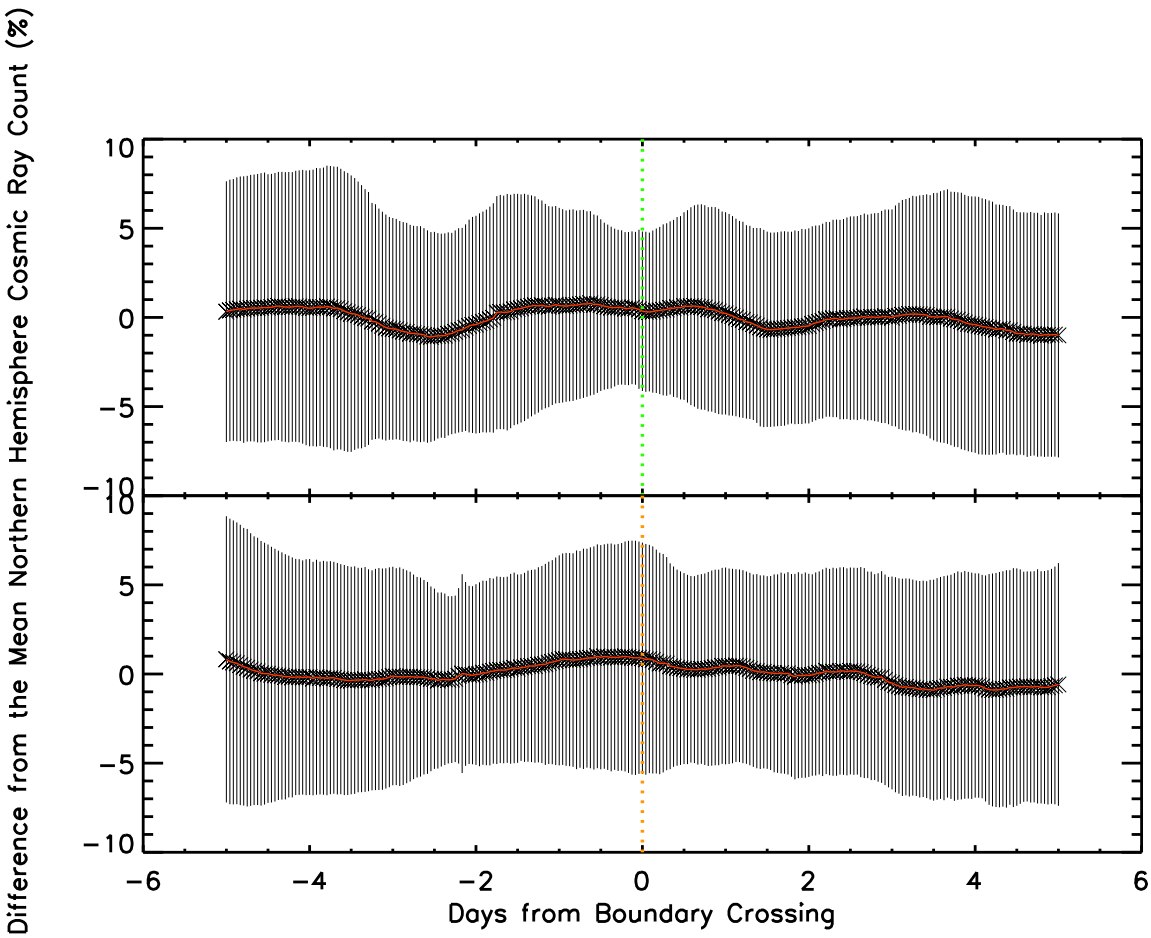

Figure 4.17: Superposed epoch plots of northern hemisphere uncorrected cosmic ray monitor counts. The top panel includes 153 toward–to–away events, and the bottom panel includes 138 away–to–toward events. The red line gives the mean of the data, while the black vertical lines give the standard deviation.

atmospheric correction has been performed. A superposed epoch analysis on the corrected counts was also performed, but the results were similar. The top panel includes sector boundary transition events with toward–to–away polarity, and the bottom panel includes sector boundary transition events with away–to–toward polarity.

Figure 4.17 presents data from the northern hemisphere, specifically from the Bartol Research Institute's neutron monitor station at Thule, Greenland. From the plots, it can be seen that there is no significant change in the GCR counts related to the crossing of a sector boundary. At most the counts vary by 1%, which is neglible when considering the standard deviation of the data.

Figure 4.18 presents the southern hemisphere data from Bartol Research Institute's neu-

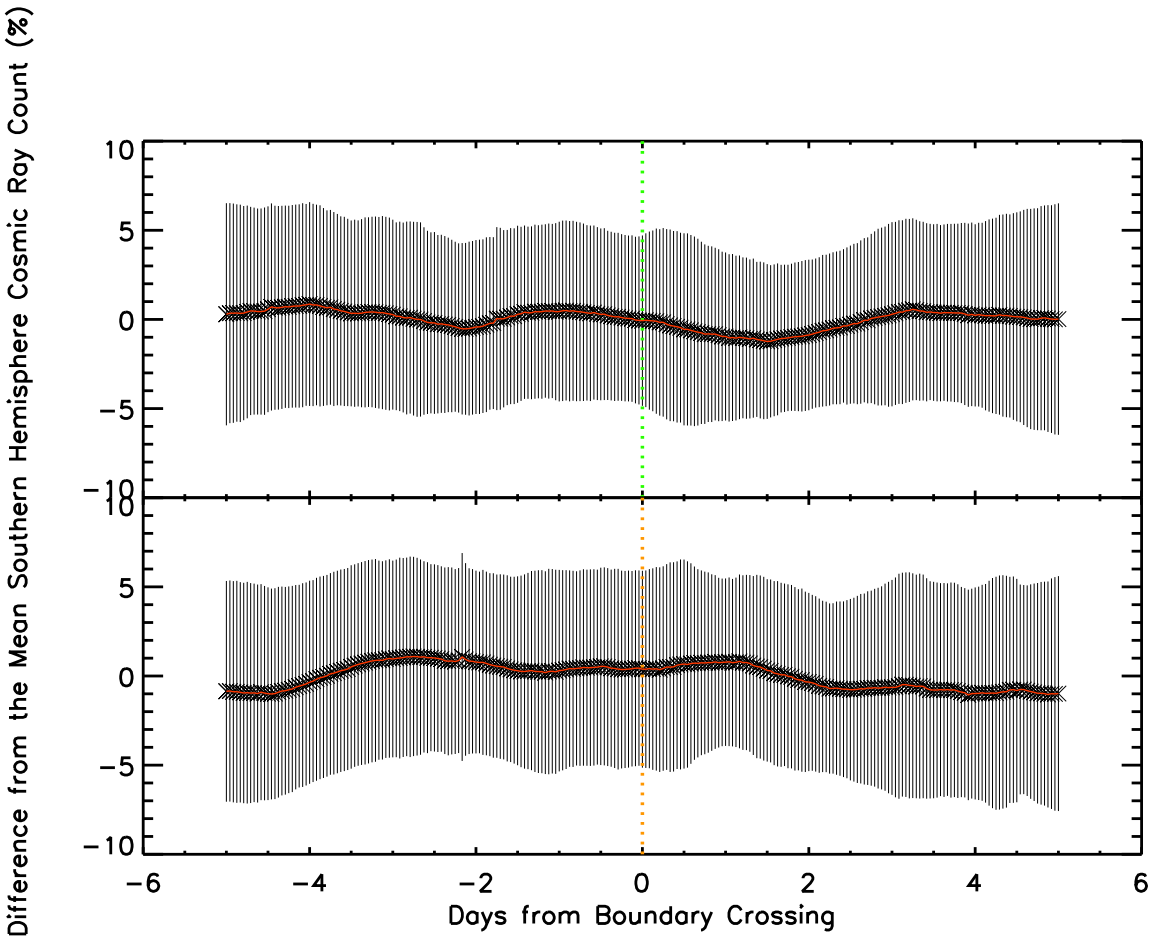

Figure 4.18: Superposed epoch plots of southern hemisphere uncorrected cosmic ray monitor counts. The top panel includes 153 toward–to–away events, and the bottom panel includes 138 away–to–toward events. The red line gives the mean of the data, while the black vertical lines give the standard deviation.

tron monitor at McMurdo, Antarctica. The variation from the mean is less than 1% for the GCR counts, and no significant trend is evident. From these results it appears there is little to no dependence of the cosmic ray count on sector boundary crossings. It may be useful to examine GCR data from interplanetary spacecraft instruments, as these do not include Earth–based sources of neutrons that could mask a weak signal. As we are concerned more with the ionosphere than the troposphere in this study, this analysis is beyond the scope of the present work and will be left for future investigation.

4.3 Ionospheric Persistent Responses to IMF and Solar Wind Conditions

4.3.1 Time Series Analysis

To complement the statistical results from the superposed epoch analyses, the time series of some of the data sets were investigated. These include the solar sector angle, the SuperDARN ground scatter measurement occurrence, the DMSP hemispherical power and the solar wind speed. A sample of the time series is presented in Figure 4.19. In Figure 4.19 the verticle dashed lines represent the sector boundary crossings determined using the method described in Section 4.1. The orange lines mark a transition from an away to a toward sector, and the green lines mark a transition from a toward to an away sector. The top panel contains the solar wind speed, the middle panel contains the northern hemisphere SuperDARN ground scatter occurrence and the bottom panel contains the DMSP northern hemispherical power.

In the away sectors (following the green dashed lines) there is consistently a strong solar wind speed compared to that recorded during the toward sectors (following the orange dashed lines). During the periods of high solar wind speed the SuperDARN ground scatter occurrence appears to be lower. The year 2003 was during the decline of solar cycle 23 and the solar sector had a well defined 27–day, 2–sector structure during this period (e.g., see Figure 4.4). The regular solar sector structure is evident from the regular spacing between the sector boundaries in Figure 4.19.

A visual inspection of the data revealed many oscillations of the parameters with possible correlations and anticorrelations between several of the data sets. A more systematic approach is therefore warranted to investigate these in detail.

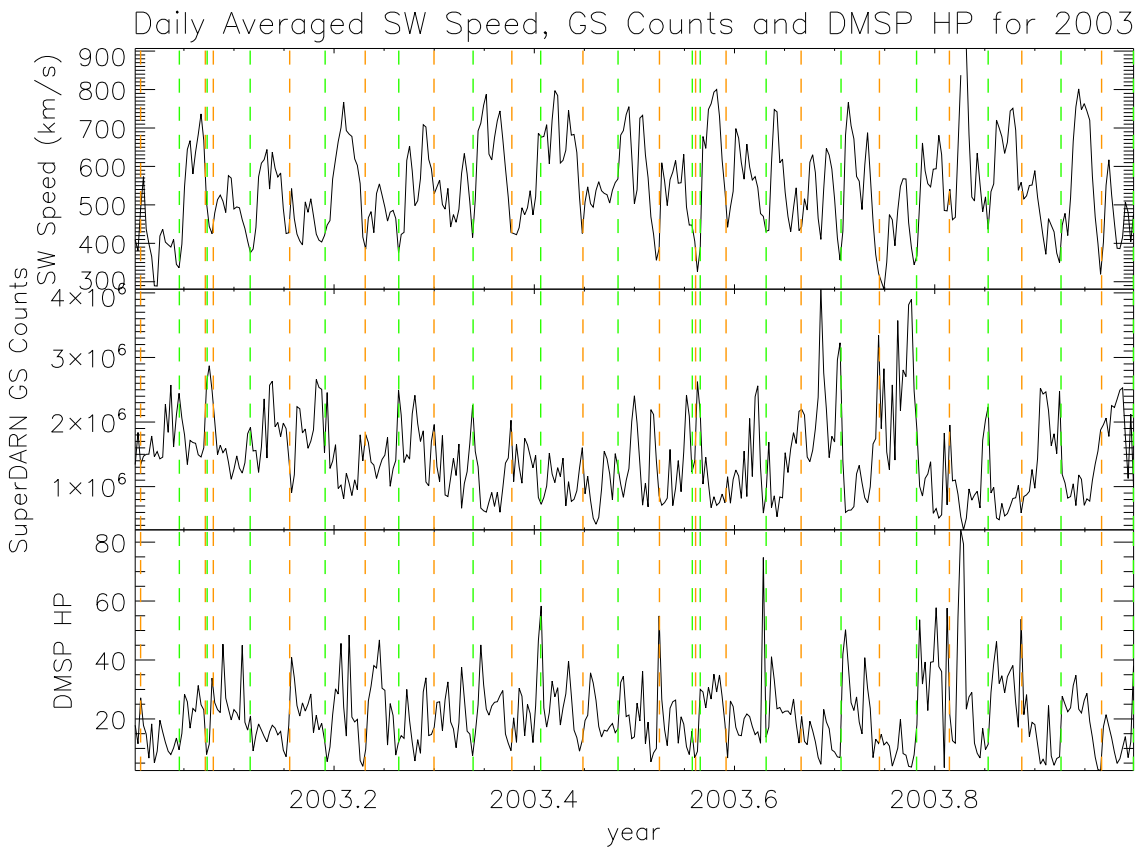

Figure 4.19: Time series of the averaged solar wind speed (top panel), the northern hemisphere SuperDARN ground scatter measurement occurrence (middle panel) and the averaged northern hemisphere DMSP hemispherical power (bottom panel) for the year 2003. The vertical dashed lines show the polarity and time of the solar sector boundary crossings that occurred. The orange lines represent the away–to–toward sector boundary transition, and the green lines represent the toward–to–away sector boundary transition.

4.3.2 Fast Fourier Transform Analysis

A fast fourier transform (FFT) analysis was performed on the solar wind and ionospheric data, and the results are presented in Figures 4.20 through 4.25. This analysis helps to determine the dominant frequencies in the time series. These plots all have the same format, with the maximum value of 0.2 cycles per day corresponding to a minimum periodicity of 5 days. The vertical axis of the plots is the year and has a resolution of ten days. The horizontal axis is the frequency of the data in cycles per day. The color scale represents the intensity of the fourier spectrum in arbitrary units. The FFT is performed on a boxcar sliding window of 361 days, so there will be some artifacts in the power spectrum at very high and very low frequencies. There will also be some "smearing" of the data in the time domain (vertically) because the vertical resolution of the plot is 10 days, but a 361 day window is used to perform the FFT analysis. The result is that every ten days there are only ten new days used in the FFT analysis, while there are 351 days that were used in the previous FFT horizontal strip. This method, while it does "smear", does provide a useful view of how the dominant frequencies change from year to year over the course of a solar cycle. The vertical lines on the plots show the 27–day, 13.5–day, 9–day and 6.75–day periodicities, from left to right, respectively.

One thing to note about spectral analyses is that spurious harmonics of dominant frequencies can appear in the spectrum of the data. If there is a dominant 27–day periodicity in the data, there can be a 13.5–day periodicity seen in the spectral analysis, even though there are no 13.5–day periodic variations in the data. These additional spectral peaks are often due to the shape of the waveforms in the data set. A preliminary analysis was performed on the solar wind speed to determine if the spectral peaks were due to periodicities present int he original data set or if they were artifacts introduced by the spectral analysis. The spectral peaks in the spectral analysis of the solar wind speed appear to be present in the data set. This is very promising and warrants a more thorough investigation in the future.

Figure 4.20 is the FFT spectrum of the solar sector angle. There are strong 27–day and 13.5–day periodicities in the data set. The 27–day periodicity is dominant in every year except for 2005 and 2006, while there is a strong 13.5–day periodicity in the years

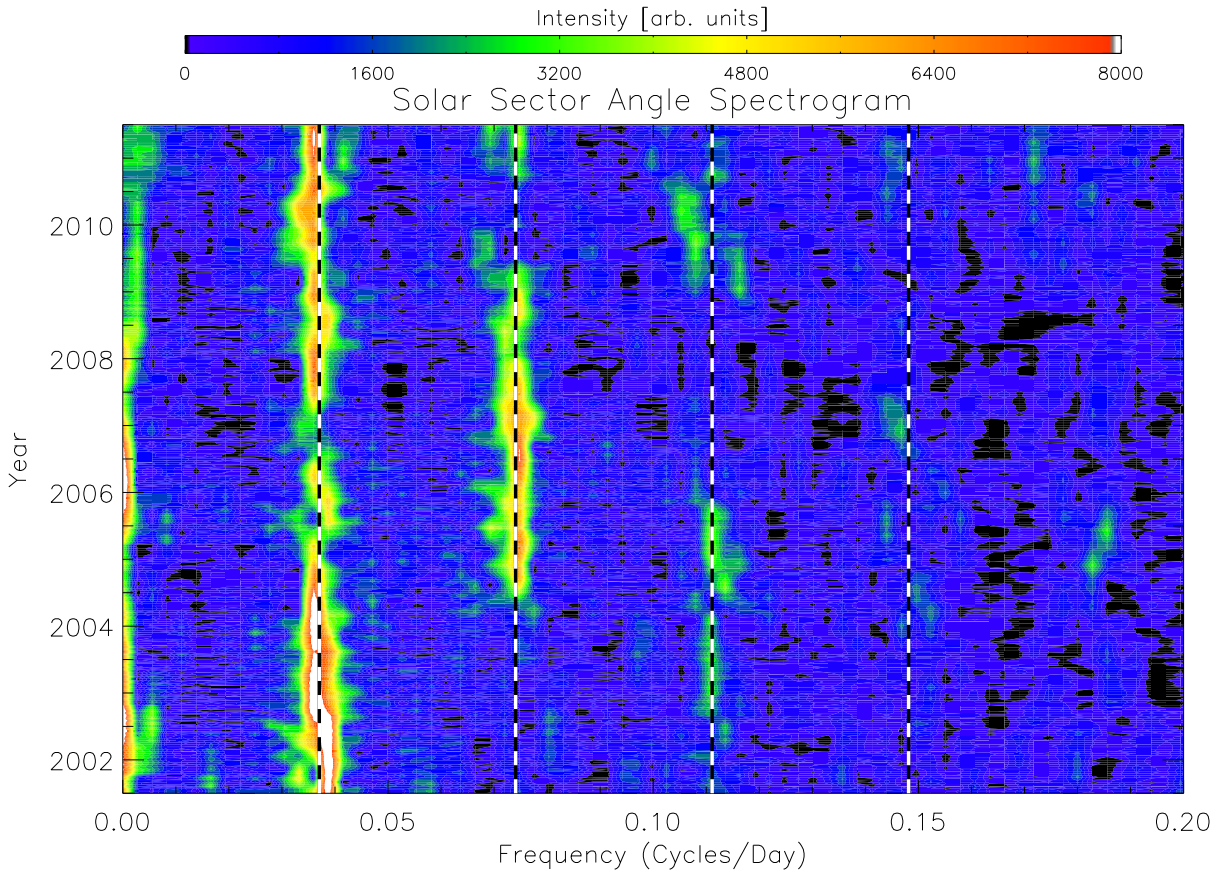

Figure 4.20: Spectrogram of the solar sector angle. The vertical axis has a resolution of ten days, and the FFT is done as a 361–day sliding window. The vertical lines show periodicities of 27–days, 13.5–days, 9–days and 6.75–days. The intensity of the fourier spectrum has arbitrary units.

2005 through 2008. A 27–day periodicity in the sector angle corresponds to a two–sector solar sector structure, and a 13.5–day periodicity corresponds to a four–sector solar sector structure. In Sections 4.1 and 4.2.2 it was shown that many solar wind and ionospheric properties vary across solar sector boundaries. Some of the parameters vary independently of the sector boundary crossing polarity (away–to–toward or toward–to–away). The dominant frequencies for these data are therefore expected to be twice that of the dominant sector angle frequencies.

The FFT spectrum of the solar wind speed is shown in Figure 4.21. There are dominant frequencies with periodicities of 27–days, 13.5–days, 9–days and 6.75–days. The strong 27–day periodicity is likely due to the synodic solar rotation (described in Section 2.1.3), where

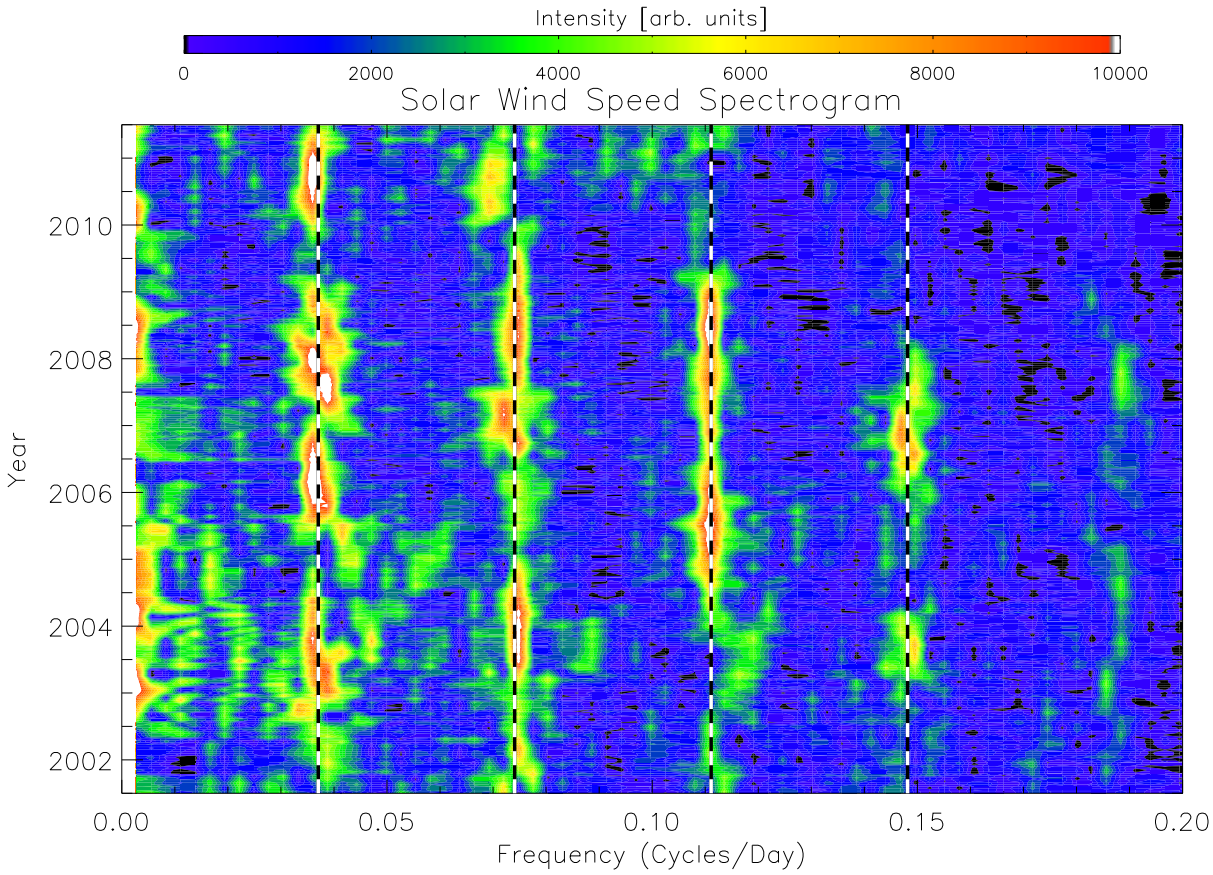

Figure 4.21: Spectrogram of the solar wind speed. The vertical axis has a resolution of ten days, and the FFT is done as a 361–day sliding window. The vertical lines show periodicities of 27–days, 13.5–days, 9–days and 6.75–days. The intensity of the fourier spectrum has arbitrary units.

structures on the Sun "re-appear" every 27–days. If a fast solar wind stream is seen at Earth, it is likely that 27 days later the fast solar wind stream will re–appear. During the crossing of a sector boundary, there is a significant change in the solar wind speed (Figure 4.7). The analysis in Section 4.1 showed that there is little, if any, dependence of the solar wind speed on the polarity of the sector boundary crossing within several days of the crossing, and therefore the solar wind speed should have a strong power in the FFT with a frequency that is twice that of the solar sector angle. Comparing Figures 4.20 and 4.21, this effect can be seen in 2006 when there was a strong 13.5–day periodicity in the sector angle and a corresponding strong 6.75–day periodicity in the solar wind speed centered on 2006. The strong 13.5–day periodicity peak in the solar wind speed corresponds to the strong 27–day

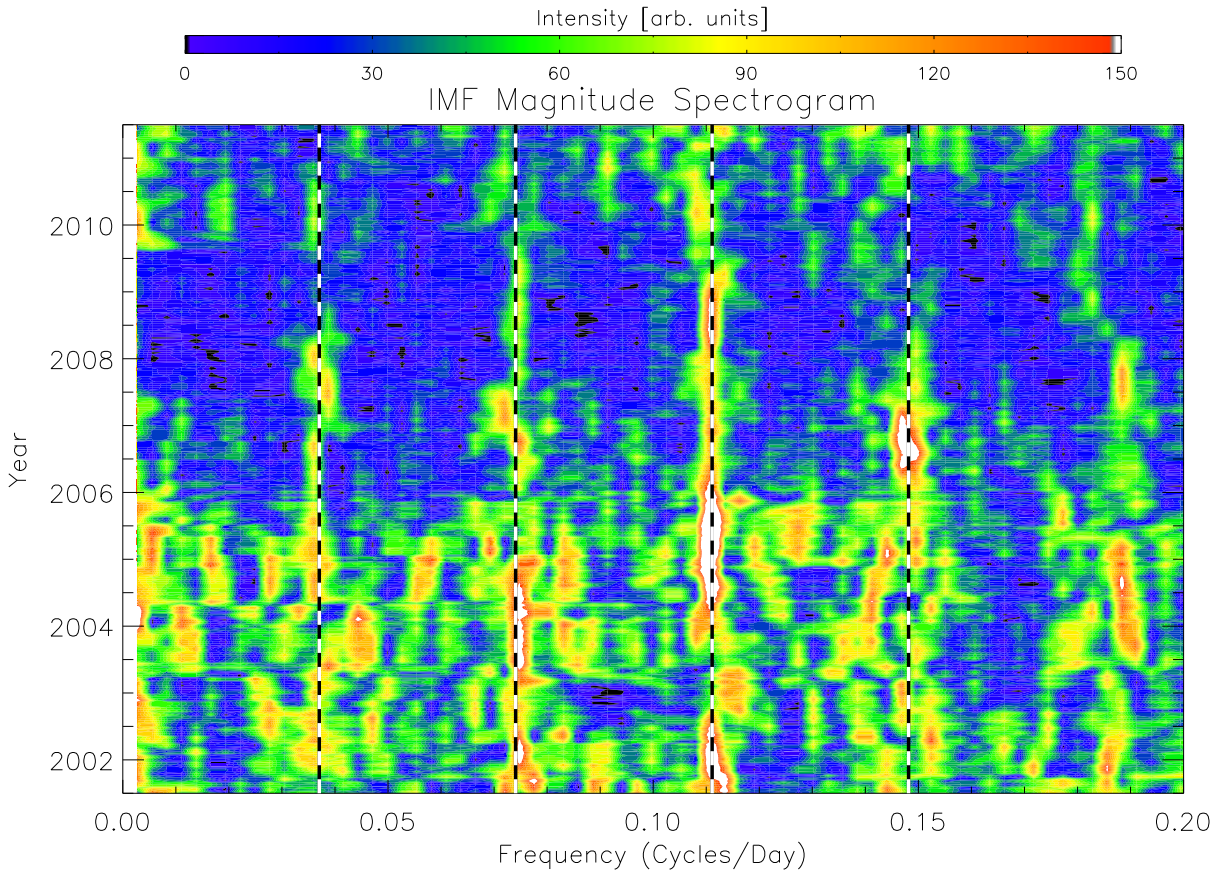

Figure 4.22: Spectrogram of the IMF magnitude. The vertical axis has a resolution of ten days, and the FFT is done as a 361–day sliding window. The vertical lines show periodicities of 27–days, 13.5–days, 9–days and 6.75–days. The intensity of the fourier spectrum has arbitrary units.

periodicity peak in the solar sector angle. There is a strong 9–day periodicity in the solar wind speed in the years 2005–2008 that has been shown to be due to recurring high–speed streams [*Emery et al.*, 2011]. High speed streams tend to emerge from coronal holes that persist for more than one solar rotation period, and from 2005–2008 there were three coronal holes spaced evenly around the Sun.

The fourier spectrum of the IMF magnitude is shown in Figure 4.22. During the maximum and the decline of solar cycle 23 (2001.5–2005) there were a multitude of strong peaks in the fourier spectrum. The spectral components have periodicities of 13.5 days and 9 days. In 2006 there is a strong spectral peak with a periodicity of 6.75 days. In 2006 there was also a strong 13.5–day periodicity in the sector angle (Figure 4.20). Recall from Figure 4.6 that

during a sector boundary crossing there is a significant increase in the IMF magnitude, which is independent of the crossing polarity. This could account for the strong periodicity at 6.75 days in Figure 4.22, which is half the periodicity of the solar sector angle (Figure 4.20). Similarly the 13.5–day periodicities in the IMF magnitude could be due to the dominant 27–day periodicities in the solar sector angle that persists for much of the solar cycle. The 9–day periodicity in the IMF magnitude is interesting, as, while there was high speed streams from 2005–2008 creating a strong 9–day periodicity in the solar wind [*Emery et al.*, 2011], there is a dominant 9–day periodicity peak across more years in the IMF magnitude spectrogram. There is also a periodicity in the IMF magnitude spectrum of approximately 5.4 days in 2002, 2004 and 2007. The 27–day periodicity in the IMF magnitude, noticeable from 2002–2008, is likely due to the solar synodic rotation and recurring magnetic structures from the Sun. It's also worth taking note of the lower intensity of the fourier spectrum of the IMF magnitude during solar minimum. This agrees with the lower variability of the IMF magnitude during this time period (Figure 4.2).

Figure 4.23 is the fourier spectrogram of the northern DMSP hemispherical power. One thing to note is that there is only hemispherical power data up to day 107 in 2011, so the vertical axis is slightly different than the solar wind spectrogram axes. There are peaks at a multitude of frequencies in the hemispherical power spectrogram during the years 2001.5–2004.5. These peaks occur at periodicities of approximately 27 days and 13.5 days. From 2004.5–2008 there is a significant peak at a periodicity of 9 days. Past studies have shown the hemispherical power to be correlated with the solar wind speed [*Brautigam et al.*, 1991]. The fourier spectrogram of the solar wind speed (Figure 4.21) has a similar peak at 9 days from 2005–2008. The periodicity of 6.75 days in the hemispherical power in the year 2006 may also be related to a similar periodicity in the solar wind speed at that time. Comparing Figures 4.7 and 4.13, the northern hemispherical power changes across a sector boundary crossing in a manner that is very similar to the change in the solar wind speed across a sector boundary crossing. The change in both of these parameters appears to be independent of the sector boundary crossing polarity. Like the solar wind speed, the dominant period that would be expected for the hemispherical power would be half the dominant period of the solar sector angle. During 2006 there was a strong 13.5–day periodicity in the solar sector

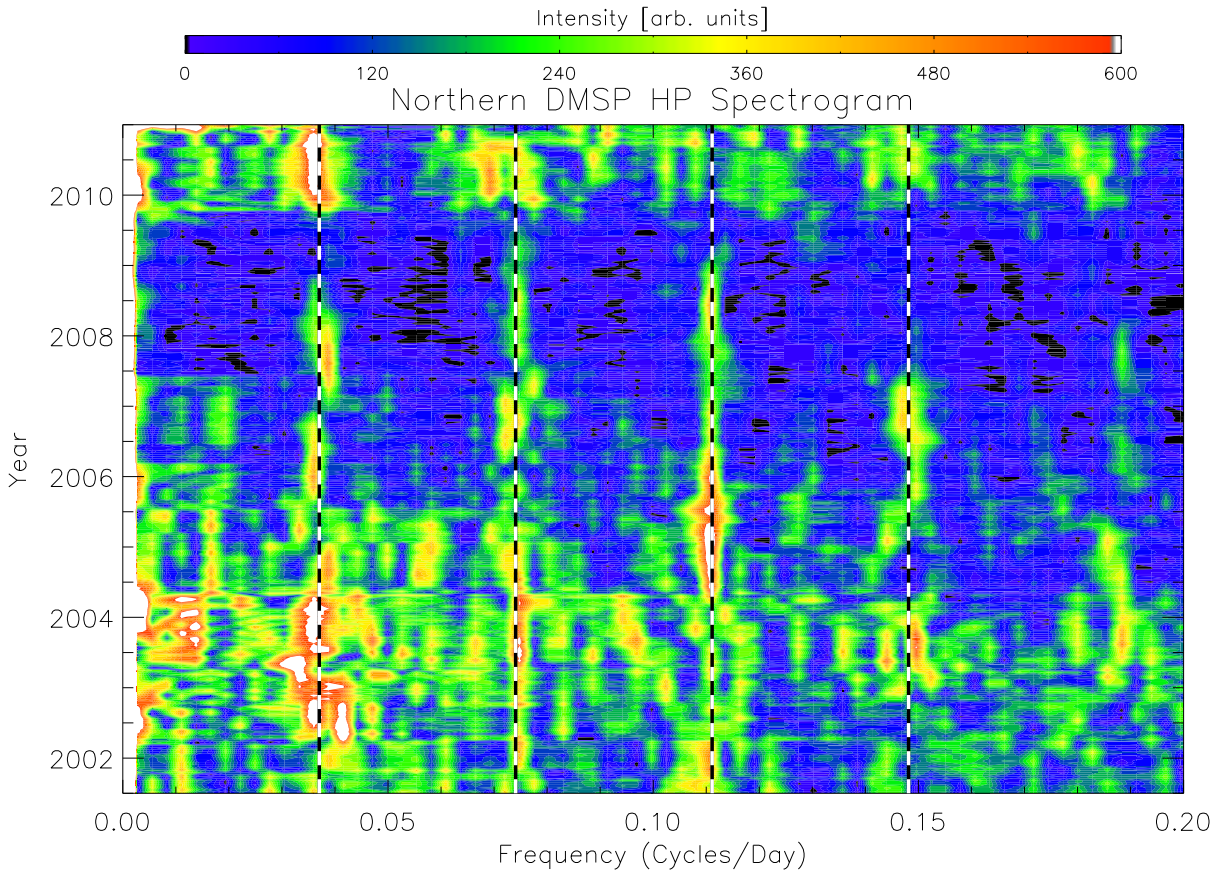

Figure 4.23: Spectrogram of the DMSP northern hemispherical power. The vertical axis has a resolution of ten days, and the FFT is done as a 361–day sliding window. The vertical lines show periodicities of 27–days, 13.5–days, 9–days and 6.75–days. The intensity of the fourier spectrum has arbitrary units.

angle, which corresponds to the strong 6.75–day periodicity in the hemispherical power. The spectrogram of the hemispherical power is very similar to that of the solar wind speed (Figure 4.21), especially during the solar minimum (2006–2009). This is to be expected, since *Brautigam et al.* [1991] showed a strong correlation between solar wind speed and auroral charged particle precipitation.

The fourier spectrogram of the northern hemisphere SuperDARN ground scatter occurrence is shown in Figure 4.24. The vertical axis extends only to the end of 2010. A strong 9–day periodicity can be seen in the data during the years 2005–2008, which is similar to the strong 9–day periodicity seen in the solar wind speed (Figure 4.21) and the DMSP hemispherical power (Figure 4.23). While the 9–day periodicity in the northern hemisphere

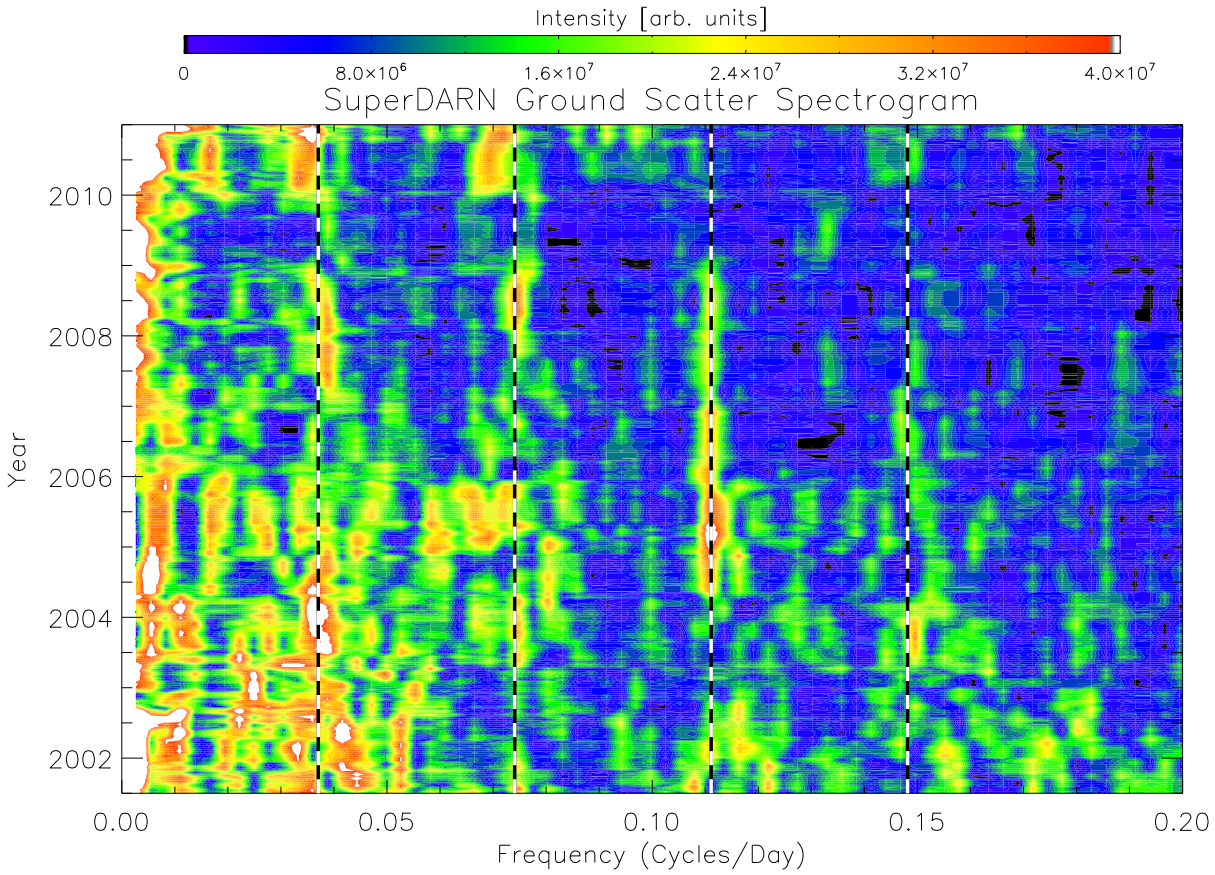

Figure 4.24: Spectrogram of the northern hemisphere SuperDARN ground scatter occurrence. The vertical axis has a resolution of ten days, and the FFT is done as a 361–day sliding window. The vertical lines show periodicities of 27–days, 13.5–days, 9–days and 6.75–days. The intensity of the fourier spectrum has arbitrary units.

SuperDARN ground scatter is quite evident, the periodicities of 27 days and 13.5 days that were dominant in the solar wind speed and the DMSP hemispherical power are much less significant in the SuperDARN ground scatter spectrogram. During the solar maximum and decline of solar cycle 23 (2001.5–2005) there are multiple peaks at low frequencies (high periodicities), the origin and validity of which are not known. The 27–day periodicity is likely due to the solar synodic rotation, while the other longer periodicities could be due to the operating mode of the radars or periodic ionospheric conditions, such as a seasonal variations. During the solar minimum period (2006–2009) many of the low frequency peaks in the FFT analysis are reduced, while the frequencies corresponding to periodicities of 27 days and 13.5 days become dominant during 2008. The data processing routine was modified in

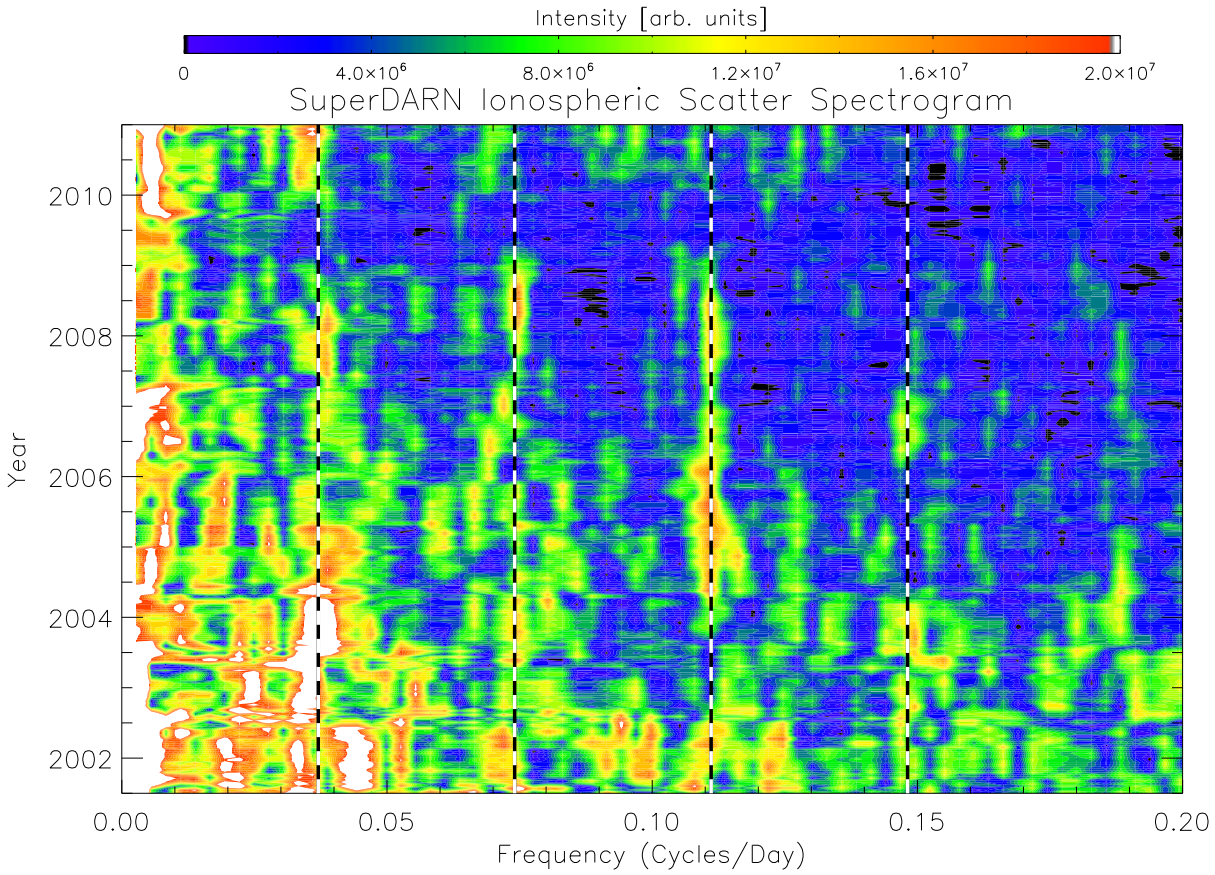

Figure 4.25: Spectrogram of the northern hemisphere SuperDARN ionospheric scatter occurrence. The vertical axis has a resolution of ten days, and the FFT is done as a 361–day sliding window. The vertical lines show periodicities of 27–days, 13.5–days, 9–days and 6.75–days. The intensity of the fourier spectrum has arbitrary units.

2006, which could account for the reduction of the low frequency peaks at this time.

Figure 4.25 shows the spectrogram of the northern hemisphere SuperDARN ionospheric scatter occurrence. The SuperDARN ionospheric scatter and ground scatter occurrence appear to have very similar dominant frequencies. During the solar maximum and decline of solar cycle 23 (2001.5–2005) there are a number of low frequencies that have large peaks in the FFT power spectrum for SuperDARN ionospheric scatter. These low frequency peaks are reduced during the solar minimum (2006–2009). As stated earlier, the data processing routine was modified in 2006, which could account for the systematic reduction of low frequencies after this time. In 2008 there is a significant peak in the SuperDARN ionospheric scatter spectrogram at periodicities of 27–days and 13.5–days. There is also a significant

peak at a 9–day periodicity in the SuperDARN ionospheric scatter spectrogram during the years 2005–2008.

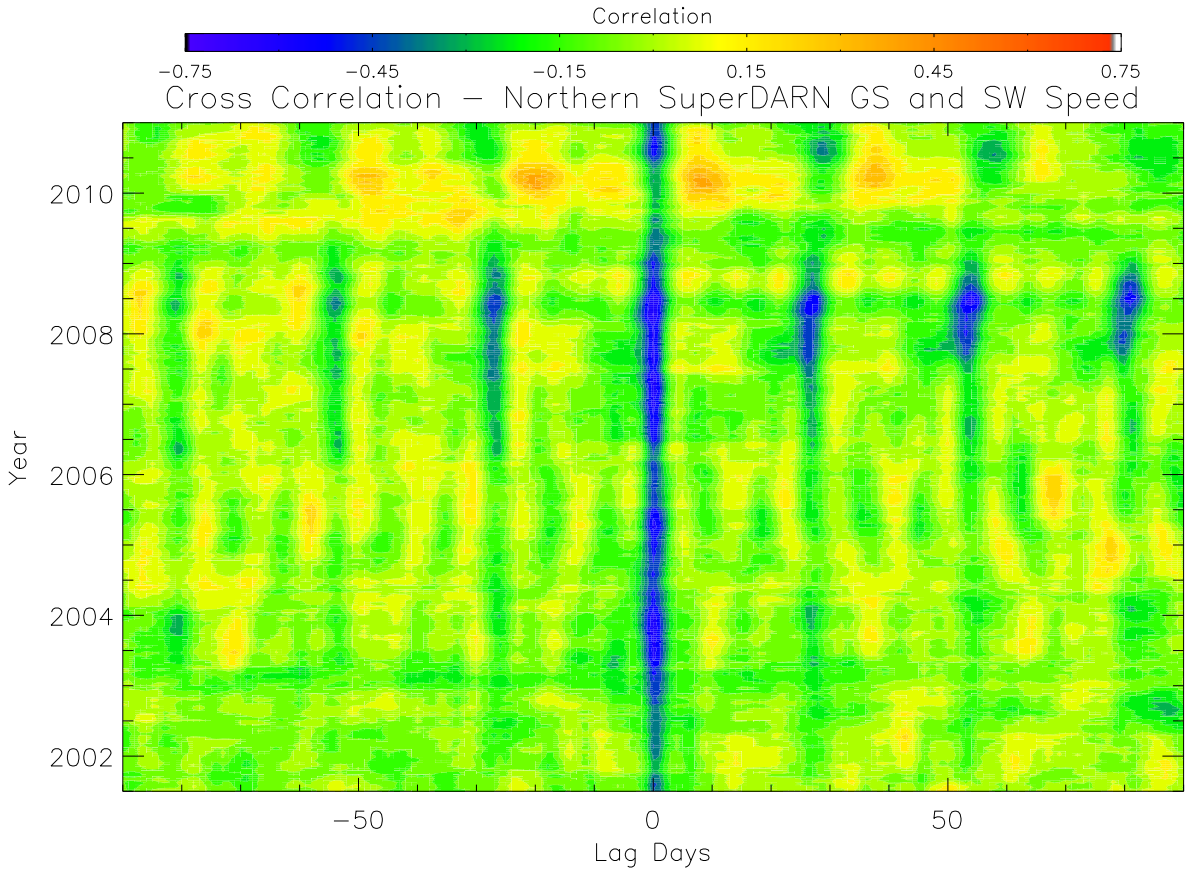

Figure 4.26: Cross–correlation of daily northern hemisphere SuperDARN ground scatter occurrence and daily averaged solar wind speed from 2001–2011.

4.3.3 Correlation Analysis

A linear cross–correlation analysis was performed on many of the available solar wind and ionospheric data sets. These are shown in Figures 4.26 through 4.33. The plots are a series of cross–correlations (shifted 180 days, i.e., +/- 90 days along the horizontal axis) and done every 10 days (vertical axis). All time series have a temporal resolution of one day. The color scale represents the correlation. One important thing to note is that the color scale is not the same for every plot (Figures 4.26–4.33). Each cross–correlation includes 361 days of data for both time series involved, and a cross–correlation is performed every 10 days. This method means that the vertical resolution of the plot is about 1 year, but this method does provide a useful view of how the relationship between the data sets change year by year over the course of the solar cycle.

The cross–correlation of the solar wind speed and the northern hemisphere SuperDARN ground scatter occurrence is shown in Figure 4.26. There is a strong anticorrelation between the solar wind speed and the SuperDARN ground scatter occurrence at zero offset between the data sets. This anticorrelation is on the order of -0.4 to -0.7. It appears to have a stronger anticorrelation during the declining phase of solar cycle 23 and in solar minimum (2003–2009) than in the years of increasing activity during the beginning of solar cycle 24 (2010–2011) and in the solar maximum of solar cycle 23 (2001.5–2003). In 2008 there is also a periodicity in the correlation which is approximately the synodic solar rotation period (27 days). The positive lags show a stronger anticorrelation at this periodicity than the negative lags. This might imply causality between the data sets, but more work is required to determine this. The 27–day periodicity can be attributed to the three dominant spectral components seen in both the solar wind speed and the northern hemisphere SuperDARN ground scatter occurrence spectrograms (Figures 4.21 and 4.24, respectively). The spectrograms of both data sets have strong 27–day, 13.5–day and 9–day periodicities during 2008. These periodicities are all multiples of 27 days (1, 1/2, and 1/3). Every 27 days the spectral components will align, but at other times they interact deconstructively.

The cross–correlation of the solar wind speed and the northern hemisphere SuperDARN ionospheric scatter occurrence is shown in Figure 4.27. Figure 4.27 is very similar to Figure 4.26, particularly the strong anticorrelation at zero lag. The solar wind speed and the SuperDARN ionospheric scatter occurrence is generally less strongly anticorrelated than the solar wind speed and SuperDARN ground scatter occurrence. This could be due to the fact that SuperDARN ground scatter is affected by ionospheric radio wave propagation, while the SuperDARN ionospheric scatter is affected by both the ionospheric radio wave propagation and the presence of plasma irregularities in the ionosphere (Section 3.1). However, the general similarity between the ground scatter and ionospheric scatter correlation plots suggests that the solar wind speed is affecting the propagation of radio waves through the ionosphere.

A cross–correlation was performed on the DMSP northern hemispherical power and the solar wind speed and the results are shown in Figure 4.28. There is a high correlation between the northern hemispherical power and the solar wind speed with a shift of zero days. This correlation reaches the highest value of 0.75 in 2008. This strong correlation means that

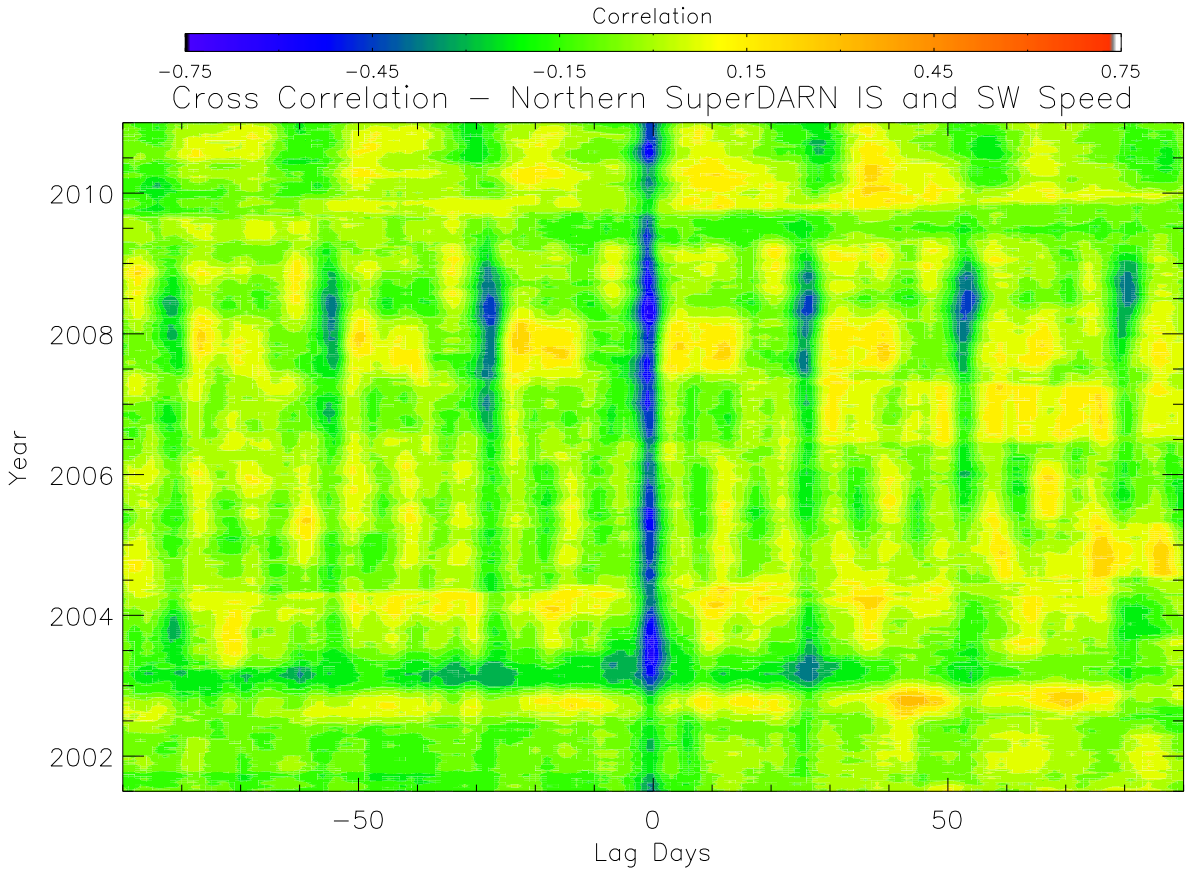

Figure 4.27: Cross–correlation of daily northern hemisphere SuperDARN ionospheric scatter occurrence and daily averaged solar wind speed from 2001–2011.

during times of high solar wind speed there is quite often a high hemispherical power (higher energy flux of precipitating electrons). This agrees with a study done by *Brautigam et al.* [1991]. The cross–correlation was also performed between the DMSP hemispherical power from the southern hemisphere and the solar wind speed, and the results were very similar. There was a strong correlation when the data sets were not offset. Since the hemispherical power is an estimate of the energy being deposited into a hemisphere by precipitating electrons, this means that during high solar wind speeds there is a higher energy flux of electrons precipitating into both the northern and southern areas poleward of the equatorward auroral boundary.

The cross–correlation of the DMSP northern hemispherical power and the SuperDARN ground scatter occurrence is shown in Figure 4.29. The northern hemispherical power is highly anticorrelated with the SuperDARN ground scatter occurrence at a lag of 0 days.

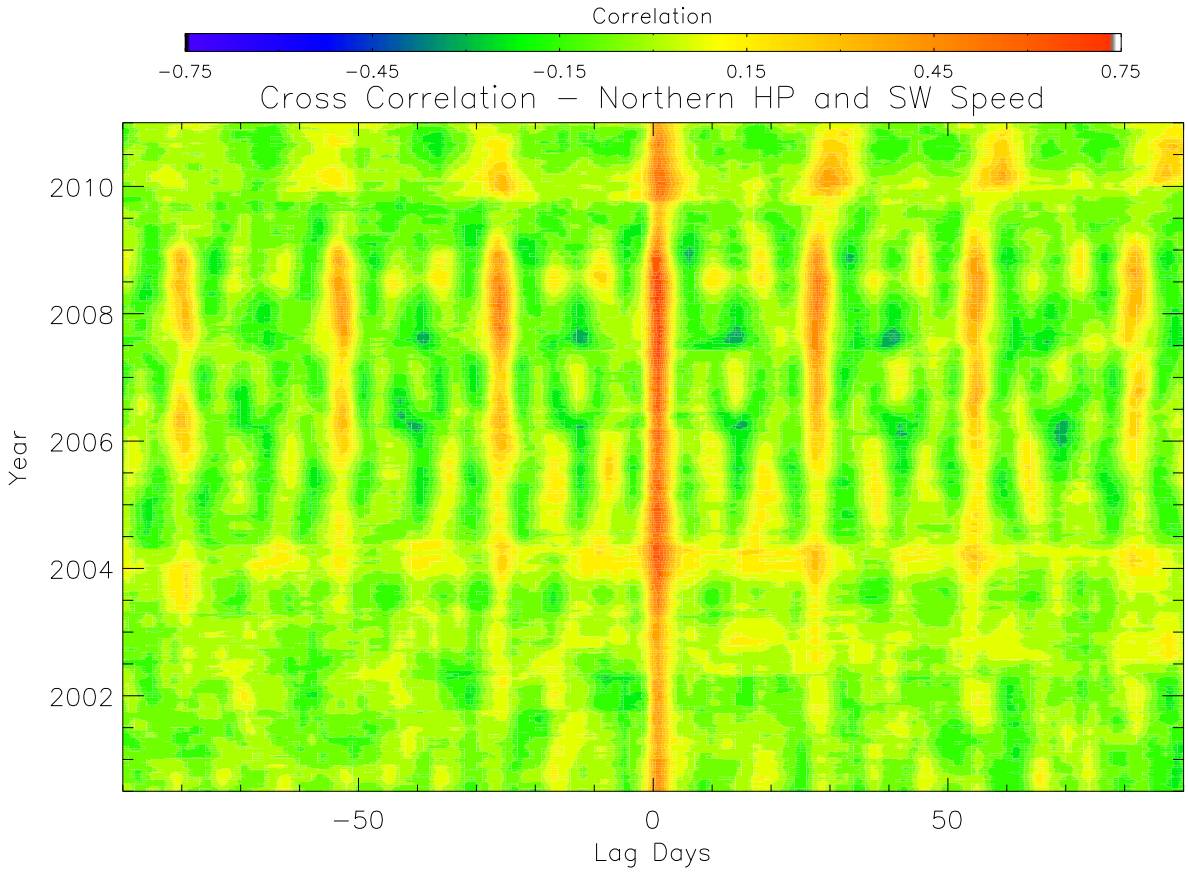

Figure 4.28: Cross–correlation of daily averaged DMSP northern hemispherical power and daily averaged solar wind speed from 2000–2011.

During periods of enhanced electron precipitation north of the equatorward auroral boundary fewer SuperDARN ground scatter echoes are recorded, and vice versa. From previous studies it is known that the electron precipitation into the Earth's auroral zones can affect properties of the ionosphere, such as the vertical electron density profile [*Kelley*, 1989; *Randall et al.*, 2005]. This, in turn, would affect radio wave propagation and could influence the SuperDARN scatter occurrence.

The cross–correlation of the solar sector angle and the northern hemisphere SuperDARN ground scatter occurrence is shown in Figure 4.30. In some years the parameters are significantly anticorrelated (-0.4 in 2008), but this varies over the years. The correlation values are much more periodic, in general, than the previous cross–correlation figures. In 2008, when the data shows the strong correlation, the data sets are offset by approximately ten days, which is a large delay for effects on the ionosphere to occur from changes in the IMF.

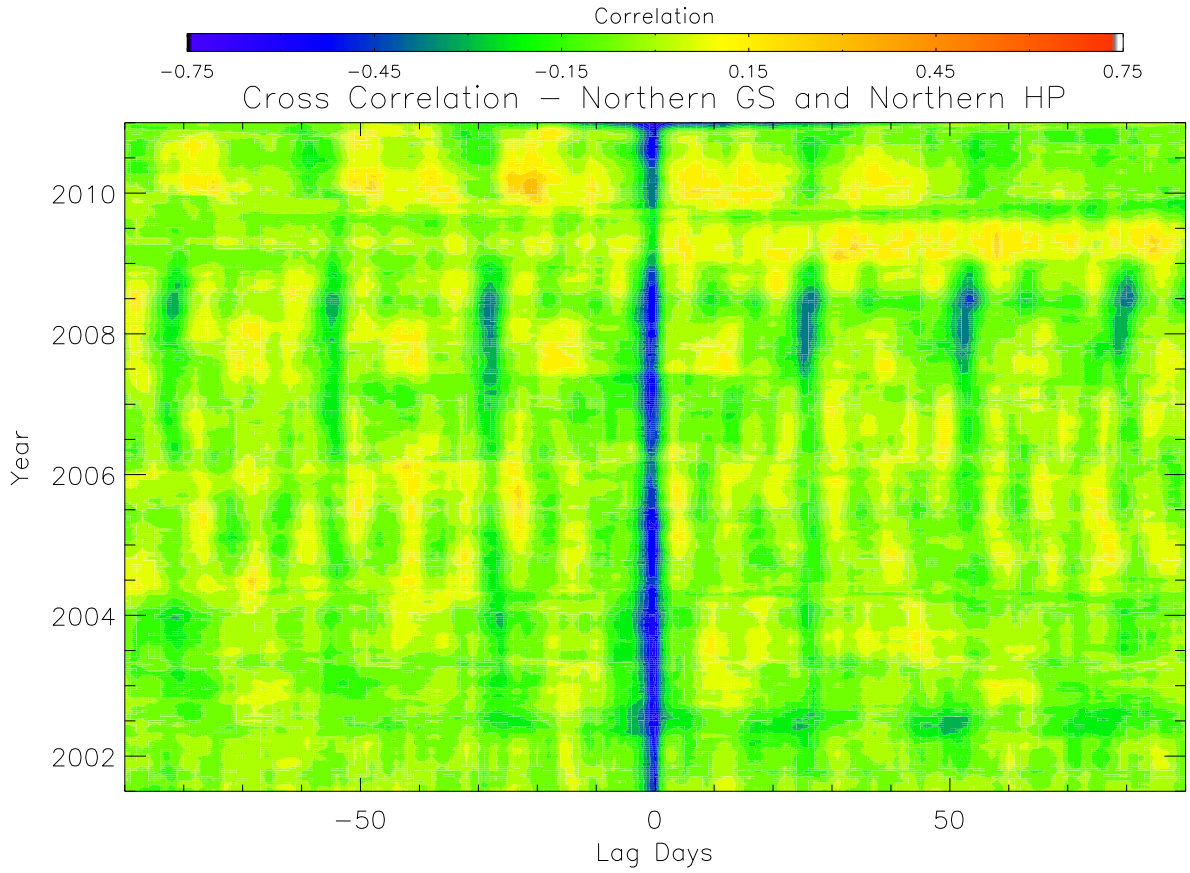

Figure 4.29: Cross–correlation of daily averaged DMSP northern hemispherical power and daily northern hemisphere SuperDARN ground scatter occurrence from 2001–2011.

The correlation between the data sets is not consistent across the years, and therefore it is unlikely that the solar sector angle plays a significant role in the SuperDARN ground scatter occurrence.

The B_z component of the IMF has been shown in the past to affect the SuperDARN ionospheric scatter occurrence rate, where more SuperDARN ionospheric scatter was recorded during periods of negative B_z [*Ballatore et al.*, 2001]. To investigate this, a cross–correlation analysis was done between the z–component of the IMF and the northern hemisphere SuperDARN ground scatter occurrence, which is shown in Figure 4.31. There is essentially no correlation between the northern hemisphere SuperDARN ground scatter occurrence and the IMF B_z. The same can be said for the IMF B_z and the northern hemisphere SuperDARN ionospheric scatter occurrence (not shown). While there was little to no correlation with the B_z component directly, there was an anticorrelation between the averaged standard deviation

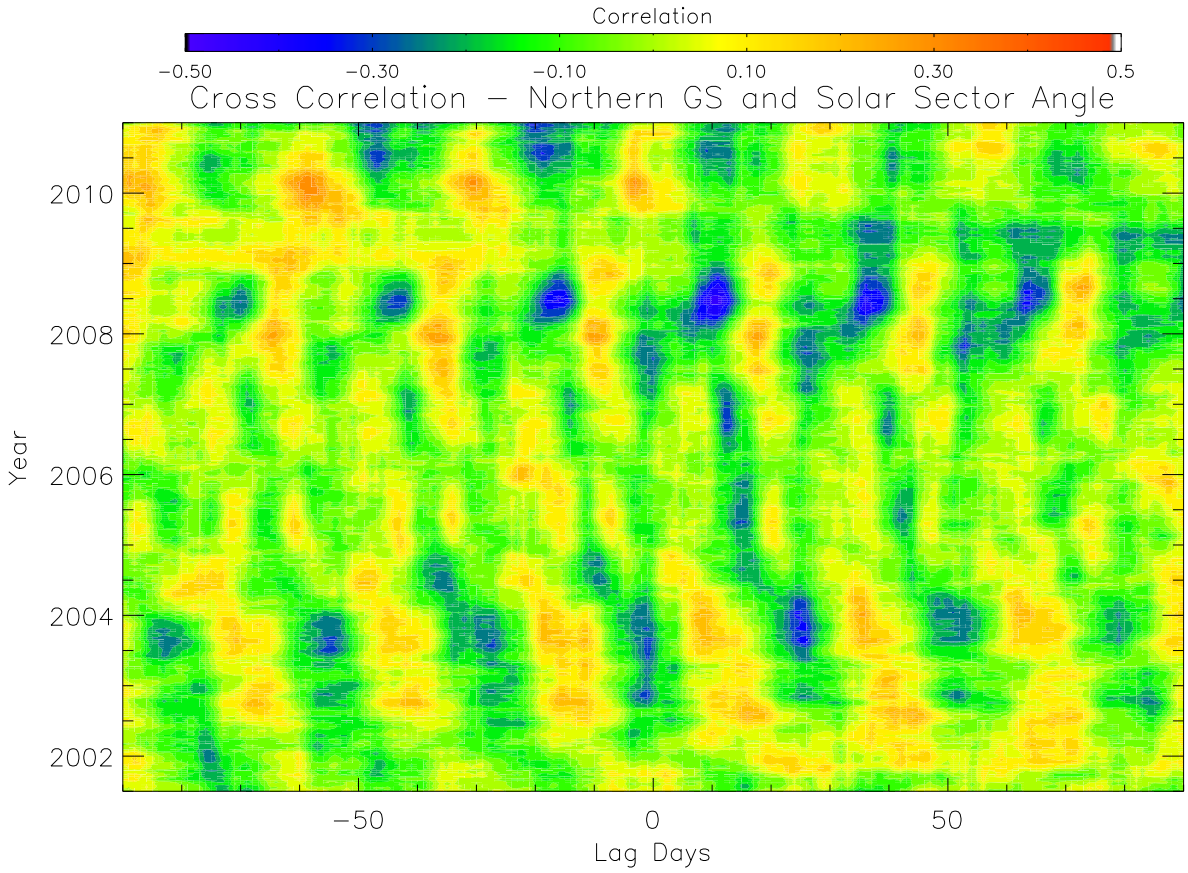

Figure 4.30: Cross–correlation of daily averaged solar sector angle and daily northern hemisphere SuperDARN ground scatter occurrence from 2001–2011.

in the z-component of the IMF and the northern hemisphere SuperDARN ground scatter occurrence (Figure 4.32). This persisted over the years 2003–2009, with a peak anticorrelation value of around -0.4. If the data sets are offset by just a couple days, the correlation goes from an anticorrelation to a correlation. This could be caused from a large decrease followed by an increase that occurs consistently in one data set's values, while the other data set only has an increase. The SuperDARN ionospheric scatter occurrence and the standard deviation in B_z were also anticorrelated in some years (not shown), but it was not consistent across the solar cycle and there was a smaller anticorrelation than that of Figure 4.32. From the results, when the z–component of the IMF is fluctuating more, there are fewer northern hemisphere SuperDARN ground scatter echoes.

Another solar property that could affect the SuperDARN measurement occurrence is the F10.7 cm electromagnetic flux. This is the flux of solar electromagnetic radiation emitted

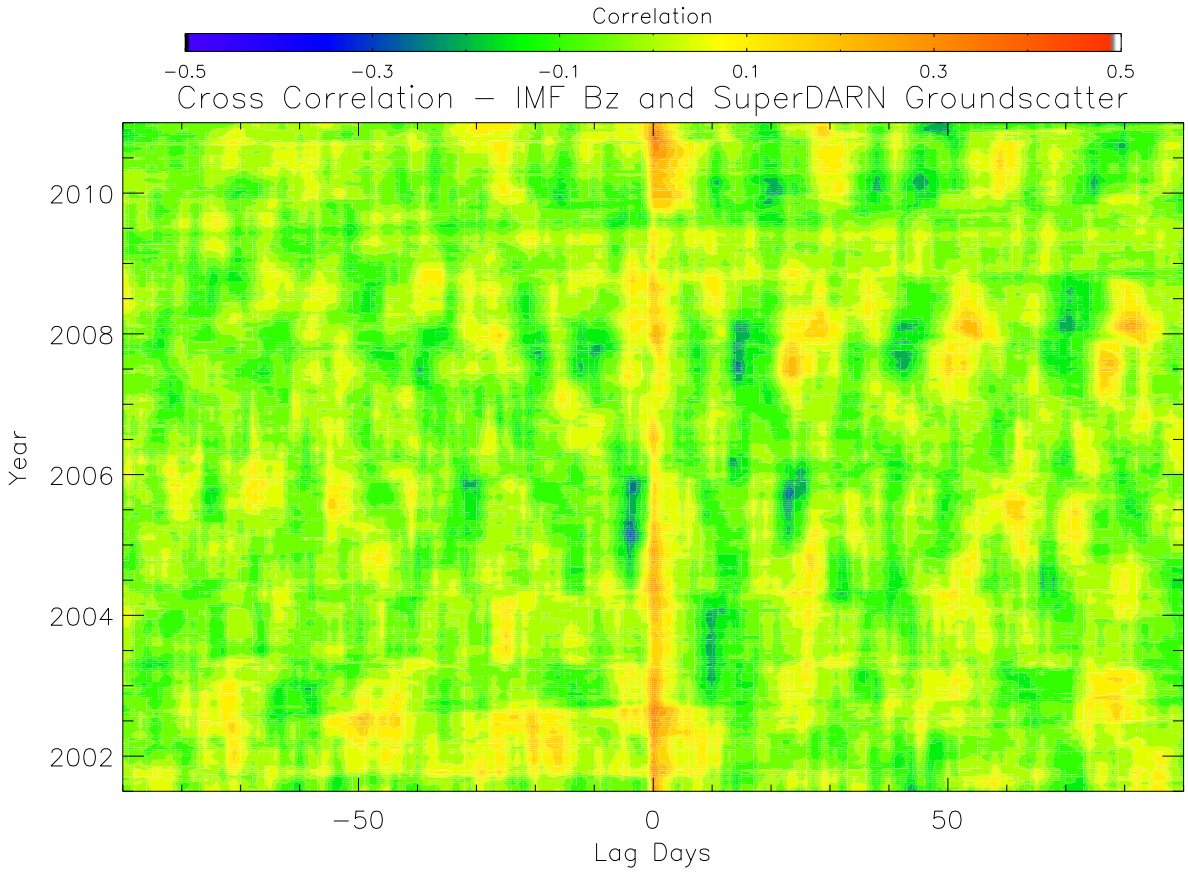

Figure 4.31: Cross–correlation of northern hemisphere SuperDARN ground scatter occurrence and daily averaged IMF B_z from 2001–2011.

from the sun with a wavelength of 10.7 cm. A change in the solar electromagnetic flux has been shown to affect the electron density profile of the Earth's ionosphere [*Roble*, 1976]. To investigate if the F10.7 cm affects the SuperDARN occurrence rate on the time scales being investigated in the present study (1 year), a cross–correlation of the F10.7 cm flux and the northern hemisphere SuperDARN ground scatter occurrence was performed. The results are presented in Figure 4.33. There is no consistent correlation between the two data sets to imply they are linearly related on time scales of approximately a year, which agrees with previous FFT studies [*Crowley et al.*, 2008].

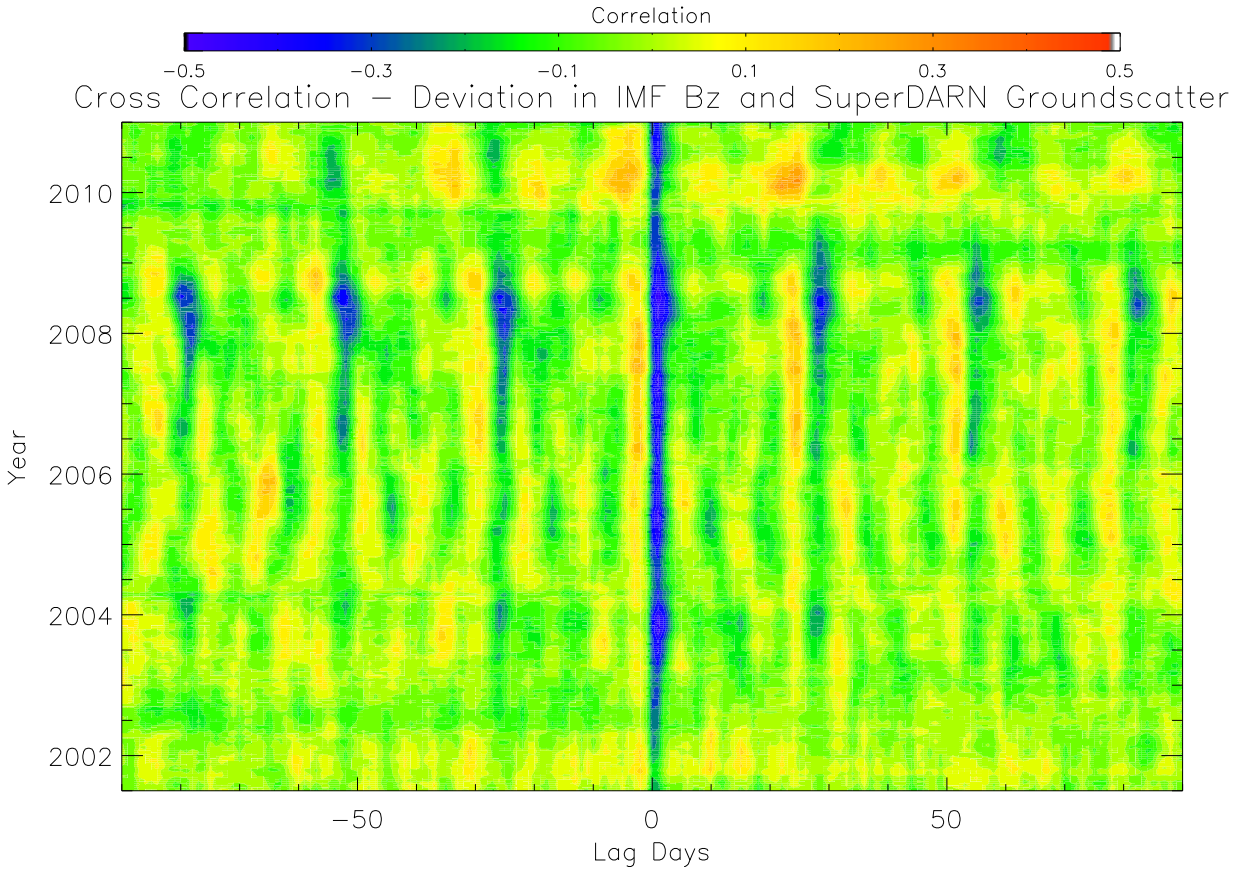

Figure 4.32: Cross–correlation of northern hemisphere SuperDARN ground scatter occurrence and daily averaged standard deviation of IMF B_z from 2001–2011.

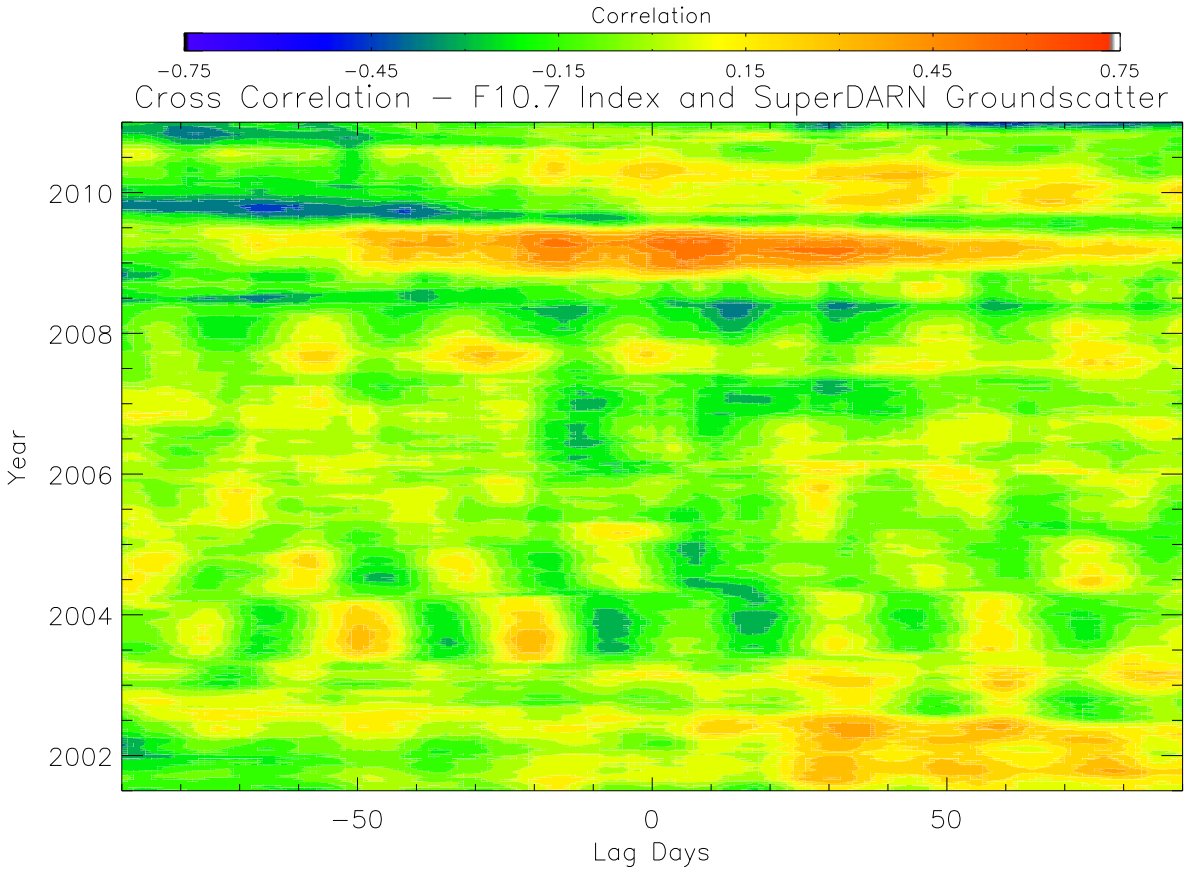

Figure 4.33: Cross–correlation of northern hemisphere SuperDARN ground scatter occurrence and daily averaged F10.7 cm Index from 2001–2011.

Chapter 5

Discussion, Summary and Conclusions

5.1 Discussion

There have been studies of the significance of a variety of solar wind and ionospheric parameters in affecting the SuperDARN ionospheric scatter occurrence. There have also been studies of the effects of the variable solar wind and IMF parameters on the ionosphere. These studies could provide a possible link between the solar wind conditions and the SuperDARN scatter occurrence.

In a study by *Danskin et al.* [2002], factors controlling F–region SuperDARN measurements were investigated. These factors included the radar transmission/signal frequency, the vertical plasma density profile of the ionosphere and the absorption of SuperDARN radio signals by the ionosphere. The data in this study included overlapping HF radar and incoherent scatter radar (ISR) measurements. The ISR is able to measure the electron density profile of the ionosphere, giving some insight into what could be affecting the SuperDARN scatter occurrence. A riometer provided radio wave absorption measurements. *Danskin et al.* [2002] found that the dominant factors in SuperDARN scatter occurrence rates were the SuperDARN operating frequency and the electron density profile. The F–region density required for a measurement to occur was found to be between $0.5 \times 10^{11}\ m^{-3}$ and $4 \times 10^{11}\ m^{-3}$ [*Danskin et al.*, 2002]. The radio wave absorption was shown to decrease the signal strength of the received SuperDARN echoes, but it did not significantly influence the occurrence rate of SuperDARN measurements.

In another study, *Kane et al.* [2012] investigated the effects of varying plasma parameters of the quiet time ionosphere on SuperDARN ionospheric scatter occurrence. *Kane et al.* [2012] found that different ionospheric parameters affected the SuperDARN scatter occurrence,

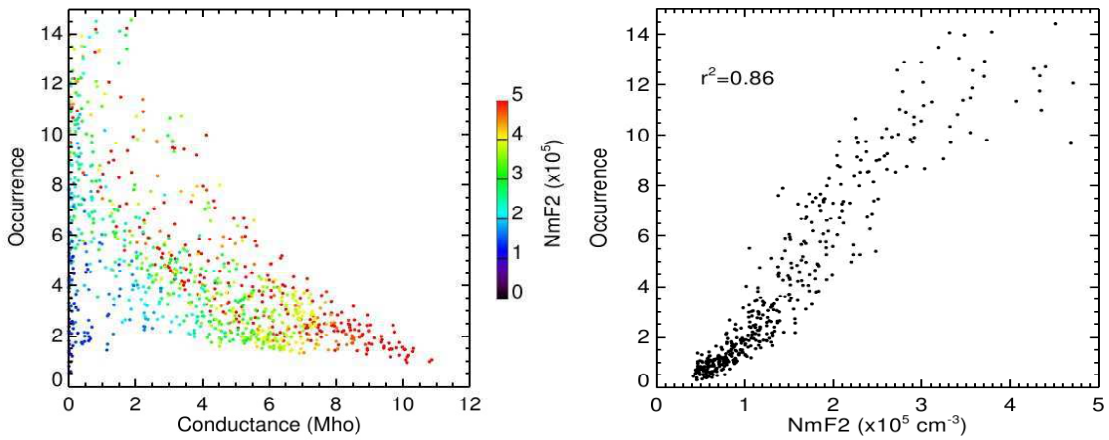

Figure 5.1: Scatter plots of the SuperDARN F–region scatter occurrence against the Pedersen conductivity for various NmF2 peaks in the day (left) and of the SuperDARN F–region measurement occurrence against the NmF2 peak in the night (right) [From *Kane et al.*, 2012].

depending on whether the radars were operated during the day or the night. At night the F-region electron density affected the amount of SuperDARN ionospheric echoes. In the right hand panel of Figure 5.1 is their scatter plot of the occurrence of SuperDARN ionospheric echoes as a function of the modeled NmF2 peak, where the NmF2 peak is the maximum electron density in the F region of the ionosphere. These data were recorded during the night. There is a very strong correlation between the two data sets, such that more SuperDARN F–region echoes are recorded when the F–region electron density peak is higher [*Kane et al.*, 2012]. On the left in Figure 5.1 is their scatter plot of the SuperDARN ionospheric scatter occurrence as a function of the modelled Pedersen conductance, color coded by the NmF2 peak value. This plot only includes data recorded during the day. There is an anticorrelation between the two data sets, meaning that for a larger Pedersen conductance there is a lower SuperDARN ionospheric scatter occurrence [*Kane et al.*, 2012]. From this study it is clear that there are at least two ionospheric properties that affect the SuperDARN scatter occurrence, and therefore multiple factors must be considered when determining long term trends in the SuperDARN data.

SuperDARN scatter occurrence can be significantly affected by changes in the propagation path of the SuperDARN radio wave. A change in the radio wave propagation path is the result of a change in the electron density profile of the ionosphere. This would affect both

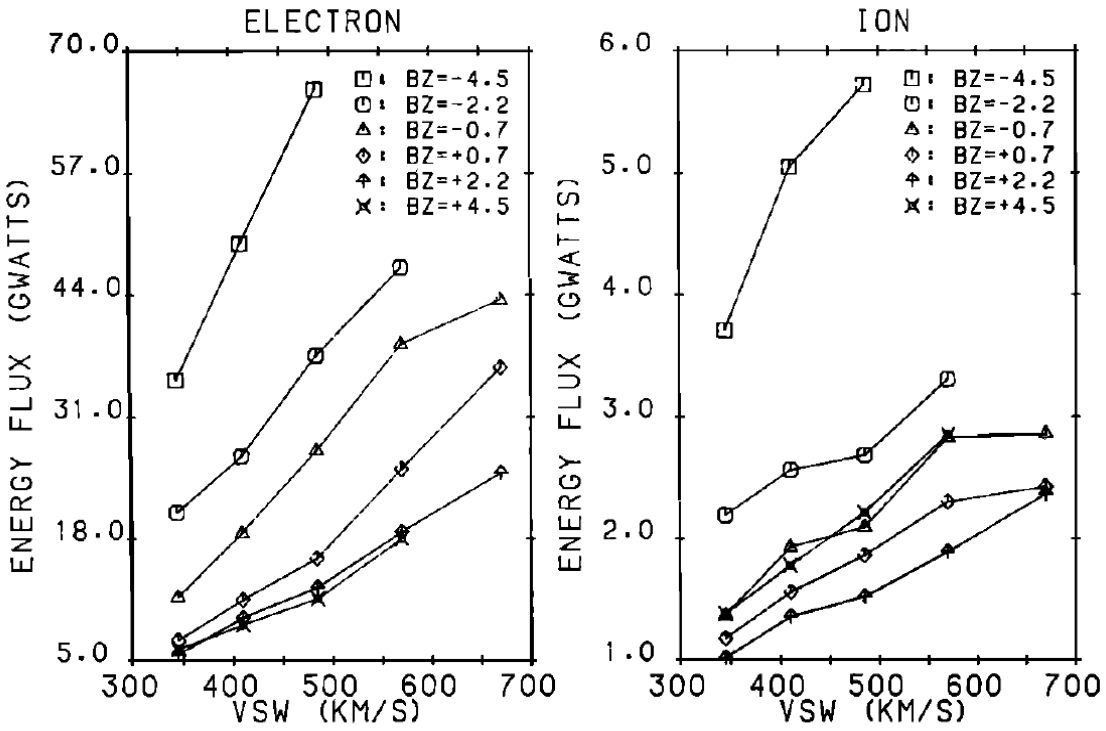

Figure 5.2: The relationship between the energy flux of precipitating particles into the auroral zone and the solar wind speed for various IMF B_z values [From *Brautigam et al.*, 1991].

ionospheric scatter and ground scatter. The occurrence rates of both ionospheric scatter and ground scatter echoes presented in this thesis are similar, suggesting that it is the ionosphere plasma density that is modified. The strong anticorrelations between the solar wind speed and the SuperDARN ionospheric scatter and ground scatter occurrence (Section 4.3.3) suggest that the solar wind speed is altering the electron density profile of the ionosphere.

A previous study related the solar wind speed to the electron and ion precipitation in the auroral zones. *Brautigam et al.* [1991] showed that the electron and ion precipitation into a hemisphere's auroral zone varied linearly with the solar wind speed. The data presented in the study is reproduced in Figure 5.2. For a variety of IMF B_z values, there is a clear increase in the ion and electron energy flux of energetic particle precipitation with an increase in the solar wind speed. This agrees with Figure 4.28, in which there was a clear linear correlation between the solar wind speed and the DMSP hemispherical power (for electrons). Changing particle precipitation affects the electron density profiles in the ionosphere [*Kelley*, 1989], which, in turn, is expected to affect the SuperDARN scatter occurrence.

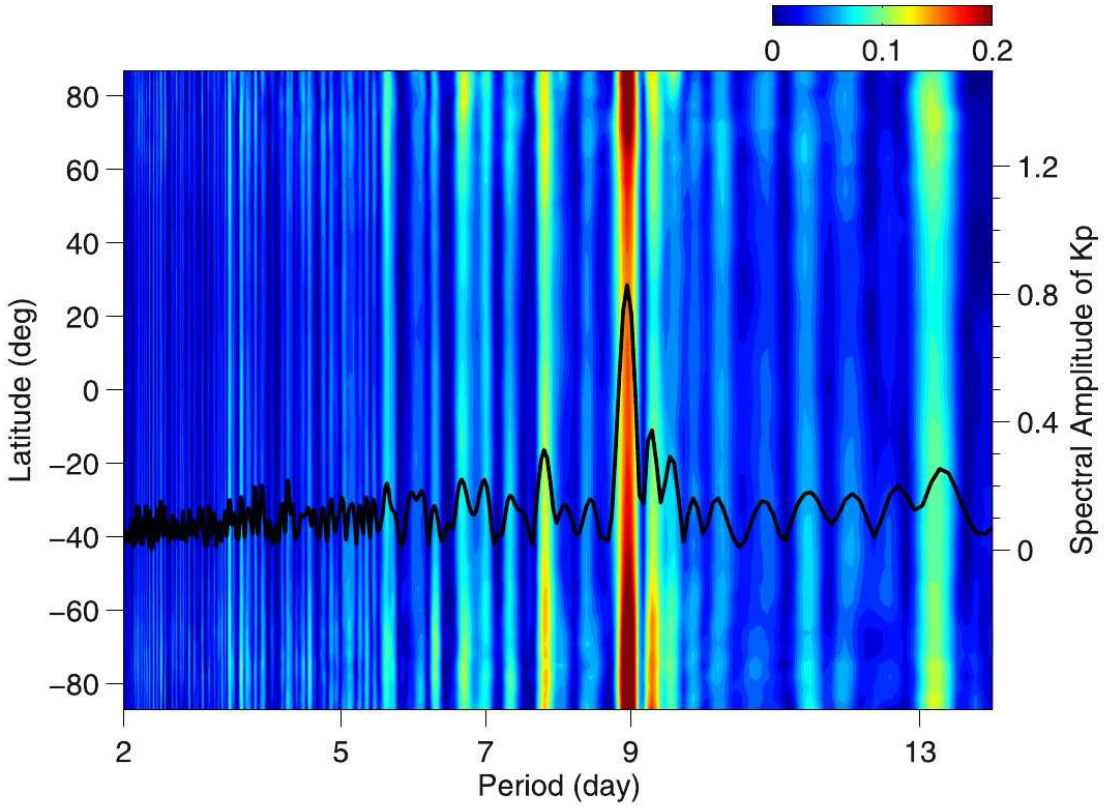

Figure 5.3: A spectral analysis of the neutral thermospheric densities at 400km for multiple latitudes in 2005. The spectral analysis for the Kp index over the same time period is superposed and shown by the black line. There is a strong periodicity of 9 days seen in both data sets. [From *Lei et al.*, 2008a]

In addition to the work discussed above, there are some interesting results from past studies related to the FFT spectral analysis. The 9–day and 6.75–day periodicities seen in many of the parameters analysed in Section 4.3.2 are evident in other ionospheric data sets. *Lei et al.* [2008c,a] observed a 9–day periodicity in the neutral density of the thermosphere at 400 km in 2005–2008 and a 7–day periodicity in the neutral density of the thermosphere at 400 km in 2006. The dominant periodicities in the thermospheric neutral density at 400 km for all latitudes in 2005 are shown in Figure 5.3, with the spectral analysis of the Kp index over the same year superposed. The 7–day and 9–day periodicities in the thermospheric neutral density and the years when they occur are very similar to those periodicities found in the solar wind speed data. The 9–day periodicity was also found in the global total electron content (TEC) [*Lei et al.*, 2008b], the polar thermospheric neutral winds data [*Lei et al.*, 2008b], and the power radiated from the infrared cooling of NO and CO_2 at altitudes of 100–

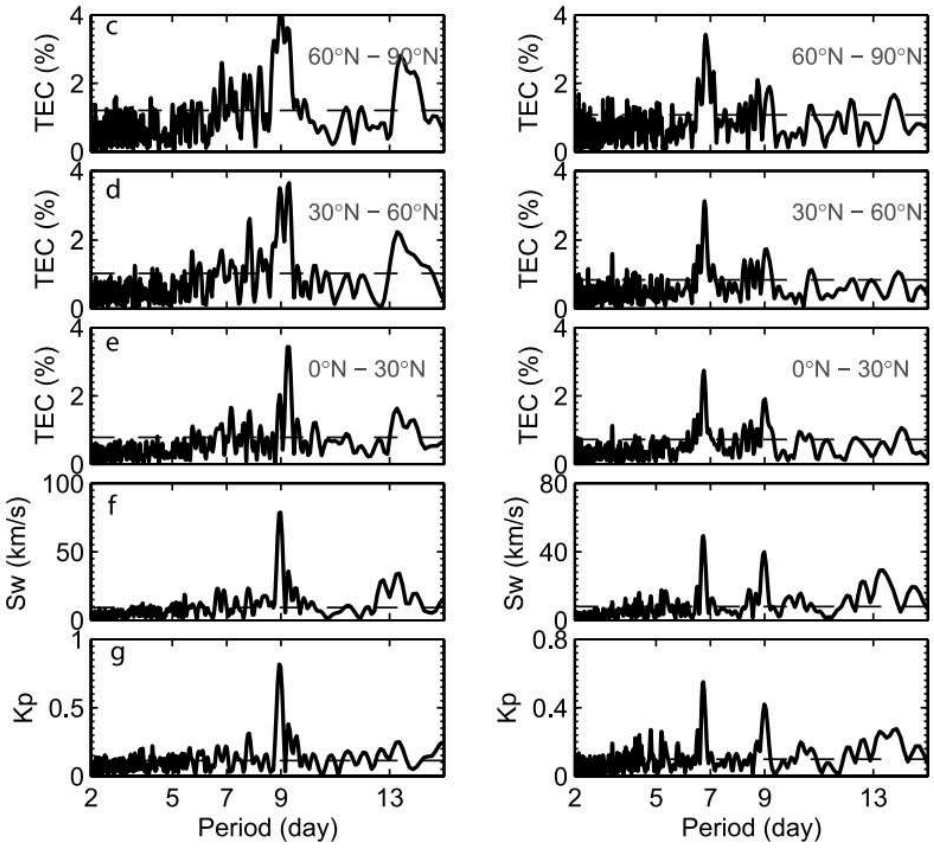

Figure 5.4: Spectral analysis performed on the TEC at varying latitudes (latitude displayed in panels), the solar wind speed and the Kp index for the years 2005 (left) and 2006 (right), where the horizontal dashed lines represent the 95% significance level. The analysis was performed using Lomb–Scargle periodograms of percent residuals from the 11–day running mean of the data. There is a strong spectral peak at a periodicity of 9 days seen in all the panels for 2005, while there is a smaller peak at 9 days seen in the data for 2006. [From *Lei et al.*, 2008b]

200 km [*Mlynczak et al.*, 2008]. The 9–day periodicity seen in the TEC is shown in Figure 5.4 for 2005 and 2006. The power radiated from the infrared cooling of NO was also shown to have a periodicity of 7 days in 2006 [*Mlynczak et al.*, 2010]. There was no 9–day periodicity in the 10.7 cm solar flux during this time period [*Lei et al.*, 2008a], so it is more likely that the solar wind and IMF properties are responsible for this 9–day periodicity in the ionospheric measurements. The means by which this is accomplished remains to be determined.

5.2 Summary

In Chapter 4, the solar wind and IMF influences on SuperDARN scatter occurrence were investigated using a variety of techniques. A superposed epoch analysis, a linear cross–correlation analysis and an FFT analysis were performed. The results from these investigations are summarized, as follows:

1) The solar wind speed, solar wind density and the IMF change over the course of a solar cycle (Figures 4.1 and 4.2). The solar wind speed was faster during the decline from solar maximum and slower during solar minimum. The solar wind density was higher at solar maximum than at solar minimum, and the IMF magnitude was also larger at solar maximum than at solar minimum. The IMF B_x and B_y components were anticorrelated.

2) During a solar sector boundary crossing (SBC), the IMF magnitude, the solar wind speed and the solar wind density change significantly. This is summarized in Figures 4.6, 4.7 and 4.8. The IMF magnitude increases during a SBC, though has a slight decrease at the moment of the crossing. The IMF magnitude decays to its pre–crossing levels two days following the SBC. The solar wind speed decreases in the days before a SBC, reaching a minimum at the SBC, and increases during the days following the SBC. The solar wind density increases during the approach of the SBC and reaches a peak at the time of the SBC. These IMF and solar wind parameters show independence from the polarity of the SBC (away–to–toward or toward–to–away).

3) Within a day of a SBC, the SuperDARN scatter occurrence tends to peak, independent of the SBC polarity. This was evident in Figures 4.9, 4.10, 4.11 and 4.12. The standard deviations were quite a bit larger than the change in the SuperDARN scatter occurrence, which could be cause for caution when deriving conclusions from these results.

4) The DMSP hemispherical power increased in both the southern and northern hemispheres during and after a SBC. This can be seen in Figures 4.13 and 4.14. There appears to be a small peak in the hemispherical power at the time of the SBC, along

with a gradual increase in the hemispherical power around the time of the SBC. The hemispherical power increases during the crossing of the SBC independent of the polarity of the SBC.

5) The epoch analysis of the midnight boundary index for both the southern and northern hemispheres shows an equatorward motion of the equatorward boundary of the auroral oval during a SBC. This can be seen in Figures 4.15 and 4.16. The change in the auroral oval appears to be independent of the polarity of the SBC.

6) There was little to no change in the uncorrected and corrected neutron monitor counts (from GCRs) during the SBC. The superposed epoch plots of uncorrected neutron monitor counts can be seen in Figures 4.17 and 4.18. The variation from the mean is less than one percent during the SBC for these plots.

7) A fast fourier transform (FFT) analysis was performed on the sector angle of the IMF. This is shown in Figure 4.20. A strong periodicity at 27 days is seen throughout the data, and a periodicity of 13.5 days is seen in the years 2005 to 2009. The 27–day periodicity corresponds to a 2–sector solar structure and the 13.5–day periodicity corresponds to a 4–sector solar structure.

8) The FFT analysis was performed on the solar wind speed. Strong periodicities were seen at 27 days, 13.5 days, 9 days and 6.75 days, which can be seen in Figure 4.21. It is likely that, since there is a change in the solar wind speed during SBCs that is independent of the SBC polarity, there should be solar wind speed periodicities at half the periodicity of the sector angle. This can be seen in the 13.5–day and 6.75–day periodicity peaks in the solar wind speed. The 9–day periodicity from 2005 to 2008 is believed to be due to recurring high speed streams from persistent source regions on the Sun [*Emery et al.*, 2011].

9) The IMF magnitude was also fourier analysed, and this is summarized in Figure 4.22. The dominant periodicities are at 13.5 days, 9 days and 6.75 days. The 9–day periodicity is interesting, as it is a consistently dominant periodicity throughout the solar cycle. The 13.5–day and 6.75–day periodicity likely reflect the changes in the IMF magnitude

during SBCs, which are independent of SBC polarity, resulting in periodicities half that of those seen in the solar sector angle data (Figure 4.20).

10) The DMSP northern hemispherical power, the northern hemisphere SuperDARN ground scatter occurrence, and the northern hemisphere SuperDARN ionospheric scatter occurrence were all processed using the FFT analysis. Figures 4.23 to 4.25 show the results. All three data sets have a strong 9–day periodicity from 2004–2008. There are also dominant peaks at 27 days and 13.5 days during this time period. During solar maximum and the decline of solar maximum there are many very low frequency peaks that are evident in the fourier spectrograms of the SuperDARN data. This may be due to programming issues that were improved upon in 2006, after which time these peaks largely disappeared.

11) A cross–correlation analysis was done between many ionospheric, solar wind and IMF parameters. The resulting plots are found in Section 4.3.3. During the decline of solar maximum and through solar minimum a strong anticorrelation exists between the solar wind speed and the SuperDARN ground scatter occurrence, reaching a peak of -0.7 in 2008. There is a comparable anticorrelation between the SuperDARN ionospheric scatter and the solar wind speed during the same time period, but the magnitude of the anticorrelation is weaker. The DMSP northern hemispherical power and the solar wind speed were strongly correlated for the whole solar cycle. The DMSP northern hemispherical power and the northern hemisphere SuperDARN ground scatter occurrence were strongly anticorrelated in all years except for 2009. The F10.7 index, the solar sector angle and the z–component of the IMF all had a correlation analysis performed on them with the northern hemisphere SuperDARN ground scatter occurrence. No significant or consistent correlations were found between any of these parameters and the northern hemisphere SuperDARN ground scatter occurrence.

5.3 Conclusions

The superposed epoch analysis was inconclusive in many regards, as the standard deviations in most of the cases were large. Generally, there was a peak seen in the SuperDARN scatter occurrences at the sector boundary crossing, which may be related to the decrease in the solar wind speed or increase in the solar wind density at the sector boundary crossing. The polarity of the sector boundary crossing did not affect the results of the superposed epoch analysis on any of the parameters. The neutron monitor counts do not appear to be affected by crossing the solar sector boundary, even though the IMF magnitude appears to change across the boundary. More work is required to determine why the neutron monitor counts do not appear to be affected by the change in the IMF magnitude across the boundary, though it likely has to do with the size of the IMF structure, as cosmic rays can have gyroradii that are extremely large (on the order of several AU).

The 9–day periodicity in the SuperDARN scatter occurrences can be attributed to the solar wind and IMF. The solar wind and IMF magnitude have a 9–day periodicity in 2004–2008, while past studies have shown that during this time period the F10.7 flux and the solar electromagnetic flux do not have an evident 9–day periodicity [*Lei et al.*, 2008a]. The 9–day periodicity is also seen in the DMSP hemispherical power, which is to be expected due to the linear relationship between the solar wind speed and the auroral particle precipitation [*Brautigam et al.*, 1991]. Past studies have shown that SuperDARN scatter occurrence rates are more affected by the radio wave propagation path than by radio wave absorption. Changes in the electron density profile of the ionosphere can therefore affect the SuperDARN scatter occurrence. One mechanism by which the electron density profile could be changed is through particle precipitation [*Kelley*, 1989].

It has also been shown that the solar wind speed and SuperDARN scatter occurrences are anticorrelated during the decline of solar max and during solar minimum. The SuperDARN scatter occurrences are anticorrelated with the DMSP hemispherical power as well, and the DMSP hemispherical power and solar wind speed are correlated. The hemispherical power and solar wind speed correlation could be due to direct precipitation, magnetospheric wave generation or some other mechanism. The correlation analysis between the Super-

DARN echoes and the F10.7 index, the solar sector angle and the z–component of the IMF displayed little to no correlation. The SuperDARN scatter occurrences are therefore likely being affected by ionospheric particle precipitation, which has been shown to be correlated with the solar wind speed. This agrees with the results from the FFT analysis. By including previous studies on SuperDARN measurement occurrence, it appears that the SuperDARN measurement occurrences are being affected by changes to the electron density profile, the likely cause of which is particle precipitation.

5.4 Possible Future Work

Many questions have been raised with regards to what is affecting the SuperDARN measurement occurrence, and some possible explanations presented. A few of the outstanding questions are presented below, along with possible methods by which one could answer them:

1) How does the solar wind speed and particle precipitation affect the electron densities in the ionosphere?

   Incoherent scatter radar (ISR) data can be used to examine the electron density profiles of the ionosphere at certain locations. When compared with the solar wind speed and the particle precipitation data sets (such as DMSP), it can be determined if and how the solar wind speed is changing electron density profiles. Generally ISRs only operate over short time periods, but this study would benefit from both event studies and trend analysis of longer time series. The Svalbard ISR ran in a special "continuous" mode for most of 2007, which would be a great data set to examine since the radar ran during the time period that there was a dominant 9–day periodicity in many of the data sets, unrelated to the F10.7 index.

2) Is there a local time dependence for solar wind and IMF effects on the SuperDARN scatter occurrence?

   The SuperDARN data can be separated by MLT, though it was not done in this study. This could be used to determine if, for example, the dayside or nightside are more affected by changing solar wind speeds and particle precipitation. Dayside effects are

likely due to more direct interaction with the solar wind and IMF, while nightside processes are expected to be related more likely to magnetospheric processes, such as substorms. Perhaps the change in SuperDARN scatter occurrence is more prominent in the evening sector, as there is a lower background ionization level in the ionosphere during this time.

3) Does the latitude of the SuperDARN radar affect the results?

The SuperDARN radars can be classified into three main classes: mid–latitude, auroral zone and PolarDARN radars. Separating the data into these three regions would then determine if the effect of solar wind speed and particle precipitation on the SuperDARN measurement occurrence is confined to regions that map into the magnetosphere or out into the solar wind in the polar cap. The hemispherical power data set used in the current study includes all electron precipitation poleward of the equatorward auroral boundary, so it would be interesting to determine where the SuperDARN scatter occurrence is actually being affected. In these studies it would be useful to compare SuperDARN observations with DMSP particle data directly, rather than the more simplified DMSP indices.

4) Do other atmospheric properties display a correlation with the solar wind speed and particle precipitation?

The initial interest in this project came about because of the links between space and tropospheric weather. It is imperative to extend the current studies to atmospheric properties at altitudes below the ionosphere. As a specific example, past studies show a strong 9–day periodicity in many different atmospheric data sets during a certain time period (2005–2008), and this would be a good, well–observed interval to analyze. There is an extensive database of ozone and atmospheric aerosol data from the OSIRIS instrument [*Llewellyn et al.*, 2004] located at the University of Saskatchewan. This data set extends over a whole solar cycle and therefore would be excellent for comparison with space weather data sets.

References

Akasofu, S. (1981), Energy coupling between the solar wind and the magnetosphere, *Space Science Rev.*, *28*(2), 121–190, doi: 10.1007/BF00218810.

Baker, D. (2002), How to cope with space weather, *Science*, *297*(5586), 1486–1487, doi: 10.1126/science.1074956.

Ballatore, P., J. Villain, N. Vilmer, and M. Pick (2001), The influence of the interplanetary medium on SuperDARN radar scattering occurrence, *Ann. Geophys.*, *18*(12), 1576–1583, doi: 10.1007/s00585-001-1576-2.

Blaunstein, N., and E. Plohotniuc (2008), *Ionosphere and Applied Aspects of Radio Communication and Radar*, CRC Press.

Boudouridis, A., E. Zesta, R. Lyons, P. Anderson, and D. Lummerzheim (2003), Effect of solar wind pressure pulses on the size and strength of the auroral oval, *J. Geophys. Res.*, *108*(A4), 8012, doi: 10.1029/2002JA009373.

Bradbury, N. (1938), Ionization, negative-ion formation, and recombination in the ionosphere, *Terr. Magn. Atmos. Elect.*, *43*(1), 55–66, doi: 10.1029/TE043i001p00055.

Brautigam, D., M. Gussenhoven, and D. Hardy (1991), A statistical study on the effects of IMF Bz and solar wind speed on auroral ion and electron precipitation, *J. Geophys. Res.*, *96*(A4), 5525–5538, doi: 10.1029/91JA00157.

Budden, K. (1961), *Radio Waves in the Ionosphere*, Cambridge University Press.

Cane, H., G. Wibberenz, I. Richardson, and T. von Rosenvinge (1999), Cosmic ray modulation and the solar magnetic field, *Geophys. Res. Lett.*, *26*(5), 565–568, doi: 10.1029/1999GL900032.

Clem, J., and L. Dorman (2000), Neutron monitor response functions, *Space Science Rev.*, *93*(1), 335–359, doi: 10.1023/A:1026508915269.

Cravens, T. E. (1997), *Physics of Solar System Plasmas*, Cambridge University Press.

Crowley, G., A. Reynolds, J. Thayer, J. Lei, L. Paxton, A. Christensen, Y. Zhang, R. Meier, and D. Strickland (2008), Periodic modulations in thermospheric composition by solar wind high speed streams, *Geophys. Res. Lett.*, *35*(21), doi: 10.1029/2008GL035745.

Curtis, J., and L. Adams (1987), Defense meteorological satellite program, *Aerospace and Electronic Systems Magazine, IEEE*, *2*(3), 13–17, doi: 10.1109/MAES.1987.5005348.

Danskin, D., A. Koustov, T. Ogawa, N. Nishitani, S. Nozawa, S. Milan, M. Lester, D. Andre, et al. (2002), On the factors controlling occurrence of F-region coherent echoes, *Ann. Geophys.*, *20*(9), 1385–1397.

Dungey, J. (1961), Interplanetary magnetic field and the auroral zones, *Physical Review Letters*, *6*(2), 47–48, doi: 10.1103/PhysRevLett.6.47.

Emery, B., I. Richardson, D. Evans, F. Rich, and G. Wilson (2011), Solar rotational periodicities and the semiannual variation in the solar wind, radiation belt, and aurora, *Solar Physics*, *274*(1), 399–425, doi: 10.1007/s11207-011-9758-x.

Evans, D. (1987), Global statistical patterns of auroral phenomena, in *Proceedings of the Symposium on Quantitative Modeling of Magnetospheric-Ionospheric Coupling Processes*, vol. 325.

Fairfield, D. (1971), Average and unusual locations of the Earth's magnetopause and bow shock, *J. Geophys. Res.*, *76*(28), 6700–6716, doi: 10.1029/JA076i028p06700.

Fairfield, D. H., and J. D. Scudder (1985), Polar rain: Solar coronal electrons in the Earth's magnetosphere, *J. Geophys. Res.*, *90*(A5), 4055–4068, doi: 10.1029/JA090iA05p04055.

Freeman, J. W. (2001), *Storms in Space*, Cambridge University Press.

Gosling, J., and V. Pizzo (1999), Formation and evolution of corotating interaction regions and their three dimensional structure, *Space Science Rev.*, *89*(1), 21–52, doi: 10.1023/A:1005291711900.

Gray, L., et al. (2010), Solar influences on climate, *Rev. Geophys.*, *48*(4), RG4001, doi: 10.1029/2009RG000282.

Greenwald, R. A., et al. (1995), DARN/SuperDARN, *Space Science Rev.*, *71*(1), 761–796, doi: 10.1007/BF00751350.

Gussenhoven, M., D. Hardy, and W. Burke (1981), DMSP/F2 electron observations of equatorward auroral boundaries and their relationship to magnetospheric electric fields, *J. Geophys. Res.*, *86*(A2), 768–778, doi: 10.1029/JA086iA02p00768.

Haigh, J. (1994), The role of stratospheric ozone in modulating the solar radiative forcing of climate, *Nature*, *370*(6490), 544–546, doi: 10.1038/370544a0.

Haigh, J. (2003), The effects of solar variability on the Earth's climate, *Philosophical Transactions of the Royal Society of London. Series A: Mathematical, Physical and Engineering Sciences*, *361*, 95–110, doi: 10.1098/rsta.2002.1111.

Hardy, D., L. Schmitt, M. Gussenhoven, P. Marshall, H. Yeh, T. Schumaker, A. Huber, and J. Pantazis (1984), Precipitating electron and ion detectors (SSJ/4) for the block 5D/flights 6-10 DMSP (Defense Meteorological Satellite Program) satellites: Calibration and data presentation, *Tech. rep.*, DTIC Document.

Hargreaves, J. (1969), Auroral absorption of HF radio waves in the ionosphere: A review of results from the first decade of riometry, *Proceedings of the IEEE*, *57*(8), 1348–1373, doi: 10.1109/PROC.1969.7275.

Hargreaves, J. K. (1992), *The Solar-Terrestrial Environment*, Cambridge University Press.

Hathaway, D. H., and R. M. Wilson (2004), What the sunspot record tells us about space climate, *Solar Physics*, *224*, 5–19, doi: 10.1007/s11207-005-3996-8.

Hundhausen, A., S. Bame, J. Asbridge, and S. Sydoriak (1970), Solar wind proton properties: Vela 3 observations from July 1965 to June 1967, *J. Geophys. Res.*, *75*(25), 4643–4657, doi: 10.1029/JA075i025p04643.

Jackson, J., and J. Seddon (1958), Ionosphere electron-density measurements with the navy Aerobee-Hi rocket, *J. Geophys. Res.*, *63*(1), 197–208, doi: 10.1029/JZ063i001p00197.

Kane, T., R. Makarevich, and J. Devlin (2012), HF radar observations of ionospheric backscatter during geomagnetically quiet periods, *Ann. Geophys.*, *30*(1), 221–233, doi: 10.5194/angeo-30-221-2012.

Kelley, M. (1989), *The Earth's Ionosphere: Plasma Physics and Electrodynamics*, Academic Press.

King, J., and N. Papitashvili (2012), One min and 5-min solar wind data sets at the Earth's bow shock nose, *Tech. rep.*, GSFC/SPDF and ADNET Systems, Inc.

Kivelson, M., and C. Russell (1995), *Introduction to Space Physics*, Cambridge University Press.

Kokubun, S., T. Yamamoto, M. Acuña, K. Hayashi, K. Shiokawa, and H. Kawano (1994), The Geotail magnetic field experiment, *J. Geomag. Geoelectr.*, *46*(1), 7–22.

Larsen, M., and M. Kelley (1977), A study of an observed and forecasted meteorological index and its relation to the interplanetary magnetic field, *Geophys. Res. Lett.*, *4*(8), 337–340, doi: 10.1029/GL004i008p00337.

Lei, J., J. Thayer, J. Forbes, E. Sutton, R. Nerem, M. Temmer, and A. Veronig (2008a), Global thermospheric density variations caused by high-speed solar wind streams during the declining phase of solar cycle 23, *J. Geophys. Res.*, *113*(A11), A11,303, doi: 10.1029/2008JA013433.

Lei, J., J. Thayer, J. Forbes, Q. Wu, C. She, W. Wan, and W. Wang (2008b), Ionosphere response to solar wind high-speed streams, *Geophys. Res. Lett.*, *35*(19), doi: 10.1029/2008GL035208.

Lei, J., J. Thayer, J. Forbes, E. Sutton, and R. Nerem (2008c), Rotating solar coronal holes and periodic modulation of the upper atmosphere, *Geophys. Res. Lett.*, *35*(10), doi: 10.1029/2008GL033875.

Lepping, R., et al. (1995), The Wind magnetic field investigation, *Space Science Rev.*, *71*(1), 207–229, doi: 10.1007/BF00751330.

Liu, J., L. Liu, B. Zhao, and W. Wan (2012), Influence of interplanetary solar wind sector polarity on the ionosphere, *J. Geophys. Res.*, *117*(A8), doi: 10.1029/2012JA017859.

Llewellyn, E., et al. (2004), The OSIRIS instrument on the Odin spacecraft, *Canadian Journal of Physics*, *82*(6), 411–422, doi: 10.1139/p10-093.

Lu, G., S. W. H. Cowley, S. E. Milan, D. G. Sibeck, R. A. Greenwald, and T. Moretto (2002), Solar wind effects on ionospheric convection: A review, *Journal of Atmospheric and Solar-Terrestrial Physics*, *64*, 145–157, doi: 10.1016/S1364-6826(01)00080-3.

Marsh, N., and H. Svensmark (2000), Cosmic rays, clouds, and climate, *Space Science Rev.*, *94*(1-2), 215–230, doi: 10.1023/A:1026723423896.

Mason, G., M. Desai, U. Mall, A. Korth, R. Bucik, T. Von Rosenvinge, and K. Simunac (2009), In situ observations of CIRs on STEREO, Wind, and ACE during 2007–2008, *Solar Physics*, *256*(1), 393–408, doi: 10.1007/s11207-009-9367-0.

McComas, D., S. Bame, P. Barker, W. Feldman, J. Phillips, P. Riley, and J. Griffee (1998), Solar wind electron proton alpha monitor (SWEPAM) for the advanced composition explorer, *Space Science Rev.*, *86*, 563–612, doi: 10.1007/978-94-011-4762-0_20.

Mendillo, M., and K. Schatten (1983), Influence of solar sector boundaries on ionospheric variability, *J. Geophys. Res.*, *88*(A11), 9145–9153, doi: 10.1029/JA088iA11p09145.

Mlynczak, M., et al. (2008), Solar-terrestrial coupling evidenced by periodic behavior in geomagnetic indexes and the infrared energy budget of the thermosphere, *Geophys. Res. Lett.*, *35*(5), doi: 10.1029/2007GL032620.

Mlynczak, M., L. Hunt, J. Kozyra, and J. Russell (2010), Short-term periodic features observed in the infrared cooling of the thermosphere and in solar and geomagnetic indexes from 2002 to 2009, *Proc. Roy. Soc. A*, *466*(2123), 3409–3419, doi: 10.1098/rspa.2010.0077.

Mukai, T., S. Machida, Y. Saito, M. Hirahara, T. Terasawa, N. Kaya, T. Obara, M. Ejiri, and A. Nishida (1994), The low energy particle (LEP) experiment onboard the Geotail satellite, *J. Geomag. Geoelectr.*, *46*, 669–692.

Neugebauer, M., and C. Snyder (1966), Mariner 2 observations of the solar wind 1. Average properties, *J. Geophys. Res.*, *71*(19), 4469–4484, doi: 10.1029/JZ071i019p04469.

Newell, P. T., K. Liou, and G. R. Wilson (2009), Polar cap particle precipitation and aurora: Review and commentary, *Journal of Atmospheric and Solar-Terrestrial Physics*, *71*, 199–215, doi: 10.1016/j.jastp.2008.11.004.

Nicolet, M., and A. Aikin (1960), The formation of the D region of the ionosphere, *J. Geophys. Res.*, *65*(5), 1469–1483, doi: 10.1029/JZ065i005p01469.

Ogilvie, K., et al. (1995), SWE, a comprehensive plasma instrument for the Wind spacecraft, *Space Science Rev.*, *71*(1), 55–77, doi: 10.1007/BF00751326.

Otto, A. (2005), The magnetosphere, *Lect. Notes Phys.*, *656*, 133–192, doi: 10.1007/978-3-540-31534-6_5.

Paularena, K. I., and J. H. King (1999), Nasa's IMP 8 spacecraft, in *Interball in the ISTP Program*, *NATO Science Series*, vol. 537, edited by D. G. Sibeck and K. Kudela, pp. 145–154, Springer Netherlands, doi: 10.1007/978-94-011-4487-2_11.

Pilipp, W. G., H. Miggenrieder, M. D. Montgomery, K.-H. Mühlhäuser, H. Rosenbauer, and R. Schwenn (1987), Characteristics of electron velocity distribution functions in the solar wind derived from the Helios plasma experiment, *J. Geophys. Res.*, *92*(A2), 1075–1092, doi: 10.1029/JA092iA02p01075.

Prikryl, P., V. Rušin, and M. Rybansk (2009), The influence of solar wind on extratropical cyclones – Part 1: Wilcox effect revisited, *Ann. Geophys.*, *27*(1), 1–30, doi: 10.5194/angeo-27-1-2009.

Pulupa, M. (2013), Space physics illustrations, `http://sprg.ssl.berkeley.edu/~pulupa/illustrations/`, accessed: 07/02/2013.

Randall, C. E., et al. (2005), Stratospheric effects of energetic particle precipitation in 2003-2004, *Geophys. Res. Lett.*, *32*, L05,802, doi: 10.1029/2004GL022003.

Roble, R. (1976), Solar EUV flux variation during a solar cycle as derived from ionospheric modeling considerations, *J. Geophys. Res.*, *81*(1), 265–269, doi: 10.1029/JA081i001p00265.

Rodriguez, J., H. Carlson Jr., and R. Heelis (2012), Auroral forms that extend equatorward from the persistent midday aurora during geomagnetically quiet periods, *Journal of Atmospheric and Solar-Terrestrial Physics*, *86*(0), 6–24, doi:10.1016/j.jastp.2012.06.001.

Ruohoniemi, J., and R. Greenwald (1996), Statistical patterns of high-latitude convection obtained from Goose Bay HF radar observations, *J. Geophys. Res.*, *101*(A10), 21,743–21,763, doi: 10.1029/96JA01584.

Russell, C., and R. Elphic (1978), Initial ISEE magnetometer results: Magnetopause observations, *Space Science Reviews*, *22*(6), 681–715, doi: 10.1007/BF00212619.

Sibeck, D., R. Lopez, and E. Roelof (1991), Solar wind control of the magnetopause shape, location, and motion, *J. Geophys. Res.*, *96*(A4), 5489–5495, doi: 10.1029/90JA02464.

Sloan, T., and A. Wolfendale (2008), Testing the proposed causal link between cosmic rays and cloud cover, *Environmental Research Letters*, *3*(2), 024,001, doi:doi:10.1088/1748-9326/3/2/024001.

Smith, C., J. L'Heureux, N. Ness, M. Acuña, L. Burlaga, and J. Scheifele (1998), The ACE magnetic fields experiment, *Space Science Rev.*, *86*, 613–632, doi: 10.1007/978-94-011-4762-0_21.

Smith, E. J. (2001), The heliospheric current sheet, *J. Geophys. Res.*, *106*(A8), 15,819–15,831, doi: 10.1029/2000JA000120.

Solanki, S. K., B. Inhester, and M. Schüssler (2006), The solar magnetic field, *Rep. Prog. Phys.*, *69*, 563–668, doi: 10.1088/0034-4885/69/3/R02.

Solomon, S., P. Crutzen, and R. Roble (1982a), Photochemical coupling between the thermosphere and the lower atmosphere 1. Odd nitrogen from 50 to 120 km, *J. Geophys. Res.*, *87*(C9), 7206–7220, doi: 10.1029/JC087iC09p07206.

Solomon, S., G. Reid, R. Roble, and P. Crutzen (1982b), Photochemical coupling between the thermosphere and the lower atmosphere 2. D-region ion chemistry and the winter anomaly, *J. Geophys. Res.*, *87*(C9), 7221–7227, doi: 10.1029/JC087iC09p07221.

Sonett, C. (1982), Sunspot time series: Spectrum from square law modulation of the Hale cycle, *Geophys. Res. Lett.*, *9*(12), 1313–1316, doi: 10.1029/GL009i012p01313.

Stone, E. C., A. M. Frandsen, R. A. Mewaldt, E. R. Christian, D. Margolies, J. F. Ormes, and F. Snow (1998), The Advanced Composition Explorer, *Space Science Rev.*, *86*, 1–22, doi: 10.1007/978-94-011-4762-0_1.

Tinsley, B. (2000), Influence of solar wind on the global electric circuit, and inferred effects on cloud microphysics, temperature, and dynamics in the troposphere, *Space Science Rev.*, pp. 1–28, doi: 10.1023/A:1026775408875.

Wilcox, J., and N. Ness (1967), Solar source of the interplanetary sector structure, *Solar Physics*, *1*(3-4), 437–445, doi: 10.1007/BF00151368.

Wilcox, J., P. Scherrer, L. Svalgaard, W. Roberts, R. Olson, and R. Jenne (1974), Influence of solar magnetic sector structure on terrestrial atmospheric vorticity, *J. Atmos. Sci.*, *31*, 581–588, doi: 10.1175/1520-0469(1974)031<0581:IOSMSS>2.0.CO;2.

Wolf, R. (1975), Ionosphere-magnetosphere coupling, *Space Science Rev.*, *17*(2), 537–562, doi: 10.1007/BF00718584.